.

Search for New Massive Long-Lived Neutral Particles decaying to Photons in pp Collisions at $\sqrt{S} = 8$ TeV

A DISSERTATION
SUBMITTED TO THE FACULTY OF THE GRADUATE SCHOOL
OF THE UNIVERSITY OF MINNESOTA
BY

Tambe Ebai Norbert

IN PARTIAL FULFILLMENT OF THE REQUIREMENTS
FOR THE DEGREE OF
Doctor of Philosophy

Prof. Yuichi Kubota

September, 2014

Acknowledgements

There are many people that have earned my gratitude for their contribution to my time in graduate school.

Dedication

To those who held me up over the years

Abstract

Dark matter particles, if they exists in nature, are believed to be neutral, stable, weakly interacting with ordinary matter and maybe massive. The hunt for dark matter particles is on! There are theoretical models which predict the existence of dark matter particles that can be produced in a proton-proton collider like the Large Hadron Collider, with sufficient center of mass energy. Gauge Mediating Supersymmetric Model is an example of such models. It describes the production and decay into isolated energetic photons, new, massive, neutral, weakly interacting particles known as supersymmetric particles. The lightest supersymmetric particle, the Neutralino ($\tilde{\chi}_1^0$), is a prime example and its decay into a photon is accompanied by a light weakly interacting and stable particle, the gravitino ($\tilde{G}$). The properties of the gravitino makes it a very good candidate for dark matter particles. The resulting photon from such a decay, is understood to be delayed in its arrival time at the detector due to inherent dynamics understood to be well described by supersymmetry and not the current theory, the standard model. The signature of a delayed photon is not specific to only supersymmetric models but could be the result of probably some new model not relating to the standard model. Using the Compact Muon Solenoid detector at the LHC, we have performed a search for delayed photons produced from proton-proton collisions at the center of mass energy, $\sqrt{S} = 8$ TeV. We did not find any excess of events over standard model background. Consequently, we compute an upper limit on the possible existence of a lightest neutralino with mass and proper lifetime; $m_{\tilde{\chi}_1^0} \geq \chi\chi \; GeV/c^2$ and $\tau_{\tilde{\chi}_1^0} \geq \chi\chi$ ns respectively, as described in the gauge mediated supersymmetric models. We also show that using only the timing information of the electromagnetic calorimeter as an observable, the CMS detector is sensitive to neutralinos with life time up to 30 ns which no previous experiment had shown. We provide hints on possible improvements which might help discover delayed photons in future search analysis.

Contents

List of Tables

List of Figures

Chapter 1

Introduction

Matter as observed around us makes up only 4.5% of our total universe or multiverse as some currently believe. This matter is best described with unmatched precision by simple symmetries known as gauge symmetries. The mathematics of gauge symmetry currently used in our understanding of the visible or baryonic universe is best implemented in the Standard Model (SM). The SM cannot describe non-visible or non-baryonic matter which make up the larger percentage of matter content in our universe. Observational experiments in Cosmology and Astrophysics tend to reinforce speculation that this non-visible or *Dark Matter* (DM) could consist of particles which have long lifetime collectively called *Long-Lived* (LL) particles. In general, LL particles can be charged (electromagnetically charged i.e interact with light (photons) or color charged) or neutral (cannot interact with light in the context of the SM).

Of particular interest to the scientific community are neutral LL particles, since DM is understood to not have a direct interaction with light and could very weakly interact with visible matter. Recent results seems to be indicating that dark matter particles, if they exists, could be very light i.e having very small mass around eV to keV mass range. These are known as Warm Dark Matter (WDM). DM particles could also be heavy with mass around GeV to TeV mass range called Cold Dark Matter (CDM). A peculiar property is that they are stable.

In this thesis we have performed a model-independent search for Neutral Massive Long Lived Particles (NMLLP) decaying to photons. NMLLP can be produced in proton-proton (pp) collisions by the Large Hadron Collider (LHC) with a center of mass energy $\sqrt{S} = 8$ TeV. The phenomenon of interest are delayed photons produced in the decay of a metastable next-to-lightest supersymmetric particle (NLSP). The NLSP is this case is the NMLLP. A classic example of a NLSP is the neutralino ($\tilde{\chi}_1^0$). It decays into a photon and the lightest supersymmetric particle (LSP) called the gravitino ($\tilde{G}$). Assuming the conservation of a symmetry known as R-parity, the neutralinos are pair produced in a cascade decay of higher massive supersymmetric particles produced from pp collision. While the gravitino being the LSP is stable and together with it being neutral and weakly interacting makes it a good candidate particle for DM. The resulting energetic and delayed photon, isolated in this case, is detected using the electromagnetic calorimeter. High transverse momentum (p_T) spray of hadronic particles called jets and missing transverse energy due to the weakly interacting nature of the gravitino as it leaves the detector undetected, accompany this decay. The photon arrival time at the electromagnetic calorimeter is delayed due to the long lifetime of the neutralino. An event containing the decay of a neutralino, produced in the LHC pp collider with be recorded using the Compact Muon Solenoid (CMS) detector. The CMS detector is located at one of the beam crossing or collision points (also known as Interacting Point (IP)) at Point 5 in Cessy, France. Relying on the excellent timing and energy resolution of Electromagnetic Calorimeter (ECAL) sub detector, of the CMS detector, we can distinguish between high energy photons from NMLLP decay and photons produced in interactions excellently and precisely described by the Standard Model (SM). Finding a LL particle would address a lot of important questions in modern physics such as the following: Why is there so much matter and not anti-matter around us? Is there an explanation for the particle content and mass hierarchy as currently observed in the SM? What is the origin and existence of Dark Matter (DM)? Do all fundamental forces behave as a single force at some higher energy scale? Answers to these questions will provide a clear path for physics beyond the standard model.

This thesis is divided into the following chapters:

- Chapter 1 presents the introduction and general outline of this thesis.

- In Chapter 2, we begin with the motivation behind a search for neutral long lived particles predicted to exist is some BSM. The physics of long-lived particle is also described. This chapter also presents compelling hints from theory, experiment as well as cosmological observation which point to the possible existence of NMLLPs. An example BSM model used as guiding model to this analysis is also described leading to our event selection based of its predicted phenomenology. Previous analysis and their results are also shown.

- In Chapter 3, describes the experimental setup particularly the LHC collider and CMS detectors and also a detail description of the sub-detectors of the CMS which have been used in our search analysis.

- In Chapter 4, we provide a detail outline of Time measurement and Calibration of ECAL in order to reliably use timing as tool to search for long-lived particles which decay into photons and electrons depositing their energy unto the crystals of the ECAL.

- Chapter 5, The reconstruction of objects referred to as photons, jets and missing transverse energy $E_\mathrm{T}^\mathrm{miss}$ according the CMS standards is described here. The ECAL timing as useful for particle identification is presented.

- Chapter 6 hashes out our search strategy for neutral massive long-live particles.

- Chapter 7 provides an interpretation of the results obtained by our analysis in the context of Gauge Mediated Supersymmetry Breaking(GMSB).

- Chapter 8 outlines the possibility of future analysis strategy as we prepare to begin running LHC fully at $\sqrt{S} = 13$ TeV in 2015.

- In chapter 9, we conclude by giving a summary, presenting our results and possible improvement in this of the analyses.

Chapter 2

Models and Phenomenology of Long-Lived Particles

2.1 The Standard Model of Particle Physics

The Standard Model (SM) provides a thorough and experimentally valid description of the fundamental constituents of all the matter and it interactions (except gravity) in our universe. Predictions by this model of elementary particle physics agrees with almost all of the available experimental data with unmatched precision. However, there are some theoretical and experimental difficulties with this model such as the existence of Dark Matter (DM) and neutrino masses which point to an extension of the SM to a much general model to which the SM is embedded within. An example of such a parent model could be based on the idea of supersymmetery.

This section briefly describes the SM as pertaining to the understanding of this thesis as well as its limitations.

2.1.1 Main Components

The mathematics used to formulate the SM is known as relativistic quantum field theory. Particles are represented as quantum fields and their dynamics and interaction is based on a Lagrangian formalism using a Lagrangian density $\mathcal{L}$. Its main building blocks are the following:

- All of Matter around us can be described by fermion fields.

- These matter fields interact with each other mediated by vector bosons of a particular symmetry.

- These matter fields are massless and cannot mix with each other until they interact with another field called the Higgs field and in the process obtain their mass and mixing. This process is known as Higgs mechanism.

Fermions

Fundamental particles are characterized in terms of 3 quantities: Mass, Charge and Spin, where spin is a non-spatial or internal quantum number unlike mass and charge. The spin of a particle can be integer or half-integer.

Fermions are particles with half-integer spin ($\frac{1}{2}\hbar$). They obey a kind of statistics referred to as the *Fermi-Dirac* statistics meaning no two identical fermions can occupy the same state. Fermions can be massive as well as massless. The can be charged or be neutral. Fermions have anti-particles which have the same mass and spin but a different charge.

In the SM, the dynamics of fermions and their possible interactions is described by the Dirac equation given as:

$$Diraceuationhere! \tag{2.1}$$

Nevertheless, there are two types of fermions: Leptons and Quarks.

Leptons can participate in electromagnetic and weak interactions and not strong interactions whereas quarks can perform all three interactions. In the SM, leptons have integer charge values and come in three families or flavours of pairs arranged in a certain mass hierarchy with the third generation being the most massive. The third generation flavour leptons can decay into the lower generation leptons through weak interactions. Each charged lepton of a particular flavour has its neutral pair partner known as its neutrino. For example, the pair partner of an electron is the electron neutrino. In the SM, neutrinos are considered massless however, numerous experiments have confirm neutrinos have a very tiny mass and can oscillate from one flavour into another under sufficiently large distances.

Quarks also come in pairs of three flavours with the most massive third generation flavour capable of decaying to its lower generation flavours through electro-weak interactions. Each pair flavour or generation of quarks consists of an "up-type" and a "down-type" quark. Quarks have have an electric charge as well as a color charge since they can participate in strong interactions. Up-type quarks like (up(c), charm(c), top(t)) have charge of $+\frac{2}{3}$ and Down-type quarks such as (down(d), strange(s), bottom(b)) have charge of $-\frac{1}{3}$. Charges are expressed in units of elementary charge e. Quarks make up the contents of a less fundamental particles like the proton using in hadron collisions and their distribution inside a proton is modelled according to Parton Distribution Functions (PDF). A full content of fermions in the SM and their properties can be seen in table **TABLE OF FERMIONS IN SM**.

$$TABLE AND FIGURE OF FERMIONS IN SM \tag{2.2}$$

In electro-weak interactions, fermions can be distinguished as being "Left" or "Right" handed. Infact, the SM, does not provide any understanding of why only 3 generations of elementary particles have been discovered. However, from the SM, it is clear that one generation of leptons –the electron and the electron neutrino (e ,ν) and one generation of quarks –the up-quark and the down quark (u, d) is enough to describe all the visible matter we see around us.

Interactions

The interaction of matter fields or fermions is mediated by force-mediating particles called bosons–meaning they have an integer spin ($n\hbar$, where n is an integer). The SM describes three different forces and their carriers. For the electromagnetic force described under the mathematical frame work of Quantum Electrodynamics (QED), the force carrier is a massless boson called the photon, γ. For the two nuclear forces: The weak force which was later in the 1960s developed in a combined electroweak framework by Sidney Glashow, Abdus Salam and Steven Weinberg[], the force-mediator are the massive vector bosons $W^{\pm}$, Z^o discovered at CERN in 1983 []. The strong force described under the frame work of Quantum Chromodynamics (QCD) is not unified with the other two forces and is mediated by massless gluon, g. The table below show

some the property of the force mediating particles in SM.

$$"PLEASE INSERT TABLE/DIAGRAM FOR GAUGE BOSONS HERE!" \qquad (2.3)$$

The current frame work of the SM was formulated with inputs from theory and results from several experiments so it in not uncommon to introduce mathematical concepts and constructs to describe the SM in an elegant manner. It is with this spirit that we will continue the rest of this section.

Fermion interaction is based on the sole concept of symmetry i.e the invariance of a Lagrangian density, $\mathcal{L}$, under a particular set of transformations. In the SM, these set of transformations are called local transformation or gauge transformations(symmetry groups) because the depend on space-time coordinates and can be expressed as:

$$SU(3)_C \times SU(2)_L \times U(1)_Y \qquad (2.4)$$

The symmetry groups describe the following parts of the SM interactions:

- $SU(3)_C$ defines the strong nuclear interaction where quarks with color charge C are coupled to massless eight(octet) gluons in the frame work of QCD. The surprising phenomenon here is that unlike electromagnetic interactions (QED) where massless photons cannot interact with each other, these massless guons can interact with each since they carry color charge. There are three color charges.

- $SU(2)_L \times U(1)_Y$ defines the electroweak interaction. The four corresponding gauge(because they are from these gauge groups) massless bosons $W_\mu^{1,2,3}, B_\mu$ mix with each other to give the physical electroweak bosons $W^\pm$ charged and neutral Z^0 and γ. The $W^\pm$ and Z^0 becomes massive after the Higgs mechanism. These bosons couple using the "charge" of the weak interaction called weak isospin T and the hypercharge Y to all fermions or matter. With $W^\pm$ couple only to left-handed fermions and right-handed anti fermions only leading to what is known as parity violations. Using the third component of the weak isospin T_3 and the hyper charge Y, the resulting electromagnetic charge of all fermions can be defined using

the relation:

$$Q = T_3 + \frac{Y}{2} \tag{2.5}$$

In the SM, all left handed fermions have $T^3 = \pm\frac{1}{2}$ and are thus represented as multiplets of the SM, in this case isospin doublets whereas, right-handed fermions have have $T^3 = 0$ and are thus isospin singlets in the SM. The table below summarises these electroweak fermion multiplets and their quantum numbers.

$$TABLE\,OF\,SM\,multiplets\,and\,their\,Quantum\,Numbers. \tag{2.6}$$

The $SU(2)_L \times U(1)_Y$ theory carry two coupling constants g and g' which parametrizes the strength of these interactions and they are connected to the electric charge of each fermions in the following relation:

$$e = gsin\theta_w = g'cos\theta_w \tag{2.7}$$

The parameter θ_w is known as the *Weinberg angle* which is not derived from the SM but measured from experiment to be equal to $sin^2\theta_w \approx 0.231$. The physically observed gauge bosons are a rotation of the weak eigenstates involving the Weinberg angle given as:

$$The\,Physical\,Gauge\,Bosons\,in\,terms\,of\,weak\,eigenstates. \tag{2.8}$$

This angle participates in an important phenomenon in SM known as quark mixing. Unfortunately in the current simplest state of SM, there are no lepton mixing(due to a global symmetry called lepton number conservation) even though the recent discovery of neutrino masses existence [] hints at the possibility of such a mixing in the lepton flavour sector. Nevertheless, in the quark sector, it is possible for the $W^\pm$ to change the flavour of a given quark, for example and up-type quark u can transition to a down-type quark d. This type of transitions are referred to as Flavour Changing Charge Currents (FCCC). However, it is not possible for Z^0 to change the flavour of a quark but also lead to small violation of parity. There is active research to discover large Flavour Changing Neutral Currents (FCNC) from certain weak interactions since most of these are suppressed. The quark mixing is entirely described using a 3 by 3 component matrix known as the

Cabibbo-Kobayashi-Maskawa (CKM) matrix given in equation below:

$$TheCKMmatrix \tag{2.9}$$

The entire components of this matrix is measured from experiment and not derived from the SM.
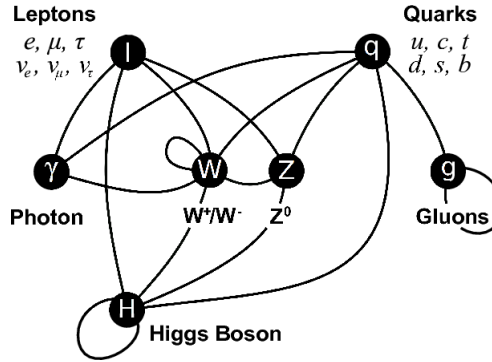
Figure 2.1: Fermions interaction through bosons as described in the SM.

Quantum Chromodynamics and Parton Distribution Functions

The strong nuclear interactions described by QCD is based on the $SU(3)_C$ gauge group. Only quarks and gluons are involved in this interaction. Each quark can exists in three different strong "charge" called *color* (dubbed are red, green and blue) thus forming a color triplet. Anti-quarks also carry opposite color charges. The color strength is the same for all three colors. Gluons unlike photons carry a combination of color and anti-color charge which lead to the self interaction of gluons. Gluons are not affected by Higgs mechanism thus remain massless after breaking of $SU(2)_Y$. Leptons carry no color and as such are color singlets thus cannot participate in strong interactions.

The value of the strong coupling α_S which determines the strength of the strong interaction depends on the momentum transfer Q^2 as do the coupling constants of the $SU(2) \times U(1)_Y$ groups. For large Q^2, α_S approaches zero in a process in QCD referred to as *asymptotic freedom* and the quarks are nearly free while for small values of Q^2, α_S grows large and the quarks are tightly bound. This process is also referred to as *confinement*. Quarks are always confined to hadronic bound states called baryons or

mesons consisting of three quarks or a quark and anti-quark respectively.

The proton is the most stable baryon. It is made up of two up quarks and one down quark such that its electric charge is 1. These are called valence quarks. It turns out that from experiments, valence quarks are not the only quarks present in a proton. Infact it is best to describe the proton as made up of *partons*. Partons are quarks and gluons. Inside a proton, it is possible for a gluon to radiate or split up into a quark anti-quark pair. These kind of quarks are referred to as sea quarks. All partons in a proton carry the total momentum of the proton, however during proton-proton collision in a hadron accelerator, the partons are the actual colliding particles and not the protons so it is imperative to know the momentum fraction x of an individual parton inside a proton. The momentum fraction of a parton is expressed as a *Parton Distribution Functions* (PDFs). PDFs gives the probability of finding a parton with momentum fraction x. PDFs are measured from electron-proton accelerator experiments such as HERA in Germany. The PDF is expressed as a function of the fraction of the parton momentum to the total proton momentum and the momentum transfer Q^2 from the electron interacting with the parton, $f(x, Q^2)$. Figure below shows an example of the PDFs for a few quarks and gluons and strange quarks with momentum fractions x_q and x_g respectively with a momentum transfer of Q^2.

$$DIAGRAM OF EXAMPLE PDFs \tag{2.10}$$

It is imperative to know the PDFs very well when performing a search for physics beyond the SM as calculating scattering *cross sections* which is an experimentally observable quantity describing the probability of a particular process happening highly depends on PDFs. In addition to this, due to the PDFs, the center of mass for proton-proton collision which in actual experiment is parton-parton collision is much reduced from $\sqrt{S} = 14$ TeV as advertised in the LHC to $\sqrt{\hat{s}} \approx 2$ TeV and this depends on the particular partons involved in the parton-parton interaction.

Without the Higgs mechanism, all the particles described so far will be massless. But experiments observe massive particles, So how do we get these particles to have mass in the SM? This questions remains and important one in particle physics. However in the case of the SM, we obtain mass by "manually" breaking the gauge symmetries in the

SM through the addition of mass terms into the SM Lagrangian. Thus the introduction of mass terms through the Higgs mechanism breaks the local gauge invariance in the theory which describes all the above interactions.

Higgs Mechanism

Earlier attempts prior to the 1960s for constructing a gauge theory of weak interactions had failed because the gauge bosons always end up massless. Which indicated that the strength of the weak interaction can be infinite just like the electromagnetic interactions. However, theories were in complete contrast with results from experiments as weak interactions were understood to be limited to very small distances of about the scale of the nucleus. Thus these massless gauge bosons had to become massive.

In the Higgs-Brout-Englert [] mechanism, consist of introducing an extra weak isospin complex scaler doublet:

$$INSERTHIGGSDOUBLETHERE \tag{2.11}$$

which is invariant under the gauge symmetry group $SU(2)_L \times U(1)_Y$ and has its dynamics described by the Lagrangian density:

$$HIGGSDOUBLETLAGRANGIAN \tag{2.12}$$

where $\boldsymbol{\Phi}$ is the Higgs doublet with spin-0 complex components. The parameter $\mu^2 < 0$ and the real parameter $\lambda > 0$ of the scalar Higgs potential(figure 2.2).
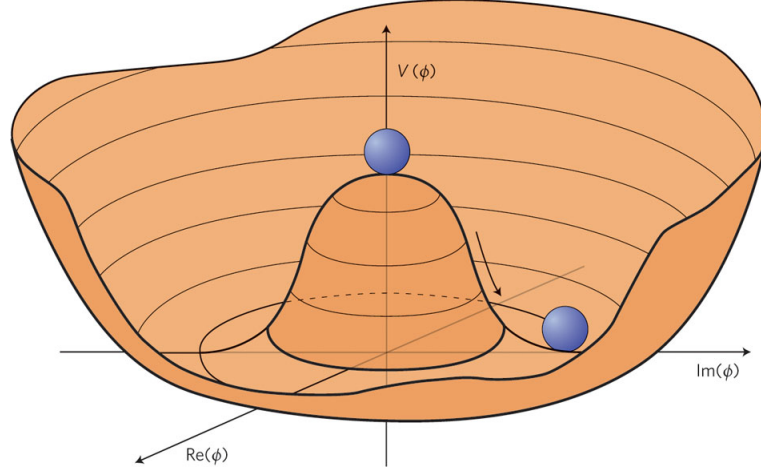
Figure 2.2: Higgs boson "Mexican hat" potential which leads to spontaneous symmetry breaking.

is chosen such that the potential $V \to \infty$ as $\mathbf{\Phi} \to 0$. It is easily seen from the previous equation that the minimum of the potential is not longer at $\mathbf{\Phi} = 0$ but lies at :

$$|\phi_0| = \sqrt{\frac{-\mu^2}{\lambda}} = \nu \tag{2.13}$$

With this choice of parameters settings, the potential V is itself $SU(2)_L$ symmetric but any other choice of ground state breaks $SU(2)_L$ symmetry. This is referred to as the *Higgs-Brout-Englert mechanism* or *Higgs mechanism* for simplicity. This choice of parameters of the potential V can be seen in figure below.

$$puthiggspotentialpictureinhere! \tag{2.14}$$

One can then choose $\phi_1 = \phi_2 = \phi_3 = 0$ and then parametrise the higgs doublet as small perturbations around the minimum as follows:

$$equationofhiggspertubations \tag{2.15}$$

with $h(x), \eta_i(x)$ being 4 real scaler fields. Using the gauge freedom of $SU(2)_L \times U(1)_Y$ once can choose the *unitarity gauge* where the kinetic terms for the fields $\eta_i(x)$ vanish and their with the requirement of local gauge invariance, $\eta_i(x)$ couple to the massless gauge bosons to be to become massive and the resulting Higgs doublet is expressed as:

$$Higgs\,doublet\,with\,imaginary\,parts\,removed \tag{2.16}$$

With the imaginary parts removed and the field $h(x)$ is identified as the physical real scalar Higgs field or Higgs boson. The ground state chosen so that the photon remains massless while the other gauge bosons including the real scalar Higgs field are massive with their masses given as:

$$Eqns\,of\,Gauge\,boson\,masses\,and\,Higgs\,mass \tag{2.17}$$

The Z^0 mass m_Z can also be expressed in terms of the $W^\pm$ mass m_W and the Weinberg angle as:

$$Z\,mass\,to\,W\,mass\,equation \tag{2.18}$$

Thus one can easily observe that all the effects of the W and Z bosons can be described in terms of the parameters e, θ_w and ν which can be expressed in term of Fermi constant all of which were experimentally known. Thus it is fine to say that the Higgs mechanism could predict the masses of W and Z gauge bosons which were experimentally found and measured in 1983 at LEP[].This discovery was one of the greatest triumphs of the SM. With the value of $\nu \approx 246$ GeV, we can then express the mass of the fermions in terms of the Yukawa coupling as (from the Yukawa sector of the Lagrangian) :

$$m_f = \lambda_f \frac{\nu}{\sqrt{2}} \tag{2.19}$$

according to the *Yukawa terms* $\mathcal{L}_{\mathcal{Y}}$ which is symmetric under $SU(2)_L \times U(1)_Y$ given by

$$YUKAWA\,equation \tag{2.20}$$

with λ_f dimensionless Yukawa couplings which are free parameters of the model.
The search for the Higgs boson was the main purpose for the construction of the LHC at CERN and an June 04, 2012, a Higgs-like candidate particle was found whose result can be seen in figure below:

$$insert figure of Higgs boson discovery here! \tag{2.21}$$

It is important to understand that there is no fundamental reason why there should be only one Higgs field to which all fermions couple to. As we will see in other supersymmetry that there could be more than one Higgs field.

2.1.2 Decay Rate and Life Time

Of all fundamental "point-like" particles in the SM, only the electron e, and electron neutrino ν, as leptons and the up u, and down d, as quarks are "understood" to be stable. The rest of the SM particles can transform from one particle generation to another either through disintegration or oscillation. This stability is measured with respect to the age of the universe which is understood to be about 13.7 billion years old. Thus a composite particle such as the proton made up of two u and one d valence quarks although seemingly very stable can disintegrate with some theories beyond the SM predicting to remain stable in a time period of about 10^{33} years. The disintegration of a particle also referred to as decay is usually through an interaction of some sort. This interaction is between the particle and its daughter particles and can be electromagnetic, weak, strong, any pair or maybe all three types of interactions. In particle Physics, the stability of a particle is related to the conservation of a quantum number or conserved quantity such as energy, spin, angular momentum and charge. Other factors may also play an important role in determining the stability of a particle such as phase space (enough room to decay into), violation of some property such as strangeness or the mediating particle usually a boson being very massive compared to the momentum of the parent particle. The decay rate, Γ, a quantity which can be calculated obtained from prediction made in some theory can also be measured experimentally. Its measurement provide access to the underlying type of interaction or mediating particles involved in the decay and thus can be used as a direct tool to search for other interactions beyond the current known ones. A single particle can decay into more than one type of particles. As long as the conditions for decay are met, a decay into any potential particle whose mass if less than the mass of the parent particle is possible. The decay into a particular set of particle(s) is known as a decay channel. Different decay channels can

be quantified with respect to the overall total decay rate of the parent particle. This quantification is expressed as a *branching ratio (BR)*. Thus the BR gives quantitative estimate of the possibility of a parent particle decaying to specific daughter particles or through that channel.

The inverse of a decay rate is the *life time*, denoted as τ.

$$\tau = \frac{\hbar}{\Gamma} \tag{2.22}$$

A convenient way to express life time is in distance. This distance called cτ, where c is the speed of light in vacuum and τ is the life time is called the *decay length*. cτ is the decay length as measured in the frame with respect to the center of mass of a moving particle. However, laboratory measurements are not done in the center of mass of the moving particle as this would be near impossible to do. So since the particle is moving with some speed with respect to a stationary laboratory, we have to take into consideration this difference in motion of frames(the moving particle frame and the stationary Laboratory frame) in understanding our measurement in the laboratory of the decay length of the moving particle and how this is translated into the true decay length of the particle. The effect we need to consider is known in special relativity as *time dilation* and the decay length is a measure of the distance between the position where the particle was produced to where it decayed. Our laboratory measurement is expressed as:

$$L = \beta\gamma c\tau \tag{2.23}$$

where $\beta = \frac{v}{c}$ with v being the speed of the moving particle and $\gamma = \frac{1}{\sqrt{1-\frac{v^2}{c^2}}}$ is the ratio accounting for time dilation effect and from this one can translate back into the true decay length of a particle c*tau*. The decay length can also be expressed in terms of the momentum p of the particle where $p = \beta\gamma m$ and thus $L = \frac{p}{m}c\tau$. We see that the decay length of a particle is proportional to the momentum and inversely proportional to the mass of the particle.

The decay rate depends on quite a number of particle properties as we've mentioned earlier. As a result, the decay length for electromagnetic, can be very different to that of weak and strong interactions. The decay length of of strong interactions having the shortest decay length due to the strong nature of the interaction leading high decay

rates. This is followed by the weak and then electromagnetic interactions. There are some exceptions to this due to other factors playing a key role than interactions alone as we mentioned. The table and graph below show the mass and decay length of SM particles and their interaction.

$$TABLESHOWINGSM particle decay rates and interactions involed as well as mass Vs decay length.$$
(2.24)

In particle physics experiments it is very challenging to measure the life time or decay length or a particle by measuring the time it travels from where it was produced to where it decayed. Rather, the number of events present initially and that observed after a time period t is used to measure the lifetime of a particle. The decay rate (or life time) of a particle is related to the number of particles observed though the equation:

$$N(t) = N_0 \exp\left(\frac{-t}{\tau}\right) = N_0 \exp\left(\frac{-\Gamma t}{\hbar}\right)$$
(2.25)

where $N(t)$ is the number of particles observed at an arbitrary time t and N_0 is the number of particles observed at an initial time where it is assumed no particle has decayed yet usually at $t = 0$. A distribution of the observed number of particles(usually a Poisson distribution) can be plotted with time measured. The resulting distribution if fitted with a Poisson distribution faction and the parameter of the Poisson distribution function extracted to give us the decay rate or life time of a particle.

Particles with large decay length or long life time are commonly referred to as *Long-Live* (LL) particles. Many models beyond the SM predict the existence of such particle. They are also understood to be prime candidates for particles making up DM. Before we dive into such models, it is necessary to understand in detail the decay of particles and factors which determine a particle's decay length as well as the kind of LL particles considered detectable in a multi-particle physics detector such as those at the Large Hadron Collider (LHC) CERN pursued in this thesis.

Particles described by the SM come in different types of long-lived. First, we have the stable elementary (as we currently believe) such as the electron and neutrinos. Second, we have the meta-stable elementary such as the muon and finally the (very)

long-lived composite particles such as the neutrons and protons. By referring to the different classes of particles according to their life time, we can asked the question, what properties of a particle makes it stable, meta-stable or long-lived?

There are three possible answers to this question:

- A particle could be the lightest state carrying a conserved quantum number and as such remain entirely stable e.g the electron and proton.

- The decay of a particle to another lighter particle could only be made possible through some suppressed or effective coupling and as a result ends up being meta-stable e.g the muon

- If the mass of a particle is relatively close in quantity to the particle it is decaying into such that their difference in mass is quite small, the decay will be eventually suppressed. This goes by the name lack of phase space for decay e.g decay of neutron $(n \to p + e^- + \bar{\nu}_e)$. In this scenario the difference in mass between the neutron (n) and the proton (p) is ≈ 1.293 MeV and as a result determines the type of associated particle produced in this decay as observed.

In this thesis, we will only be interested in Meta-Stable (MS) particles, and in particular focus on Massive Neutral Meta-Stable particles which we refer to as Neutral Massive Long-Lived Particles (NMLLP). A rather more descriptive name would be Neutral Massive Meta-Stable Particles(NMMP) since these particles are not LL in the real sense but might decay into other elementary particles which are observable at detectors and how long-lived you refer to them depends on the possible lifetime of this particle your detector is sensitive to. As their lifetime might range from a few nanoseconds $(10^{-9}$s$)$ to the age of the universe (13.7 billion years) likewise from a few μm to billions of km. Thus, our interpretation of LL particles will be those whose decay length range from a few μm to few meters or detectable size of the LHC detectors and in particular electromagnetic sector of LHC detectors.

We have restricted ourselves to electromagnetic (local U(1) gauge symmetry) neutral particles as their charge counterparts can be studied using conventional magnetic spectrometer and ionization methods as shown in this studies for Heavy Stable Charge Particles (HSCP).

2.1.3 Limitations Of the Standard Model

The SM (Glashow, 1961; Weinberg, 1967; Salam, 1968) currently describes almost entirely all of the observed phenomena and fundamental particles of nature with unmatched precision. However, as indicated from previous sections, there is more to be understood such as:

- **General Formalism:** There are way too many parameters in the SM which are not derived within the theory but rather measured experimentally such as the Weinberg angle and the CKM matrix elements. The SM does not account for the multiplet structure of fields as well as why there are only three observed generations of particles. Currently observed neutrino masses are not required in the SM as neutrinos are considered massless in the SM. Even the Electroweak symmetry breaking is not very well understood.

- **Astrophysical:** Why is there so much matter and not anti-matter? If the Big Bang is suppose to be the correct theory about the universe existence, then matter and anti-matter must be observed in equal composition, however, Baryon asymmetry ratio show that there is more matter than anti-matter, where is all the expected anti-matter? This could be explained as charge-parity violation in weak interactions of the SM but this is quite small(not strong enough) to explain for all the observed discrepancy. Baryonic Acoustic Oscillation results also known as CMB as well as WMAP results all indicate the presence of excess matter which does not interact with light and is collision less called Dark Matter (DM) as well as increase energy density responsible for the rapid accelerated expansion of the universe called Dark Energy (DE). All these observations cannot be explained within the SM.

- **Theory:** The SM is seen as some low energy theory of some much deeper underlying theory(SM as an effective theory) due to the fact that it cannot describe gravity. In Addition to this, the coupling constants in the SM all vary with energy and so the definite question if whether there is a much higher scale where all these couplings become a single coupling(Unification of forces). Supersymmetric extensions of the SM show unification of forces at Grand Unified Theories (GUT) energy scale of $\approx 10^{15}$ GeV.

- **Mass Hierarchy and Fine-tuning:** Why are particles masses in the standard model arranged in such a hierarchy? from neutrino masses of few eV to top mass of 173 GeV. In terms of energy scale, from the electroweak symmetry breaking scale of ≈ 100 GeV to Planck scale, $M_p = 10^{19}$ GeV, there are no other particles and especially scalers or any known interactions. The Higgs mass incredible precise contributions from higher order (loop) effects to its mass in order to maintained its experimentally observed value of ≈ 125 GeV. Understanding this precise contributions and cancellations to arrived at the expected value is referred to as the fine-tuning problem and extensions of the SM like supersymmetry provide a very natural answer as we will see later.

2.2   Beyond Standard Model Physics

The Higgs boson's mass as understood from theoretical calculations should receive contributions from higher order (loop interactions as is known) inorder to observe the experimentally measured mass of possibly 125 GeV or of order $O(100$ GeV). However, all these corrections are said to cancel out such that the experimentally observed mass is as it is measured. The question of where these additional loop corrections disappeared into cannot be understood within the context of the SM. However, theories beyond the SM such as supersymmetry provide a natural understanding of how these loop effects cancel out to arrive at the observed mass. To go a step further with this; the mass of a particle can be expressed as

$$m^2_{physical} = m^2_{Bare} + \delta m^2_1 \tag{2.26}$$

where $m^2_{Physical}$ is the true mass of the particle measured in the laboratory; in the case of the Higgs boson of order $O(100$ GeV) while m^2_{Bare} is the true mass of the particle which cannot be calculated or measured. δm^2_1 is the quantum one loop corrections to the true mass which can be calculated. Thus from the measured mass and the calculated one loop quantum effect mass, one can get the true mass of the particle. The quantum loop contributions can come from bosons as well as fermions. For the Higgs scenario, the Higgs can couple or interact with every particle through interactions like $\lambda_f H \bar{f} f$ for fermions and $\lambda_S |H|^2 S^2$ for scalar or bosons with λ_f and λ_S the coupling constants

and not necessarily equal. The quantum one loop corrections as calculated from the following diagrams:

$$1 Loop diagrams for Higgs Boson/Fermion interactions. \tag{2.27}$$

is given as:

$$\delta m_{1,f}^2 = \frac{1}{16\pi^2}|\lambda_f|^2\left(-2\Lambda^2 + 6m_f^2\ln\left(\frac{\Lambda}{m_f}\right) + ...\right) \tag{2.28}$$

$$\delta m_{1,S}^2 = \frac{1}{16\pi^2}|\lambda_S|^2\left(\Lambda^2 - 2m_S^2\ln\left(\frac{\Lambda}{m_S}\right) + ...\right) \tag{2.29}$$

where Λ is understood to be some cut-off scale where new kind of interaction at a much higher energy scale is needed to regulate the low energy behaviour of the SM. Λ could be the Planck scale(10^{19} GeV) where this new kind of interaction if gravity. The two things to observe from this calculations is that first, corrections to the higgs bare mass m_{Bare}^2 are not proportional to the Higgs mass as is the case with other SM particles like the electron[]. Second, these corrections are of the order of $\approx 10^{38}$ GeV^2 with the signs reverse for fermions or scalar corrections. Despite this expected corrections to the true Higgs mass, the measured or physical Higgs mass squared $m_{H,Physical}^2$ is of the order $\approx 10^4$ GeV^2. The only way there is an agreement between this correction and physical Higgs mass is if the true Higgs mass, $m_{H,Bare}^2$ is fine-tuned with a precision of about 1 in 10^{17}. This enormous fine-tuning is considered a fundamental problem with the Higgs mechanism of the SM and is referred to as not *natural*. Infact, since in the SM, there is only once scalar particle which is the Higgs boson, this fine-tuning cannot be understood. However, in other models beyond the SM such as suppersymmetry, the fermion one loop quantum correction which comes with an opposite sign to the scalar one loop quantum correction with $\lambda_f = \lambda_S$,there is a cancellation and this fine-tuning can be understood. Another interpretation of this issue is through the question of why there is so much difference in energy scale between the electroweak scale $O(100$ GeV$)$ and the Planck energy scale $O(10^{19}$ GeV$)$ where gravity effects to particle interaction becomes significant?. This is referred to as the *Hierarchy problem* stated above as one of the motivation to go beyond SM.

Another drawback with the SM is that of unification. It is believed that at a higher energy scale since SM seems to be describing the low energy behaviour of some parent theory, the electromagnetic, weak and strong interactions all become one interaction just as the electromagnetic and weak interaction unified into the electroweak interaction as the electroweak energy scale ≈ 100 GeV. i.e

$$SU(3)_C \times SU(2)_L \times U(1)_Y \subset \mathcal{G} \tag{2.30}$$

where $\mathcal{G}$ is some larger symmetry group. In SM, this does not happen at any higher energy scale. However, in suppersymmetry, there is a clear unification of individual coupling constants or electromagnetic, weak and strong interactions at the GUT energy scale of $\approx 10^{15}$ GeV. This effect can be seen in the following figures as taken from [].

$$Plot showing Unification of Coupling Constants. \tag{2.31}$$

2.2.1 Supersymmetry

In relativistic Quantum Field Theory (QFT), the idea of symmetry is used to provide a better understanding of a particle and its possible interaction with other particles. Symmetries can be classified into two broad categories: Space-Time or external symmetries known as Poincaré(rotational and translational) symmetries also known as groups and internal or gauge (which as we saw earlier; $SU(3)_C \times SU(2)_L \times U(1)_Y$ describing the quantum numbers– color, weak and hypercharge respectively) symmetries. In a quest to include gravitational interaction along with all the other forces of nature into a unique frame work called unification, it was thought that one could combine these two classes of symmetries into a bigger class of symmetry. However, Coleman and Mandula in their so-called "*no-go*" theorem in 1967 [7] showed that the direct product nature of super groups; a direct approach to extending symmetries to bigger symmetries, is not possible. Thus these two class of symmetries cannot be combined into a bigger parent symmetry. This produced a challenge of finding a scenario where $[M^{\mu\nu}, T^a] \neq 0$, considering that the generators of these groups; $P^\mu, M^{\mu\nu}$ and T^a corresponding to these symmetries have a direct product; Poincaré $\times$Gauge group, for which $[P^\mu, T^a] = [M^{\mu\nu}, T^a] = 0$. Because of this *no-go* theorem, such a parent symmetry group is not possible if one used

generators of Lorentz tensors. The only way out is to find a symmetry which is generated by spinoral(particle's spin) charges instead of tensorial (space-time) charges. Such a theorem was found in 1975 by Haag, Lapuszanski and Sohnius [**?**] called the *Haag-Lapuszanski-Sohnius* theorem with its corresponding algebra called the *Lie-superalgebra*. The generators of these *Lie-superalgebra*, Q^α, with $\alpha = 1, ..., N$. N is the number of generators for the supersymmetry. In this Thesis we will only be considering the case where $N = 1$ i.e only one supersymmetry generator. This is known as the minimal supersymmetry. If you are interested in learning more about extensions of this minimal version see this excellent text [**?**]. The generators Q^α can be expressed in terms of Weyl Spinors Q_a where $a = 1, 2$ and must satisfy anti-commutation relation with its conjugate. This is the major aspect of introducing supersymmetry. Thus for these generators to be supersymmetric, they must satisfy the following relations:

$$\left\{Q_a, \bar{Q}_b\right\} = 2\left(\gamma^\mu\right)_{ab} P^\mu, \quad [Q_a, P^\mu] = 0, \quad [Q_a, M^{\mu\nu}] = \frac{1}{2}\left(\Sigma^{\mu\nu}\right)_a^b Q_b \qquad (2.32)$$

where γ^μ is define such that $\{\gamma^\mu, \gamma^\nu\} = 2g^{\mu\nu}$ and $\Sigma^{\mu\nu} = \frac{i}{2}[\gamma^\mu, \gamma^\nu]$ and $\bar{Q}_a$ is the Hermitian conjugate to Q and is also a generator. From these relations, two very fundamental consequences arise:

- Particles in a given supermultiplet have the same mass but differ in their spin by half a unit.

- There is an equal number of fermionic and bosonic degree of freedom or states in every irreducible representation of supersymmetry.

From the above observation, we define supersymmetry as the symmetry which transforms particles from one spin into another. Hence these supersymmetry generators transform fermions into bosons or bosons into fermions with the same mass.

$$Q|\textbf{Fermion}\rangle = |\textbf{Boson}\rangle, \quad Q|\textbf{Boson}\rangle = |\textbf{Fermion}\rangle \qquad (2.33)$$

This reveals to us that, in supersymmetry, every particle has a partner with the same mass with supermultiplets chosen such that every SM particle with spin $0, \frac{1}{2}$, 1, 2 have a partner with spin $\frac{1}{2}, 0, \frac{1}{2}, \frac{3}{2}$ respectively in the same supermultiplets. In

supersymmetry, there are three kins of supermultiplets referred to as *Chiral*, *Vector* and *gravity* multiplets. In building a minimal supersymmetric extension of SM only the Chiral and Vector supermultiplets are used and thus we will concentrate only on these two. The following table shows the different supermultiplets as encountered in supersymmetry.

$$\text{TABLE of SUSY Multipletes and spin} \qquad (2.34)$$

So far we have mostly seen the algebraic approach to supersymmetry. However in order to build models(supersymmetric Lagrangians) and make predictions, we have to return to the idea of fields. This brings us to the idea of the so-called *superfields* first proposed and realized by my hero Abdus Salam and Strathdee [**?**]. Superfields are fields defined on a superspace which is an ordinary MinKowski-space, x^μ and four anticummuting Grassmann, numbers θ. For more on this see []. Thus a general superfield is an operator-valued function Φ on a superspace $\Phi\left(x^\mu, \theta, \bar\theta\right)$ Its components consist of from ordinary scalar fields (real or complex), Lorentz vector fields and Left-handed or Right-Handed Weyl(2 degrees of freedom) spinor fields. The Table below shows an example of the components which make up the superfield or supermultiplets. Each component represents a SM particle and its super partner with the same mass.

$$\text{TABLE OF A SUPERFIELD AND COMPONENTS} \qquad (2.35)$$

In constructing the MSSM, only the Chiral and Vector supermultiplets or superfields are used.

2.2.2 Minimal Supersymmetric Standard Model

The Minimal Supersymmetric Standard Model or MSSM is an extension of the SM to include its supersymmetric partner particles.

As a result the already 19 free parameters of the SM is increased with an additional 105 free parameters. These are a lot of parameters for any fundamental theory describing elementary particle interactions and thus undermines its predictive power. Thus, a

generic or parent theory must be preferred in which the number of free parameters for the theory to predict is much reduced. Through this way, it is much easier to study the theory phenomenologically. For example, the supersymmetric (SUSY) extension of the SM theory with gravity is called mSUGRA and has only 6 parameters while a SUSY extension of SM with purely gauge interaction is called Gauge Mediated Supersymmetry Breaking (GMSB) and has only 5 parameters. Other SUSY theories such as Anomalous Supersymmetry Breaking (ASB) have 6 parameters.

In this thesis, we will only talked about GMSB theories as these describe and predict the existence of LL particles. A full table of SM particles and their SUSY counterparts as understood through the MSSM can be seen in the table below.

$$\text{TABLE OF SM/SUSY PARTICLES IN MSSM.} \tag{2.36}$$

In SUSY, the particle dynamics and interaction Lagrangian is written in terms of supermultiplets are already seen in table above. However, the superpotential is what defines the phenomenology and hence mass spectrum of the model. In MSSM, the superpotential is given as thus[**?**]:

$$W_{\text{MSSM}} = \bar{u}\mathbf{y_u}\mathcal{Q}H_u - \bar{d}\mathbf{y_d}\mathcal{Q}H_d - \bar{e}\mathbf{y_e}\mathcal{L}H_d - \mu H_d H_u \tag{2.37}$$

Where the objects H_u, H_d, $\mathcal{Q}$, $\mathcal{L}$, $\bar{u}$, $\bar{d}$, $\bar{e}$ are chiral superfields corresponding to the chiral supermultiplets given in table above. The dimensionless couplings $\mathbf{y_u}$,$\mathbf{y_d}$,$\mathbf{y_e}$ are 3×3 matrices known as the Yukawa couplings. One thing to note here is that instead of a single Higgs double as in the case with the SM, two Higgs double are present; H_u and H_d to give mass to up-type and down-type quarks and leptons. The superpartners of these Higgs particles which are fermions and those of the gauge bosons called gauginos mix to produce new neutral and charged fermions called Neutralinos and Charginos respectively. An aspect which is not present in the SM.

In MSSM, a combination of baryon (B) and lepton number (L) symmetries is combined to give a more fundamental symmetry called *R-Parity*[**?**] or *Matter Parity*[**?**].

From a multiplicative combination of B and L numbers, we get R-parity expressed as:

$$R_P = (-1)^{3(B-L)+2S} \tag{2.38}$$

where S is the spin of the particle. This is a conserved quantum number which is from a discrete symmetry. This symmetry commutes with supersymmetry. Thus particles in a given supermultiplet do not have the same R parity. SM particles like quarks have an Even parity $R_P = 1$ while SUSY particles like squarks have Odd parity $R_P = -1$. This has a lot of important phenomenological consequences such as the following:

- In the decay of SUSY particles, the lightest SUSY particle (LSP) have odd parity $R_P = -1$ and thus it must be absolutely stable. In addition to its absolute stability, if it is neutral an interacts only and very weakly with ordinary matter, then it is a good candidate for non-baryonic dark matter as required by cosmology.[?]

- Every SUSY particle produced which is not the LSP, will eventually decay into the LSP or an odd number of LSPs.

- SUSY particles can only be produced in pairs in a collider experiment.

Thus in generic SUSY models with minimal particle content, where the superpontential include terms which violate Lepton (L) and baryon (B) numbers; R-parity conservation can be imposed giving rise to R-parity Conserving (RPC) models with the LSP stable while R-parity can be violated resulting to R-parity Violating (RPV) models where the LSP is unstable and decays to SM particles.
In this Thesis, we consider only RPC models since our motivation is to search for neutral stable particles motivated by them being candidates particles which make up dark matter (DM).

If SUSY is to become a theory which describes nature, then the observation of components within the same supermultiplets having the same mass, i.e $m_B = m_F$ must be unrealistic as untill presently no experiment has found a selectron(SUSY partner of electron) with a mass of $0.512\,\mathrm{MeV}$ for example. Therefore, SUSY must be spontaneously broken. Spontaneous Supersymmetry Breaking (SSB) means that the vauum expectation value of a scalar field(in SUSY an auxiliary field) must be non-zero. The

manner in which this breaking occurs determines the phenomenology of any model. As one would imagine, there are many different ways of breaking SUSY(through gravity, gauge etc) resulting to many different SUSY models. However, in this thesis, will concentrate only on those for which guage interactions is responsible for SUSY breaking. Such SUSY models are generally referred to as Gauge Mediated SUSY breaking models (GMBS) ranging from Pure to General Gauge Mediation (GGM) as one would easily find in the literature. We will also focus on models with Soft Breaking as we would like favour SUSY models with phenomenology within the reach of the LHC. Soft breaking would mean the SUSY breaking terms in the SUSY protential consists of only masses and terms whose couplings have positive mass dimension. This ensures the existence of sparticles with masses around a few TeV where they can possibly be produced at current particle colliders.

2.2.3   Soft Supersymmetry Breaking

The idea of being soft is such that the spontaneous breaking must be caused by couplings with positive mass dimension and not dimensionless coupling. Also this allows for the observed hierarchy between the electroweak energy scale 100 GeV and the Planck energy scale 10^{19} GeV. The Lagrangian for soft SUSY breaking terms can be written as thus:

$$\mathcal{L}_{\text{Soft}}^{\text{MSSM}} = -\frac{1}{2} \left(M_3 \tilde{g}\tilde{g} + M_2 \tilde{W}\tilde{W} + M_1 \tilde{B}\tilde{B} \right) + c.c \tag{2.39}$$

$$- m_{H_u}^2 H_u^* H_u - m_{H_d}^2 H_d^* H_d - (b H_u H_d + c.c.) \tag{2.40}$$

$$- m_Q^2 \tilde{Q}^+ \tilde{Q} - m_L^2 \tilde{L}^+ \tilde{L} - m_{\tilde{u}}^2 \tilde{u}^+ \tilde{u} - m_{\tilde{d}}^2 \tilde{\bar{d}}^+ \tilde{d} - m_{\tilde{e}}^2 \tilde{\bar{e}}^+ \tilde{e} \tag{2.41}$$

$$- \left(a_u \tilde{\bar{u}}\tilde{Q}H_u - a_d \tilde{\bar{d}}\tilde{Q}H_d - a_e \tilde{\bar{e}}\tilde{L}H_d + c.c \right) \tag{2.42}$$

where M_1, M_2 and M_3 are the superpartners of the gauge bosons of the SM symmetry group. They are referred to as the Bino, Wino and gluinos(8 gluinos because there are 8 gluons in the SM). I have intentionally omitted scalar mass terms in this Lagrangian and rather included SUSY breaking contribution to the Higgs potential.

This results in the following mass spectrum for particles in the MSSM as seen in the figure below:
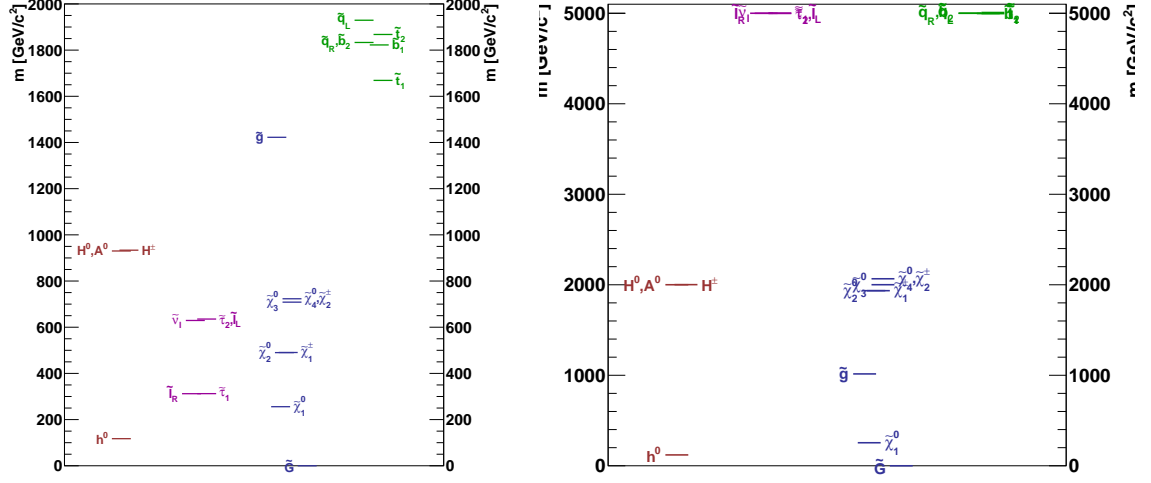
Figure 2.3: SUSY Mass spectra in the mGMSB SPS8 model (left) and GGM Model (right) with mass of gluino ($M_{\tilde{g}} = 1.0$ TeV)

In summary, SUSY predicts in addition to SM particles, new particles whose spin (S) differ from their SM counterparts by half-integer.Bosons (fermions) in the SM have superpartners which are fermions (bosons) respectively. The superpartners of SM fermions are scalars comprising of sfermions ($\tilde{l}$), sneutrinos ($\tilde{\nu}$) and squarks ($\tilde{q}$) while gluinos $\tilde{g}$ being fermions are the superpartners of the massless gauge bosons of strong interaction, gluons. The scalar Higgs (2 needed for obvious reasons) boson and the vector gauge bosons of electro-weak interaction have fermionic superpartners called higgsinos, winos and binos. These can mix to form a pair of mass eigenstates called charginos ($\tilde{\chi}_j^\pm, j = 1, 2$) and a quartet mass eigenstates neutralinos ($\tilde{\chi}_i^0, i = 1, ..., 4$).

2.2.4 Gauge Mediated Supersymmetry Breaking and Phenomenology

General Model

Constructing a SUSY model requires the following items:

1. A gauge group describing the nature of particle interaction.

2. Specifying a superpotential.

3. Providing the method for SUSY breaking.

In the case of our Minimal Supersymmetric Standard Model (MSSM), we have already provided these as seen in equations,2.4, 2.38 and 2.40-2.43. These provide the particle content and interactions we need. However, we must account for the interactions needed in the mediation of SUSY breaking down to the energy scale of the MSSM or soft terms to be observed at the LHC.

SUSY breaking is realised through the existence of a *Hidden Sector*(Hidden because it couples only indirectly and very weakly to our "observable sector" of SM particles and their superpartners) whose dynamics manages to break SUSY. The nature of this breaking is not relevant for phenomenology but rather the "mediators" which communicate the effects of this breaking to the super partners of the SM particles. Thus, these mediators or agents must couple to this "Hidden Sector" as well as the "observable sector". In gauge mediating SUSY breaking (GMSB), these agents have the usual SM gauge interactions and are called *Messenger fields*. These Messenger files through loops(instead of normal tree level interction) couple with the SM superpartners. As a result MSSM particle(gauginos and sfermions) get SUSY breaking masses at the loop level referred to as soft terms. The mass of this Messenger fields M_{mess} defines the energy scale of SUSY breaking. If $M_{mess} \ll M_{Pl}$ then induced SUSY breaking occurs at a must lower energy scale instead at the Planck energy scale where gravitational interactions become very significant and the effects of the breaking is first felt by these Messenger fields and later communicated to the observable sector through SM gauge interactions. In terms of energy scales, the picture is such that SSB happens at an energy scale $\mathbf{F}$ which defines the mass of a gravity mediating suparpartner particle, the gravitino as

$$m_{3/2} = \frac{\mathbf{F}}{\sqrt{3}M_{Pl}} \tag{2.43}$$

where $M_{Pl} = 1.3 \times 10^{19}$ GeV , then the energy scale $\mathbf{F}_S$, which is the *induced SUSY breaking* scale in the hidden sector. This along with the mass of the messenger particles M_{mess}, defines the masses of the gauginos and sfermions of the MSSB or visible sector. If $\mathbf{F}_S < \mathbf{F}$ then the interaction between the hidden sector and the fundamental SUSY breaking is weak interaction other wise $\mathbf{F}_S \approx \mathbf{F}$ and the interaction is strong. The consequences of this is that one would no longer expect the mass of the gravitino $m_{3/2}$ to be given as in equation (2.45) but rather suppressed by $\frac{M_{mess}}{M_{Pl}}$ in GMSB models.

In the mass spectrum of these models, the gravitino mass can be varied to a very small value only bounded by cosmological results, thus making it the lightest SUSY particle (LSP). Spanning the gravitino mass is expressed as a parameter c_{grav} which directly determines the lifetime of the SUSY next to lightest sparticle decaying to the gravitino. We will see more of this ahead.

In General GMSB, a simple model of the messenger sector can be chosen to consists of chiral supermultiplets of leptons and quark with the same quantum numbers $SU(3)_C \times SU(2)_L \times U(1)_Y$ as the SM gauge groups with representations given as:

$$\tilde{\ell} \sim (1, 2, 1) \quad \tilde{\ell}' \sim (1, 2^\star, -1) \tag{2.44}$$

$$\tilde{q} \sim (3, 1, -\frac{2}{3}) \quad \tilde{q}' \sim (3^\star, 1, \frac{2}{3}) \tag{2.45}$$

They couple to each other via a superpotential of a gauge singlet chiral supermultiplet S with an F-term as in the O'RAIFEARTAIGH model[?]. This messenger superpotential can be given as:

$$W_{\text{mess}} = \lambda_\ell S \tilde{q} \tilde{q}' + \lambda_q S \tilde{\ell} \tilde{\ell}' \tag{2.46}$$

We can thus obtain SUSY breaking by allowing vacuum expectation values VEV for both S and its auxiliary components F-term as $\langle S \rangle$ and $\langle \mathbf{F}_S \rangle$ where the $\mathbf{F}_S$ does not have to coincided with $\mathbf{F}$ as mentioned earlier and can be parametrised as:

$$\mathbf{F} = C_{grav} \cdot \mathbf{F}_S \tag{2.47}$$

This equation indicates that the non-zero VEV for the F-term is the main cause of fundamental SUSY breaking and this breaking is transferred to the messenger particles through radiative interactions as C_{grav} is a dimensionless parameter. Diagonalising the leptons and fermions masses with their scaler superpartners leads to mass terms for messenger particles as:

$$m^2_{\tilde{\ell}\tilde{\ell}'} = |\lambda_\ell \langle S \rangle|^2, \qquad m^2_{\tilde{\ell}_{\text{scalars}}} = |\lambda_\ell \langle S \rangle|^2 \pm |\lambda_\ell \langle F_S \rangle| \tag{2.48}$$

$$m^2_{\tilde{q}\tilde{q}'} = |\lambda_q \langle S \rangle|^2, \qquad m^2_{\tilde{q}_{\text{scalars}}} = |\lambda_q \langle S \rangle|^2 \pm |\lambda_q \langle F_S \rangle| \tag{2.49}$$

From these messenger particle mass terms, we can defined a general scale for which these definations are can be trusted as:

$$\mathrm{M_{mess}} = (\lambda_q, \lambda_\ell) \langle \mathsf{S} \rangle \tag{2.50}$$

In pure gauge mediated SUSY breaking models (PGGM) it is required that $\lambda_q \neq \lambda_\ell$ [?] whereas in general gauge mediated (GGM) and minimal gauge mediated SUSY breaking (GMBS)[?] models, $\lambda_q \simeq \lambda_\ell \simeq \lambda$ and $\mathrm{M_{mess}} = \lambda \langle \mathsf{S} \rangle$

In the MSSM sector, the gauginos and scalars obtained their mass through 1-loop and 2-loop level corrections respectively. A simple diagrams for these corrections can be seen in figure .

In the minimal GBSM scenario, an additional parameter $\mathrm{N_5}$ specitying the number of messenger vector-like supermultiplets transforming under $SU(5)$ so as to allow for unification of gauge couplings at the GUT energy scale($M_{GUT} \approx 10^{16}$ GeV. $\mathrm{N_5}$ may not be too large so as to avoid gauge couplings diverging before GUT scale and as such the masses of MSSM gauge and scalars particles can be writen as:

$$\mathbf{M}_a = \frac{\alpha_a}{4\pi} \mathrm{N_5} \Lambda \tag{2.51}$$

$$\phi_i^2 = 2\Lambda^2 \mathrm{N_5} \sum_{a=1}^{3} C_a(i) \left(\frac{\alpha_a}{4\pi}\right)^2 \tag{2.52}$$

where $C_a(i)$ are some constants of $\mathsf{O}(1)$, α_a are coupling constants and

$$\Lambda = \frac{\mathrm{F}_S}{\lambda \langle \mathsf{S} \rangle} = \frac{\mathrm{F}_S}{\mathrm{M_{mess}}} \tag{2.53}$$

Ofcourse for PGGM models we will have two seperate λs defined as:

$$\Lambda_G = \frac{\mathrm{F}_S}{\lambda_q \langle \mathsf{S} \rangle} \tag{2.54}$$

$$\Lambda_S = \frac{\mathrm{F}_S}{\lambda_\ell \langle \mathsf{S} \rangle} \tag{2.55}$$

For complete description of PGGM and its parameters see [?]. $\mathbf{\Lambda}$ is called *the effective SUSY breaking scale* which defines the mass spectrum of MSSM gauginos and scalars. In

GGM models [10, 11, 12], the mass of the gauginos $\mathbf{M}_a, a = 1, 2, 3$ defines the parameter space for these models. From equation we redefine the fundamental SUSY breaking scale F in terms of the effective SUSY breaking scale $\mathbf{\Lambda}$ as:

$$\mathbf{F} = C_{grav} \cdot \mathbf{\Lambda} \cdot \mathbf{M}_{\text{mess}} \tag{2.56}$$

and hence from equation gravitino mass is re-written as:

$$m_{\tilde{G}} = C_{grav} \cdot \frac{\Lambda \mathbf{M}_{\text{mess}}}{\sqrt{3} \mathbf{M}_{pl}} \tag{2.57}$$

We observe from above equation that in GMSB models the gravitino can become very light compared to gravity mediating models. It should not be surprising when the gravitino is identified as least stable SUSY particle (LSP) in GMSB models and is seen as a candidate for DM. C_{grav} as mentioned earlier determines the decay rate and hence the lifetime of a SUSY particle decaying to the gravitino. For instantaneous decay $C_{grave} \approx 1$ whereas for non-instantaneous decays C_{grav} can be varied accordingly to achieve of-the- order-of a particle detector size lifetimes.

GMSB Phenomenology

GMSB models attract a lot of interests because of the existence of first, light gravitinos–unlike gravity mediating SUSY models which require the gravitino mass to be of the other of $\simeq 100$ GeV and as such does not play any role in collider phenomenology, GMSB models allow for gravitino masses as low as a few eV. Second, unique gravitino-scalar-chiral fermion and gravitino-gaugino-gauge boson interactions. Figure shows feynman diagrams for these interaction.
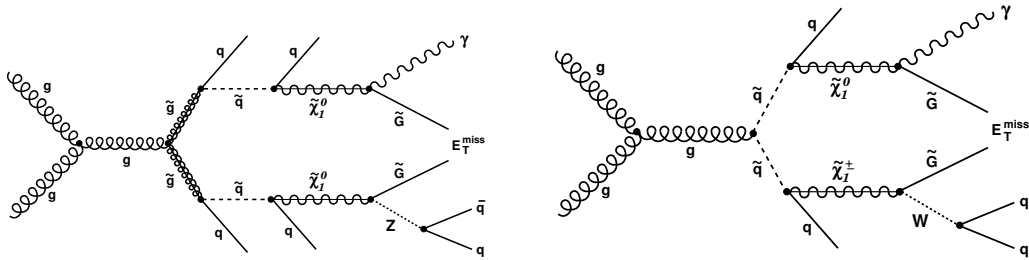
Figure 2.4: Feynman diagrams of of Gravitino interactions with superpartner pairs (ψ, ϕ) (a) and (λ, A)(b).

The presence of light gravitinos allows for the decay of any next-to-lightest MSSM particle to a gravitino as $\tilde{p} \to p\tilde{G}$ with the decay rate depending on the mass of the gravitino $m_{\tilde{G}}$ as long as R-parity is conserved. Thus every MSSM particle decay will eventually include a gravitino in its final states. This decay rate can be parametrised by C_{grav}. It is easy to see that $C_{grav} \geq 1$. Thus we define the parameter space for GMSB models as follows:

- For minimal GMSB (mGMSB): the parameter space is

$$\{\Lambda, \quad M_{\text{mess}}, \quad N_5, \quad \tan\beta, \quad sgn(\mu), \quad C_{grav}\} \qquad (2.58)$$

- For General Gauge Mediation SUSY breaking (GGM): The parameter space to scan is [8, 9]

$$\{\mathbf{M_3}(\text{gluino mass}), \quad \mathbf{M_2}(\text{Wino mass}), \quad \mathbf{M_1}(\text{Bino mass}), \quad \tan\beta, \quad sgn(\mu), \quad c\tau_{NLSP}\}$$
$$(2.59)$$

  The advantage with GGM models is that colored sparticles are not required to be be heavier than their electroweak sparticles allowing for greater discovery potential at hadron collider[13]

- For Pure General Gauge Mediation SUSY breaking (PGGM): The parameter space to scan is:

$$\{\Lambda_G, \quad \Lambda_S, \quad M_{\text{mess}}\} \qquad (2.60)$$

In these models, the Next-To-Lightest SUSY particle (NLSP) decays to the lightest SUSY particle (LSP), the gravitino and its SM partner. if $\tilde{p}$ is the NLSP, then it will decay is as follows:

$$\tilde{p} \to p + \tilde{G} \qquad (2.61)$$

In mGMSB models $\tilde{p}$ is the lightest neutralino(neutralinos come in four types and they are a mixture of Bino $(\tilde{B}^\circ)$,Wino $(\tilde{W}^\circ)$, higgsino $(\tilde{H}_u^\circ, \tilde{H}_d^\circ)$ depending on the choice of parameters M_1, M_2, M_3, or Λ, $\tan\beta$, and $sgn(\mu)$. and particle p is the photon (γ),

SM(or new) Z boson) (Z)(or Z') and the higgs (h). In this thesis, we will only focus on the parameter space for which the the particle $p = \gamma$ and $C_{grav} > 1$. This ensures that with the lifetime of our NLSP being finite, its decay happens *within the detector volume* and the resulting photon is delayed or non-prompt on detector time scales.

The decay rate for an NLSP to its SM partner and a gravitino goes like(details can be found in[6, **?**]):

$$\Gamma(N\tilde{L}SP \to \gamma\tilde{G}) \approx \frac{m_{N\tilde{L}SP}^5}{\mathbf{F}^4} \tag{2.62}$$

This approximation is almost the same for the non-minimal GMSB models except that we add other parameters showing explicit dependence of how the neutralino life time can be made as long as expected in collider detectors. It is important to observe here that, the decay rate is large for smaller values of fundamental SUSY breaking scale or equivalently smaller gravitino mass provided the neutralino mass is kept fixed. Thus if m_{NLSP} is of the O(100 GeV) or more and $\mathbf{F} \ll 1000$ TeV, meaning $m_{\tilde{G}} \leq 1$ KeV, then the above decay rate is of the order than can be observed at hadron collider detectors.

2.3 Long-Lived Particles in GMSB Models

We have in previous discussions mentioned in passing some reasons why the study of LL particles is very important for uncovering new physics beyond the SM. In addition to mass, charge and spin being experimental handles for the search of new physics, a particle's life time or decay length is indispensable as importable parameters related to the underlying interaction type of the decay can be extracted from the decay rate and hence provide direct window towards new physics interactions beyond the SM.

2.3.1 Production of supersymmetric particles at Hadron Colliders

Production of a supersymmetric (SUSY) particle at a hadron collider is a probabilistic process. This process can be quantitatively expressed as the production cross-section. The production cross-section is basically the sum of all the different probabilities of a given process happening. This probability depends on the distribution of type of incoming particles inside the colliding protons with enough proton energy fraction to create a supersymmetric particle. Since the mass of the supersymmetric particle being

create depends on the available center of mass energy of the colliding partons. In a hadron collider like the LHC, gluons are the one of these partons with the highest probability of proton energy fraction distribution. Sea quarks such as up and down quarks which make up the proton as well as valence quark which can exist inside the proton provide their energy fraction is large enough can also collide to create SUSY particles. The figure (2.3.1) show the parton distribution function against its energy fraction on the horizontal axis within a proton. The probability of creating a SUSY particle depends on the momentum transfer Q of these partons.

Figure 2.5: Parton distribution function (PDF) for partons against energy fraction on the horizontal axis for a particular momentum transfer Q value.

In order to be able to make comparisons between theoretical expectations and experimental observation or measurements, we have to be able to quantify these cross-sections of a given process happening at a particle collider. We do this by summing the probabilities of all the given ways by which a process can occur. The given ways by which a process can occur are represented by diagrams known as feynman diagrams. The fynman diagrams for the production of SUSY particles at LHC is given in (2.3.1).
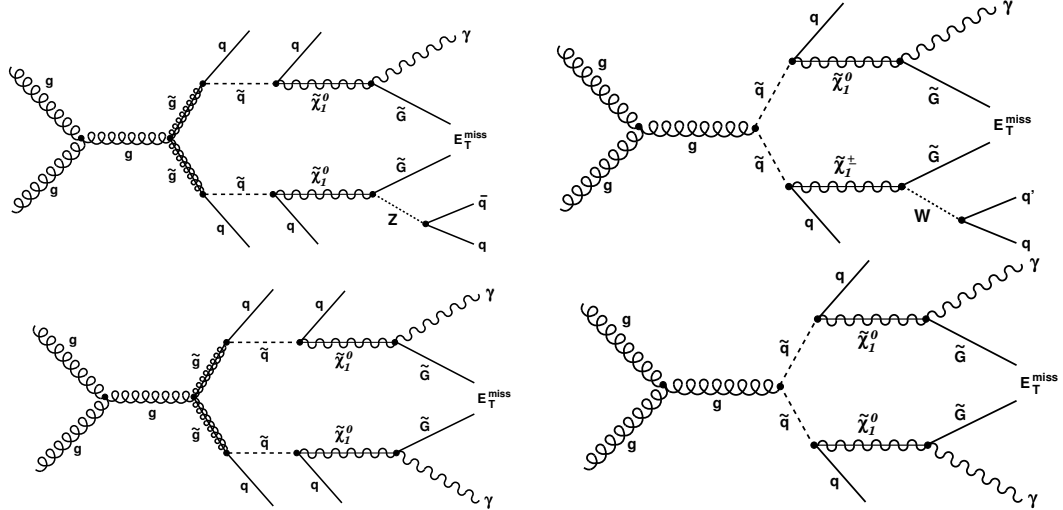
Figure 2.6: Feynman diagrams of single(top) and di(bottom) photon production from cascade decays of gluino and squark at LHC.

The list presented is not exhaustive at all but rather simplicity in computation. The sum or complete computations results in a single number known as the cross-section of the process occurring at the LHC for some amount of center of mass energy. This number called the cross-section is very small that it is express in term of a unit called a *barns* (b). (1 $b = 10^{-28} \ m^2$). Because this number is quite small it is usually further express with suffix in front of the unit barn such as *nano* (n) or *pico* (p) or *femto* (f). For example, the typical cross-section of producing a SUSY particle at the LHC is of the order of 1 $pb = 10^{-12} \times 10^{-28} \ m^2$ or at times 1 $fb = 10^{-15} \times 10^{-28} \ cm^2$ for some extremely rare SUSY processes. While a typical production of a standard model process such as the production of the Z or W bosons is of the order of a few $nb = 10^{-9} \times 10^{-28} \ m^2$. Thus, finding a SUSY particle in an environment such as the LHC is liken to *finding a needle in a haystack*, since most SUSY production cross-section are very small compared to an overwhelming high cross-section processes from the standard model.

2.3.2   Decay of supersymmetric particles in CMS detector

NLSP Decay Length

The SUSY particle produced will also decay instantaneously or stay a bit longer-before disintegrating. Usually this disintegration process occurs in a series of subsequent decays in a cascade manner until the final particle is stable and cannot decay. This decay is once again a probabilistic process which can also be expressed and quantified in a single real number. The probability depends on quite a number of factors like the availability of smaller particles for it to decay into and some others. Usually there must be a conservation of a fundamental quantum number or symmetry like the energy conservation for such a decay or decay chain to be possible. There are always many options for a given particle to decay into and each of these options is quantified by a number known as the *Branching fraction or Ratio*. Summing all the branching ratio for all the different decay processes gives the total *Decay Width*. This total decay width, calculated in theory from the different probabilities of the given particle to decay into other particles is a expressed as a single real number in units of GeV or MeV (GeV = giga electron volt). This number can be compared with measurements from experiments observing this different decays. In the case of the SUSY particles like the NLSP, the decay width depends on the nature of the interaction which in this case is different from

the interactions currently understood within the SM.

The probability for a NLSP particle produced with an energy E having mass m to travel a distance x before decaying to a photon and gravitino in the laboratory frame is given as:

$$\mathcal{P}(\mathsf{x}) = 1 - \exp\left(-\frac{x}{\mathrm{L}}\right) \tag{2.63}$$

where

$$\mathrm{L} = c\tau_{NLSP} \cdot (\beta\gamma)_{NLSP} \, [mm] \tag{2.64}$$

and

$$(\beta\gamma) = \frac{|p|}{m} = \sqrt{\left(\frac{E}{m}\right)^2 - 1} \tag{2.65}$$

with its proper decay length as given by as(we have used equation 2.23 and 2.64 to go from decay rate to lifetime):

$$c\tau_{NLSP} \approx \left(\frac{m_{NLSP}}{\mathrm{GeV}}\right)^{-5} \left(\frac{\sqrt{\mathbf{F}}}{\mathrm{TeV}}\right)^4 \tag{2.66}$$

Its is important to observe here that, varying $\mathbf{F}$ changes the lifetime of the NLSP from being prompt to long-lived. This variation can be easily archived in GMSB models where the parameter C_{grav} is used so that the above proper decay length equation becomes:

$$c\tau_{NLSP} \approx C_{grav}^2 \left(\frac{m_{NLSP}}{\mathrm{GeV}}\right)^{-5} \left(\frac{\sqrt{\mathbf{F}_S}}{\mathrm{TeV}}\right)^4 \tag{2.67}$$

With C_{grav}, one could one could change the decay length of the NLSP such that its decay occurs within the volume of the detector such that the resulting photon is delayed. This gives a unique signature for discovering SUSY in hadron colliders as photons produced from SM interactions are prompt. In a simple GMSB model such as the SPS8, where the neutralino is the NLSP and gravitino is LSP, figure (**??**) show the kinematic properties and neutralino proper decay length distribution for the neutralino and its decayed photon in different parameter choices. The HepMC class in CMS Software (CMSSW) is used to measure and and exponential distribution as the one in (2.63) is fitted on the decay length distribution to extract its proper decay length as

produced in the MC generation.
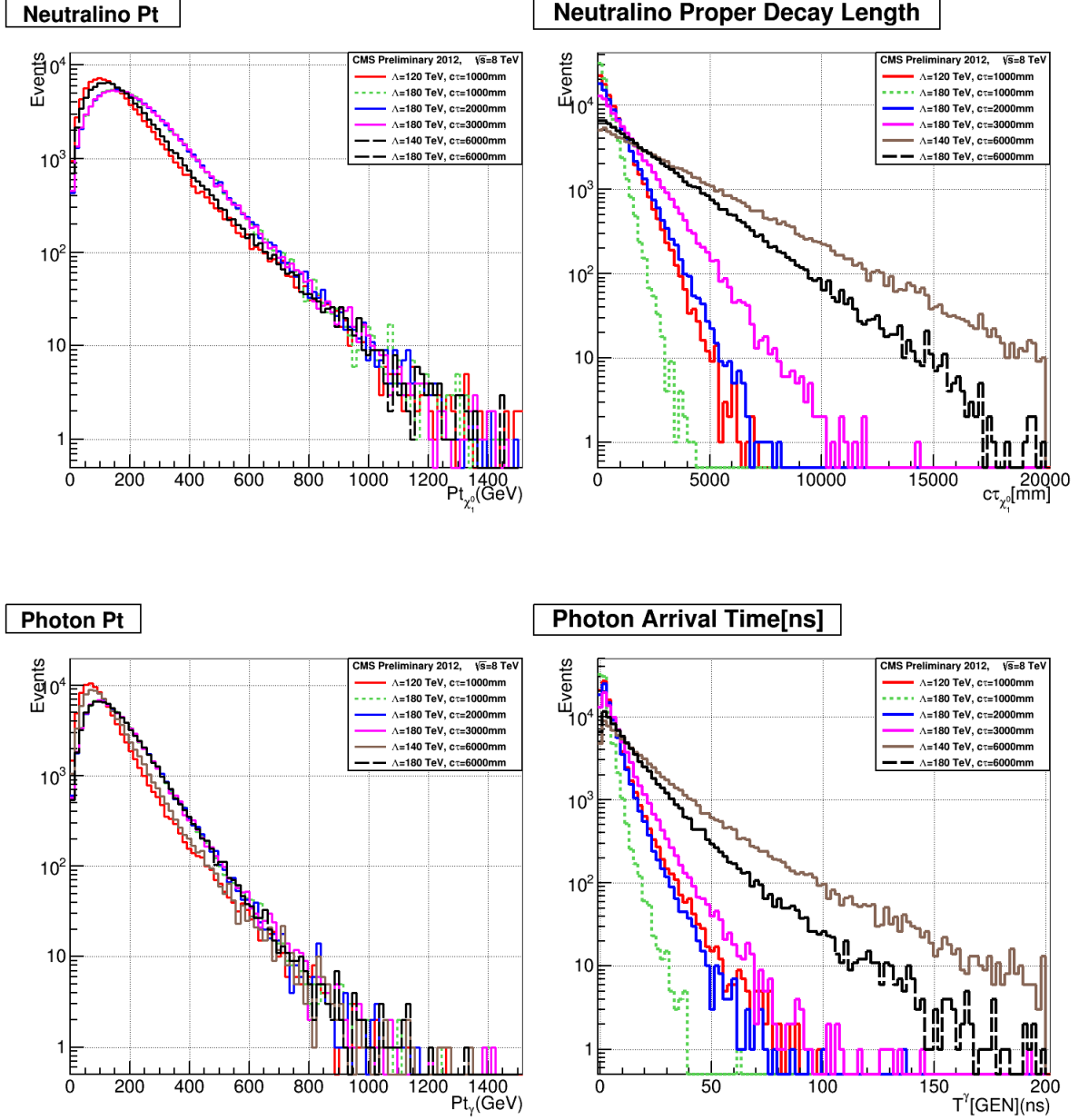
Figure 2.7: Neutralino transverse momentum distribution(top left) and proper decay length(top right) with its decayed photon transverse momentum distribution(Bottom right) and time of arrival at ECAL(Bottom right) for GMSB SPS8 model.

2.3.3 Why is the search for neutral long-lived particles important

Finding answers to fundamental questions such as the following: What is the origin of neutrino masses, Why are there only 3 types of leptons and quarks? Where do all the parameters in SM come from? Other big questions include: What is Dark Matter (DM)? is DM made of particles? Can one detect these particles? Why is there so much asymmetry between matter and anti-matter in our universe? Is there some energy scale or early epoch in the evolution of the universe where all the fundamental forces behaved as a unique kind of force. Do baryons such as the proton exist forever? What is the lifetime of the proton? What is Dark Energy (DE)? Is the Universe expanding indefinitely? Are there other Universes? provide added impetus to search for particles BSM. We believe that the discovery of a long-live particle which are not known to exist within the current SM will provide unique access to understanding physics BSM and making measurements which can provide answers to most of the above questions.
Searching for LL neutral particles decaying to photon using timing gives us a unique advantage compared to other experiments as we expect very limited background process contribution from SM. Most of our background will be detector originated contributions Infact, our search using lifetime gives us a wide range of search techniques depending on the lifetime of the LL particle ranging from quantitative measurements to statistics. The figure below shows the wide variety of techniques which can be used to search for LL particles in general.

$$\text{ADD figure of techniques for Searches using LL} \tag{2.68}$$

Using equations (2.65), precise measurement of fundamental parameters in SUSY or new physics can be archived. Another advantage is that, the our search for neutral particles is unique in that a lot of previous searches been performed for charged particles but very limited for neutral LL particles since DM is speculated to be made of stable neutral particle(s) with long lifetime, we might as well go for DM. We also use lifetime because no particle with lifetime $\gtrsim 10^{-7}$ s and mass $\gtrsim 1.5$ GeV has been found and obviously because our detector has a very good timing resolution as can be seen in the section of the CMS detector in this thesis.
There have been previous attempts to search for quasi-stable neutral massive particles

but all the search results show no evidence for neutral particles with long lifetime. The challenge with such an experiment is that neutral particles cannot be studied using conventional magnetic spectrometer as they are not affected by magnetic field because they are charge (local U(1) gauge symmetry) neutral. Nevertheless, there are countless theoretical as well as observational reasons why studying these particles using novel experimental techniques is very important in the field of particle physics. Some of these reasons will emerge naturally as we see in the subsequent sections below.

Theory Motivation.

Physics BSM can be summarized to answering three major theoretical questions: Is there a reliable explanation behind the ordering in mass of SM particles as observed? This is the Hierarchy problem. Is there a single theory which can provide a derivation for all the numerous parameters (19) in the SM and also unify all the fundamental forces of nature? Grand Unified Theories (GUT). What is DM and Dark Energy (DE)? (DE is the stuff that is responsible for the accelerated expansion of our universe). And finally being a particle physicist it is only natural to ask if DM is made up of particles and if yes, Can one construct a model which can consistently describe DM as is already the case with visible matter in SM?

Most of the efforts in the last decades in theoretical particle physics has been to find answers to the above questions.

Experiment and Observation Motivation

As early as 1956 Reines and Cowan[**?**] observed that when a neutron decays into a proton and an electron, an elusive particle called neutrino is also produced. The observation of neutrinos was later incorporated into the SM. In the formulation of the SM, the neutrinos are considered massless. However, recent results from experiments [**?**] have shown that neutrinos of different flavours can oscillate or mix into one another. The only way they can do this is if they have a tiny but finite mass. Recent experiments measuring the different neutrino flavours and their mass difference point towards the existence of a much larger theory that can incorporate the existence of neutrino masses and the observed phenomenon of neutrino mixing in which the SM is embedded in it and can be understood as a low energy version of a much broader and deeper theory.

Galactic and supernovae observations using the Hubble and a host of other telescope as well as results from Baryonic Acoustic Oscillation (BAO) and WMAP reveal unique matter content of our universe. In addition to these cosmological observations including galaxy profiles,cluster formation, large scale structure formation and Cosmic Microwave background (CMB) power spectrum can be somehow explained by DM [**?**]. These observation reveals about 25% of our universe is made of DM with the current DM relic density is measured to be However, the question of "What is DM?" remains a very interesting one to both the particle physics astronomy society. Understanding DM and the rest of our universe will be crucial for future developments in high energy physics from both theory and experimental fronts. A possible property of DM is that they must be made of up long lived neutral particles. There are candidate particles from SUSY which have these properties. A few of these include lightest neutralino ($\widetilde{\chi}_1^0$) and gravitino ($\tilde{G}$). From the GMSB point of view, because gravitinos are stable, neutral and very weakly interacting; they are seen as good candidates for the particles which make up DM.

2.4 Previous Experiments and Results

The hunt for the discovery of DM and new particles, has led to several experimental search for neutral long-live particles decaying to photons. Obviously, negative results from these experiments has led to the putting limits of the lifetime, mass and cross section of possible existence of SUSY particles in different models of SUSY. Results from experiments(DO, CDF, CMS and ATLAS)[**?**, **?**] in the search for Neutralino NLSP decaying to photon and gravitino and interpreted within the Snowmass Point and Slop (SPS)8 benchmark[**?**] scenario with parameter set be seen in figures 2.3(a) and (b). These results show that within the SPS8 model, neutralinos with mass $m_{\widetilde{\chi}_1^0} \leq 245$ GeV and proper decay length $c\tau_{\widetilde{\chi}_1^0} \leq 6000$ mm cannot exist at hadron colliders and thus their existence has been excluded.
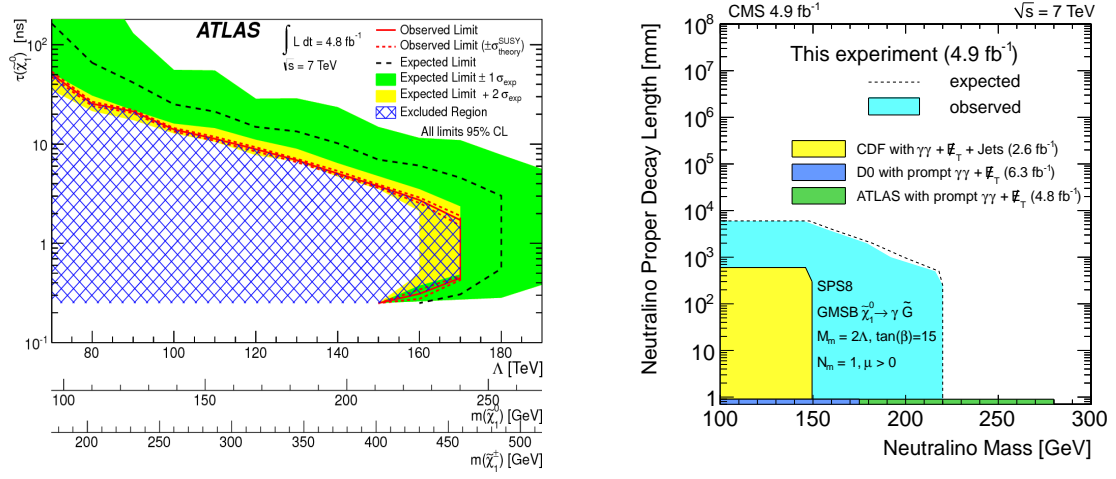
Figure 2.8: Neutralino lifetime and mass upper limit from ATLAS(left) and CMS(right) 7 TeV analysis with non-pointing photons and MET.

Chapter 3

Hadron Collider and Detector

This section describes the particle accelerator and detectors that are used to produced and detect particles at colliders. The first section describes the particle accelerator while the following section describes the CMS detectors with emphasis to those sections which are directly relevant to this analysis. A detailed description of the LHC and detectors can be found in [20] and [?].

3.1 Large Hadron Collider

3.1.1 Overview

The Large Hadron collider (LHC) is a proton-proton and heavy ion collider designed to achieve a center of mass $\sqrt{S}$ energy of 14 TeV. It is hosted and controlled by the European Organisation for Nuclear Research (CERN). Unlike linear colliders, the LHC is a circular collider with nearly 27 km in circumference located at the border between France and Switzerland. It is designed to smash protons and ions against each other controlled by powerful magnets at officially four main locations. At each major collision point are multi-purpose particle detectors ranging from A Toroidal LHC Apparatus (AT-LAS) and Compact Muon Solenoid (CMS) both non-fixed target detectors, A Large Ion Collider Experiment (ALICE) for colliding heavy ions and finally Large Hadron Collider beauty (LHCb), a fixed target experiment for investigating the properties of B-Hadrons. We give a full description of the important parts of the LHC in the following subsections,

detail discussion of other interesting parts can be found here [20]. There are three main steps prior to colliding protons or ions at the LHC. The first is ramping up the energy of the beams followed by squeezing the beams at interaction points(CMS or ATLAS) and finally remove the separator bumps that are formed by local corrector magnets. Thus our description of the LHC will follow this three stages.
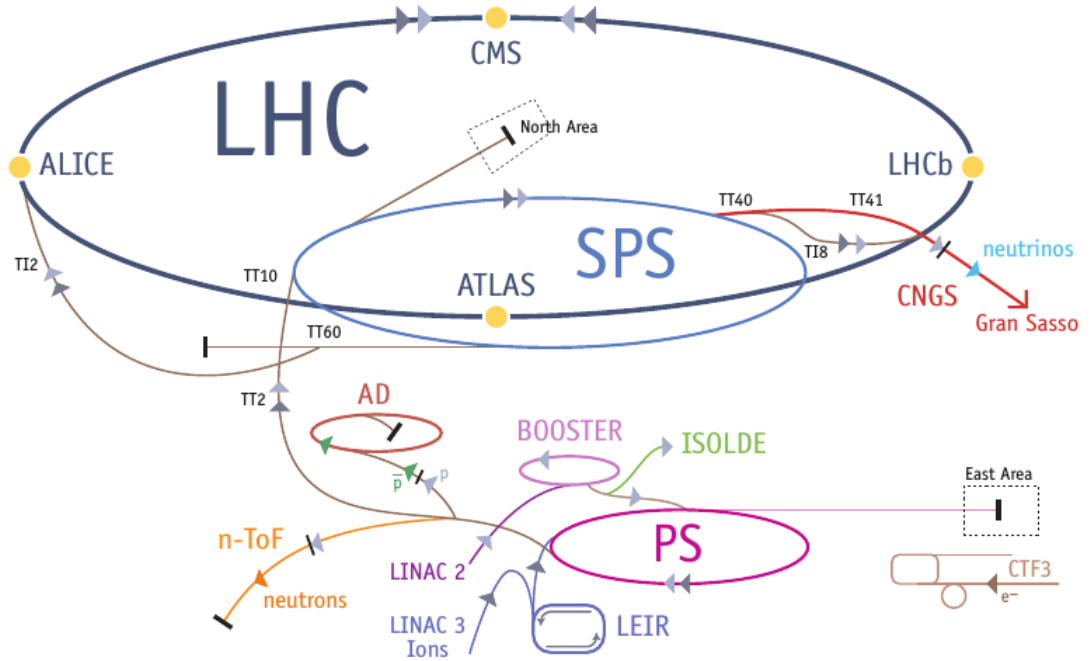
Figure 3.1: Schematic diagram showing the full Large hadron Collider. Image taken from [21]

3.1.2 Colliding Energy

Hydrogen gas is inserted into a linear accelerator called Linac2 where they are stripped off of their orbiting electrons to become hydrogen ions or protons. Under the influence of electric fields, these protons are accelerated to an energy of 50 MeV creating a stream of particles called *particle beams*. These beams are arranged in packets known as *bunches*. Particle acceleration if provided through the use of Radio-Frequency (RF) cavities containing electromagnetic fields which oscillate at a particular frequency. The protons surf this electromagnetic fields and are group in troughs of the electromagnetic

waves called RF *buckets*. The circular nature of the synchrotron accelerator ensures that the protons pass many times through a cavity and during each time their energy can be slowly increase to reach the design energy. The 50 MeV protons from the Linac2 are injected into the proton synchrotron Booster (PSB). The PSB accelerates the protons to up to 1.4 GeV and inject them into the Proton Synchrotron (PS) which pushes the protons energy to 25 GeV. These protons travelling at 99.93% the speed of light are sent to the Super Proton Synchrotron (SPS) and accelerated to an energy of 450 GeV. They are finally transferred into the LHC ring(both in a clockwise and anti-clockwise direction) and accelerated for about 20 minutes to their norminal energy of 7 TeV. As this point these protons are travelling with the speed of 99.9999% the speed of light. Powerful magnets are used to keep the beeps travelling in the circular LHC ring. The advantage of circular particle colliders such as the LHC over fix target colliders is that, the energy available to make new particles called the center of mass energy denoted as $\sqrt{S}$ is simply the sum of the energy of the two beams i.e $\sqrt{S} = E_{\text{beam1}} + E_{\text{beam2}}$ compared to $\sqrt{E_{\text{beam}}}$ for fix target experiments. In the case of the LHC, each beam is designed to have energy of 7 TeV and that makes $\sqrt{S} = 14$ TeV. Although in circular collider, an accelerating charge particles like the proton would loose energy in for the form of radiation which is inversely proportional to the mass of the charge particle to the fourth power requiring the need for continuous addition of energy after each turn to maintain the beam energy to a stable value. Since the proton's mass is about 0.938 GeV which is close to 1 GeV, this lost of energy is not very significant unlike electrons whose mass of about 0.000511 GeV making their energy lose through radiation more and thus less preferable to use as the main particles for a circular hadron collider. However, the debris of particles produced when electrons collide is much less compared to that of hadrons making analysis in a hadron collider more challenging.

3.1.3   Luminosity

Luminosity is the measurement of the number of collisions that can be produced in a collider per squared area per second. This is known as the instantaneous luminosity and it is related to the cross-section(a probabilistic measure of the possibility of a given collision process happening) through the equation:

$$N_{\text{events/sec}} = \text{Luminosity} \cdot \text{Cross Section} \qquad (3.1)$$

where the luminosity $\mathscr{L}$ is related to the total integrated luminosity(delivered luminosity over time) $\text{L} = \int \mathscr{L} dt$ and is defined in terms of accelerator(assuming round beams and equal values of beta function) parameters as:

$$\mathscr{L} = \frac{1}{4\pi} \cdot (f_{rev} n_b N_b) \cdot \frac{N_b}{\varepsilon_N} \cdot \frac{\gamma}{\beta^*} \cdot \mathscr{R}(\theta_c, \varepsilon, \beta^*, \sigma_z) \qquad (3.2)$$

where N_b is the number of particles per bunch, n_b is the number of bunches, f_{rev} is the revolutionary frequency, $\gamma = E/m_p$ is the relativistic factor, ε_N is the normalised beam emittance which along with β^*, the value of the amplitude or beta function at interaction point, determines the size of the beam. $\mathscr{R}$ is the geometrical reduction factor arising from the fact that the beams to not collide head-on but at a non-zero angle called the crossing angle or "Piwinski angle"($\phi \equiv \frac{\theta_c \sigma_z}{2\sigma_x}$). This effect is known as the *hour-glass effect*. From the above definition 3.2, it is evident that keeping the emittance (meaning particles in beam are confined to a small distance and have nearly the same momentum) means the likelihood of particle interaction will be greater and thus higher luminosity. However this is often not easy to archive as increasing the beam energy means reducing the beam emittance. The normalized emittance ε_N is often used as its dependence on beam energy is a squared root dependence. In the same way, lower beta values implies the width of beam is narrower or properly "squeezed" at interaction point resulting to an increase in number of collisions hence higher luminosity. This squeezing of depends on the quadruple magnet configuration and powering. In addition to low beam emittance and lowest value of beta function at interaction point(β^*), one can also archive higher luminosity by using high population bunches(N_b) and collide them at high frequency.

Luminosity Measurement   Obviously using equation 3.2 to determine the instantaneous and integrated luminosity would involve a lot of uncertainty in the measurements of about 20-30%, as there are so many parameters whose value need to be measured precisely in a normal LHC operation. Rather specialised LHC runs known as "Van der Meer Scans"[?] are used to calibrate specialized equipments used for determining luminosity. The method employed by CMS is using the Hadronic Foward (HF) calorimeter

to make luminosity measurements. Using production rates or cross sections of well and precisely calculable processes and rewriting 3.2 as:

$$\mathscr{L} \equiv \frac{Rate_{tot}}{\sigma_{tot}} = \frac{\mu n_b f_{rev}}{\sigma_{tot}} \tag{3.3}$$

where $\mu = \langle N_{tot}/n_b \rangle$ is the *average number of interactions per bunch crossing*. CMS keeps track of "recorded" and "delivered" luminosity. Delivered luminosity refers to the luminosity delivered by LHC to CMS and one would expect this to be equal to the amount recorded. However, there are instances where the CMS detector is unable to take data either because the data acquisition chain (DAC) is busy or one of the CMS sub-detectors is temporarily down. Part of my job as a sub-detector expert during CMS data taking of LHC Run 1 was to make sure that the period of temporal unavailability of the ECAL sub-detector is as minimal as possible.
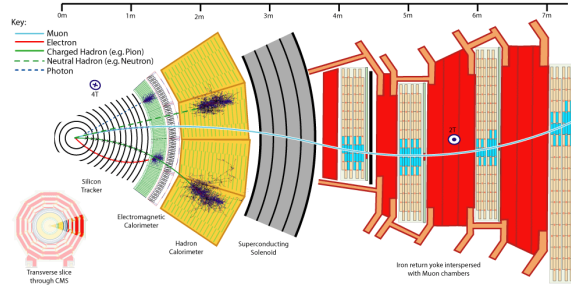
Figure 3.2: Recorded luminosity by CMS detector and LHC delivered luminosity in days/months during LHC Run 1 2012 operation.

3.1.4 Superconducting Electromagnets

The LHC design and operation uses a total of 9593 powerful magnets of different types for different purposes. Since there are two beams of protons running in clock-wise and anti-clock wise directions, the LHC uses an ingenious technique design of the magnetic field in every dipole magnet generates a vector field $\mathbb{B}$ in each pipe pointing in opposite direction to that of the other but both always perpendicular to the beam directions. The Lorentz or magnetic force acting on the protons in both pipes always point towards the center thus keeping the beams in circular motion. In circular accelerators as the LHC and its smaller synchrotron rings, given the accelerator radius, R, the beam energy p is determined by the strength $\mathbf{B}$ of the magnetic field. This can be easily understood

using the Lorentz force such that $p[TeV] = 0.3\mathbf{B}[T] \cdot R[km]$. The LHC is is a 26.659 km in circumference machine using powerful dipole magnets with magnetic field strength of about 8.33 Tesla(T) are 7 TeV to keep the protons circulating in their curved path or orbits. The LHC operates using superfluid helium for heat transport at 1.4 K(-271.3 $°C$) temperature to prevent these near 1232 dipole magnets, 858 quadruple and 6208 correcting magnets from overheating due to the energy stored in these magnets. Conventional magnetics aren't convenient for modern particle accelerators with high center of mass energy for both performance and economic reason. Rather, superconducting magnets made with modern technology using niobium-tantanium (Nb-Ti) filaments strands or cables are used to provide the high magnetic field required.

Quadrupole electromagnet and correcting magnets are used to keep the particles in the beam and archive the required focus and de-focusing needed. At interaction point, the quadrupole magnets are held symmetrically around the beam pipe to help squeeze the proton beams to very low values of beta function thus ensuring that many particle collisions as possible necessary for higher luminosity.

3.1.5   Timing

The Large Hadron Collider (LHC) is designed to collide proton-proton (pp) bunches every 24.95 ns at designed luminosity. This means, the distance between each proton bunch is about 7.5 m compared to the nearly 100 m of optical fibre length which is required to transport readout information from the very front end electronics on the detectors to the back end electronics at Point 5 for processing. It is therefore imperative to have a data synchronisation system for the trigger and readout systems of the LHC experiments in order that events from every proton-proton collision are properly assigned to the particular bunch crossing (BX) which produced them. The LHC is equipped with a Timing, Trigger and Control (TTC) system with a bunch clock frequency of 40.07897 MHz whose function is to distribute synchronized LHC time to all the detectors including CMS. Timing synchronisation in the LHC is achieved using a Beam Synchronous Timing (BST) system which distributes timing using the LHC revolution frequency(at 11.246 kHz) or LHC orbit and the RF bunch crossing frequency(40.07897 MHz at 7 TeV). Thus, the LHC fast timing signals from the RF generators of the machine and orbit signals are distributed from the Prevessin Control

Room (PCR) through single-mode optical fibers(about 10.1 km in length for CMS) to all LHC experiments, test beam areas, beam instrumentation around the ring and the SPS transfer lines. At CMS counting room, the LHC clock and orbit signals are recovered in the TTC Machine Interface crate (TTCmi) and later distributed to the Trigger Control and sub-detector master TTC crates. All Level1 (L1) trigger and Data Acquisition (DAQ) pipelines are driven with a 24.95 ns cycle clock locked to the LHC machine clock. The phase difference between the LHC 40 MHz clock and the arrival of detector signals from collision to the front-end electronics must be determined and adjusted for and monitored. The determination and assignment of pulses to bunch crossings depends critically on this initial clock phase adjustments and stability. This amplitude or pattern(also known as trigger primitives) for each trigger and bunch crossing is transmitted to the regional trigger logic in digital form every crossing and is synchronised with the LHC clock. Each trigger primitive digital data is then assigned to clock cycle in a process known as bunch crossing assignment. a Detail expert description of LHC unified timing distribution system can be found here [24, 25, 26, 27].

LHC Operation Parameters 2010-2013				
Parameter	2010 value	2011 Value	2012/13 Value	Design Value
Beam energy[Te]	3.5	3.5	4.0	7
β^* in IP 5[m]	3.5	1.0	0.6	0.55
Bunch spacing [ns]	150	75/50	50	25
Number of bunches	368	1380	1380	2808
Protons/bunch	1.2×10^{11}	1.45×10^{11}	1.7×10^{11}	1.15×10^{11}
Normalised emittance[mm.rad]	≈ 2.0	≈ 2.4	≈ 2.5	3.75
Peak luminosity[$cm^{-2}s^{-1}$]	2.1×10^{32}	3.7×10^{33}	3.7×10^{33}	1×10^{34}
Evts/bunch crossing	4	17	37	19
Stored Beam energy(MJ)	≈ 28	≈ 110	≈ 140	≈ 362
Int. Luminosity by CMS[pb^{-1}]				–
Circumference[km]	26.659	26.659	26.659	26.659
Dipole Magnet B[T]	8.33	8.33	8.33	8.33

Table 3.1: The LHC operation parameter conditions during RUN 1:2010-2013

LHC Bunch Structure

An LHC orbit is made of about 3564 *bunch* places. However only 2808 are occupied with protons. The bunch structure is archived by breaking a continuous proton beam into pulsed beam of separate bunches using an electromagnetic field with oscillating frequency of 400 MHz(LHC ring) in the SPS and LHC RF cavity. Thus each bunch is in an RF bucket. Each RF bucket has an energy against time profile as can be seen in figure below. The LHC filling scheme is arranged such that not all RF buckets have proton bunches. Thus there are empty buckets or beam gaps with missing bunches. These gaps are necessary to make room for the rise/fall times at SPS/LHC injection and ejection and abort kickers magnets during say LHC beam dump. The time separation between two buckets/bunches filled or unfilled is about 2.5 ns. Filling and acceleration at each RF cavity point is performed so that there are about 10^{11}protons/bunch. However, during filling and eventual bunch splitting at the PS, it is possible that some empty buckets are filled with a much smaller proton population compared to the main bunch. These less proton populated buckets can be $\Delta t = 2.5, 5.0, 7.5, \ldots$ ns, trailing the main bunch labelled as Beam1 or Beam2 otherwise leading the main bunch with $\Delta t = $ -2.5, -5.0s, -7.5, $\ldots$ ns. If these less populated bunches are 2.5 ns spaced in time from each other, they are referred to as *Ghost* bunches and if 5.0 ns, they are referred to as *satellite* bunches see figure (3.3).
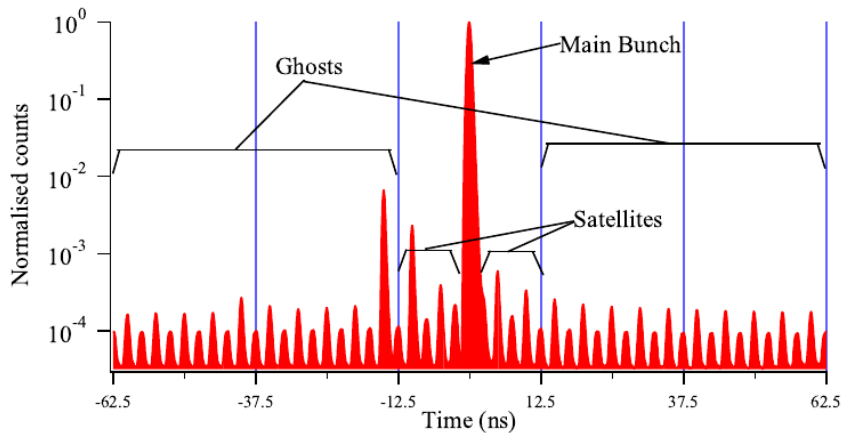
Figure 3.3: Longitudinal Profile taken with LDM detector showing definition of Ghost/Satellite bunches with respect to main bunches.

The presence of ghost/satellite bunches increase the uncertainty in LHC luminosity measurements and can also generate proton-proton interactions in the collision region. Effects on ghost/satellite bunches on instantaneous luminosity measurements have been studied by both CMS, ATLAS and ALICE detectors [**?**] with their profile compared to main bunch bunches. CMS uses energy deposits in the endcap calorimeters with time space equivalent to those of ghost/satellite bunches while in ATLAS, they have also introduced a new detector called the Longitudinal Density Monitor (LDM) to study ghost/satellite bunches. The results are shown in the figure (3.4).
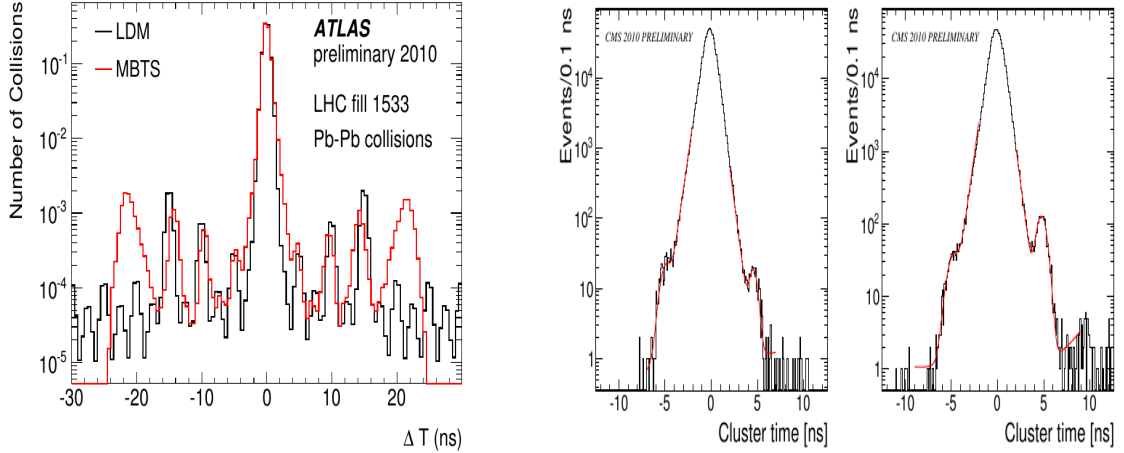
Figure 3.4: (left) Arrival time distribution(red) of ATLAS MBTS for LHC fill 1533 during 2010 Pb-Pb run and LDM profile(black) for Beam2(same for Beam1).
(Right) Timing of Clusters in the CMS endcap calorimeters for fill 1089:Left: EEP detector(left side of IP $z < 0$) Right: EEM detector(right side of IP, $z > 0$). NB: Plots taken from [29] and [30]

There is the possibility that ghost/satellite - ghost/satellite and ghost - Beam1/Beam2 collisions will happen generating events at the CMS detector. This is a major background in the search for delayed photons or objects in general as these collisions can occur *in-time*(Beam1- Beam2) collisions or *out-of-time* collisions. It is thus imperative to be able to quantify this contributions in any search analysis. We will show in future studies we have performs to both *"guestimate"* and quantify these contributions in our search analysis.

Beam Halo

In addition to ghost/satellite bunches generating collisions events during collision, protons in ghost/satellite bunches can interact with collimators or gases such as H2, CO_2 and others in the beam pipe leading to the production of high energy muons which later bremsstrahlung and shower directly in the calorimeter detectors. Main bunches due to betatron oscillations(departure of particles from nominal orbit in the transverse direction) can also through inelastic scattering with gas molecules in beam pipe about 550 m up from interaction point (IP)(since beam cleaning in not being 100% efficient), scattering on tertiary collimators (TCT) about $z = 150$ m from IP and beam dump at about 150 m upstream CMS detector, produce through cascade decay energetic muons(sometimes muons with about 1 TeV) which bremsstrahlung in calorimeter detectors.

This kind of background from beam is referred to as *Machine Induced Background* (MIB) or *Beam-Induced Background* (BIB) and its contribution is called non-collision backgrounds as these are events observed in the detectors but not produced from the interaction point (IP). Throughout these thesis, we will refer to this kind of events as *Beam Halos or halos*. Because, they produce very high transverse momentum photons which can also be miss-identified as jets arriving in-time of out-of-time, they are a very important background in any analysis. In the later section, we will also show how we have developed new methods to identify and reject these kind of events and estimate its possible contribution to our analysis.

3.2   Compact Muon Solenoid

3.2.1   Overview

The goal of the Compact Muon Solenoid (CMS) detector is to identify particles by measuring their energies, momenta and track if applicable, as they pass through the detector. It is for this reason that the CMS apparatus is a general purpose particle detector operating about 330 feet underground at point 5 (P5)LHC in cessy,France. Its main feature is a superconducting solenoid of 6 m internal diameter providing a field of 3.8 T necessary for good momentum resolution. This field encloses and all-silicon pixel serving as a vertex detector and a strip tracker for charged particle track reconstruction,

a lead-tungstate scintillating-crystals electromagnetic calorimeter (ECAL) and a brass-scintillating sampling hadron calorimeter (HCAL). Very long lived particles like muons are measured in gas-ionization detectors embedded in the flux-return iron-yoke located at the outermost section of the detector. It has a simple cylindrical structure consisting of barrel and endcap detectors and an extensive forward calorimetry and detectors to provide a near 4π solid angle assuring good hermetic coverage The CMS apparatus has an overall length of 21.6 m, a diameter of 14.6 m, and weighs 12,500 tonnes.
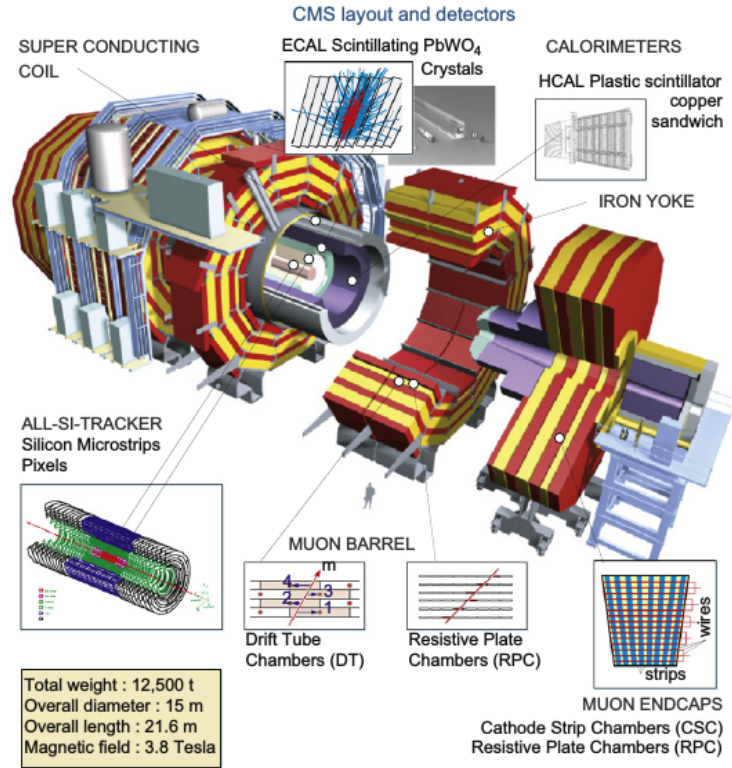
Figure 3.5: CMS Detector showing the different subdetectors and their material.

The CMS detector performance can be summarised as seen in table (4.0.11) with the material type in each sub-detector.

CMS Detector and Resolution			
Subdetector	**Quantity**	**Resolution**	**Uses**
Tracker	Momentum[GeV/c]	$\sigma_T/p_T \approx 1.5 \times 10^{-4}p_T + 0.005$	Silicon Pixels and Strips
ECAL	Energy[GeV]	$\sigma/E \approx 3\%/E + 0.003$	PbWO$_4$ Crystals
ECAL	Time[ns]	$\sigma(\Delta t) = \frac{N}{A_{eff}/\sigma_n} \oplus \sqrt{2}\bar{C}$	PbWO$_4$ Crystals
HCAL	Energy[GeV]	$\sigma/E \approx 100\%/E + 0.05$	Brass + Scintilator
Muon Chambers	Momentum[GeV/c]	$\sigma_T/p_T \approx 1\%$ 50 GeV to 10% 1 TeV	inner tracker + Muon Systems
Magnetic field	B-field strength[T]	3.8 T + 2 T	Solenoid + Return Yoke
Triggers	On/Off-line	Levels	L1(On-line) +HLT(Off-line)(L2+L3)

Table 3.2: CMS Detector Material and Resolution(Time resolution: $N \approx 35$ ns, $\bar{C} \approx 0.020$ ns [**?**])

The CMS uses a coordinate system where the origin coincides with the center of the detector also known as the nominal collision or interaction point (IP). The direction of x, y, and z-axis with the z-axis pointing towards the Jura Mountains from P5 are shown in figure (3.2.1). A more convenient coordinate system used in expressing quantities of particles is the polar coordinates. Here, the CMS uses the azimuthal angle *phi* measured from the $x - y$ plane with $\phi = 0$ being the x-axis and $\phi = \pi/2$ the y-axis. The radial distance in this plane is denoted R and the polar angle *theta* measured from the z-axis is related to the *pseudo-rapidity*, η through the relation:

$$\eta = -\ln\tan(\frac{\theta}{2})$$

. The co-ordinate system (η, ϕ, z) and its radial distance R defines a point in the CMS detector whose volume is a cylinder.
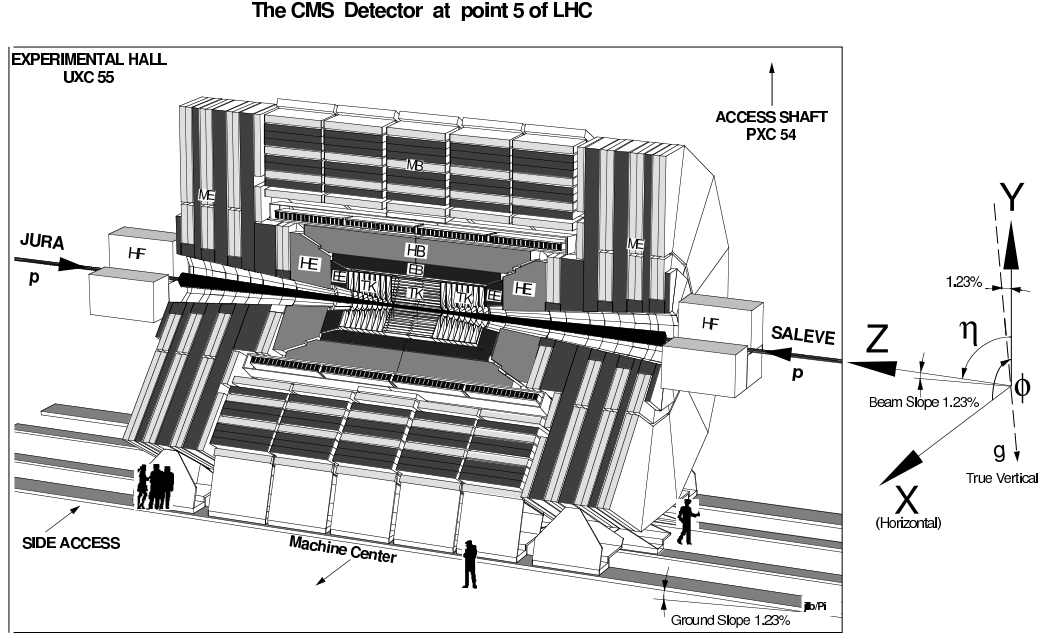
Figure 3.6: Schematic diagram of CMS detector view showing definition of cordinates as used by CMS.

In CMS, quantities such as *transverse momentum* (p_T), *transverse energy* (E_T) and *transverse missing energy* $(E_T^{\mathrm{miss}}$ or MET $)$ are used to distinguish a particle's quantities in the transverse plane($x - y$ coordinate) from those along the longitudinal direction(z coordinate) or beam line. In addition to these transverse quantities, cone-like structure with the cone radius is defined as

$$\Delta R = \sqrt{\Delta\eta^2 + \Delta\phi^2}$$

are used to measure the distance between two objects in the $\eta - \phi$ plane. These cone-like structures are used for particle isolation and identification purposes. In the next sections, we describe the characteristics and functionality of each of the CMS subdetectors introducing some additional details for those used in our analysis.

3.2.2   Tracker

Particles produced from proton-proton collision traverse the tracker sub-detector first. The job of the tracker is to measure the trajectory of charged particles, which are curved because of the magnetic filed produced by the magnetic coils. By measuring the curvature of these particle, the particle's momentum can be measured and its charge determined. The tracker is a silicon based detector and thus operates under the concept of ionization. It occupies a volume of 2.4 m in diameter and 5.4 m in length, consisting of pixel and strip sections geometrically arrange in cylindrical layers of barrel and disc-shaped endcaps, enclosed within the calorimeters. These sub-detectors all sit inside the 6 m in diameter solenoid magnet operating at 3.8 T. Figure (3.7) depicts a schematic picture of the tracker with three barrel layers covering a region of radius from 4 cm to 15 cm in radius and two endcap discs within 49 cm on either side of the collision point along the z axis; ten barrels layers and twelve endcap disks per side of silicon strip detectors covering a region with radius from 15 to 110 cm and within 280 cm on either side of the LHC beam axis. The total tracker acceptance region in pseudo-rapidity is $|\eta| < 2.5$. The pixel detector is used for identifying the primary and secondary vertices of particles while the inner tracker of strip detector is for tracker reconstruction.
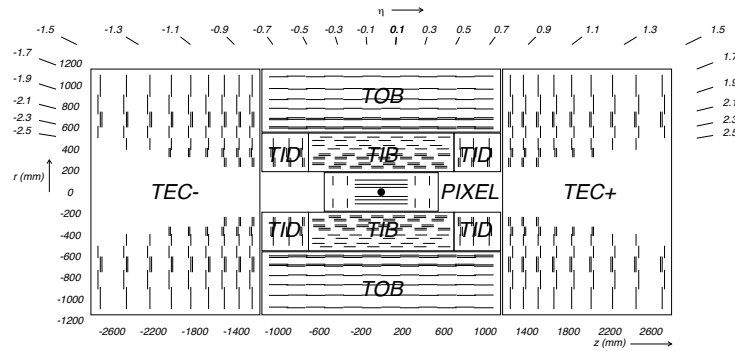
Figure 3.7: Schematic diagram of CMS Tracker showing the silicon pixel detector region (inner closer to LHC beam) and silicon strip reigion (outer).

Pixel

The pixel vertex detector occupies the inner most region, very closed to the interaction region. Providing high-resolution and three-dimensional patterns of space points using

silicon pads as pixels, the primary vertex and secondary vertices arising from the decay of heavy and relatively long-lived particles such as B-mesons containing b-quarks can be identified. This is also known as impact parameter measurements. The pixel covering a region of pseudo-rapidity $|\eta| < 2.4$ compliments the track finding by providing additional space points to seeding hits in the inner tracker. Each pixel has a size of $100 \times 150\ \mu m^2$ covering a total area of $\approx 1\ m^2$ and there are 66 million pixels read out by 16000 readout chips on the silicon sensors. The pixel is organised in three 53 cm long barrel layers (Pixel Barrel=PXB), positioned at radii of 4.4, 7.3 and 10.2 cm and two disks each per side (Pixel Forward=PXF), placed at ±34.5 cm and ±46.5 cm from the interaction point and covering a radii between 6 and 15 cm. This guarantees each charged particle track crosses at least two layers of pixels. This arrangement ensures that the pixel detector provides precise tracking points in the $r-\phi$ and z responsible for small impact parameter resolution of about $\sim 15\ \mu m$. Small impact parameter resolution is important for precise secondary vertex reconstruction and position resolution crucial in the identification of objects produced with displaced vertices with life-time of about $\tau \approx 10^{-12}\ s$ like mesons such as $B^{0,\pm}$, $D^{0,\pm}$, $\tau^{\pm}$, which may travel a distinguishable distance ($c\tau \approx 100\ \mu$m before decaying. Because of very high radiation dose of about 100 Mrad absorbed by the pixel detector, there is currently upgrade of the complete pixel detector in preparation of LHC Run 2.

Silicon Strip Tracker

CMS silicon inner tracker surrounding the pixel detector allows for the tracks of promptly produced charged particles with $p_\mathrm{T} = 100 GeV/c$ to be reconstructed with a resolution in the transverse momentum p_T of about $\sim 1.5\%$. High momentum particles are less curved by the magnetic field than low momentum particles. Therefore, the tracker works complimentary with the calorimeter and muon detectors to ensure improve momentum resolution at all particle energies. The silicon micro strip tracker covers a tracking volume up to radius of 1.2 m with a length of 5.6 m. It is organised in three parts: The inner tracker with four barrel layers (Tracker Inner Barrel=TIB) and three disks per endcap (Tracker Inner Disks=TID), 6 outer barrel layers (Tracker Outer Barrel=TOB) closed by 9 wheels on both sides. (Tracker EndCap=TEC). The silicon strip is made of 15148 silicon microstrip detector modules. Each module has a set of sensors. It occupies

an active area of 200 m^2 providing a coverage in pseudo-rapidity up to $|\eta| < 2.5$. The TIB/TID delivers up to 4 $r - \phi$ measurements on a trajectory using 320 μm thick silicon micro strip sensors arranged parallel to the beam direction in the barrel and radial on the disks. The strip pitch is 80 μm on layer 1 and 2 and 120 μm on layer 3 and 4 of the TIB, leading to a single point resolution of 23 μm and 35 μm, respectively. The TID also have varying pitches with both the TIB/TID enclosed by the TOB. The layering structure can be seen figure (3.2.2). The nearly 9.6 million silicon strips provide a spatial resolution measured to be about 10 μm for $r - \phi$ measurement and about 20 μm for z measurement necessary for particle trajectory reconstruction. The combined pixel and micro strip modules allows for nearly 75 million readout electronic channels in the tracker.

3.2.3   Calorimeter

A calorimeter is a device which absorbs a good fraction of energy of an incident particle and produces a signal with an amplitude proportional to the energy absorbed. This absorption is via a cascade production of secondary particles where the incident energy is directly proportional to the number of secondary particles. CMS uses two types of calorimeters: Electromagnetic calorimeters (ECAL) for absorbing the energy of electromagnetic particles such as photons and electrons and a sampling calorimeter or Hadronic calorimeter (HCAL) made of more than one type of material for absorbing the energy of hadrons such as kaons and pions through hadronic interactions. The combined calorimeter detectors of CMS covers a region in $|\eta| < 5$ making it nearly hermitic for missing energy measurements. The ECAL and HCAL are arranged in a layered manner as seen in figure (3.2.3) such that electromagnetic particles can be distinguished from hadronic particles by comparing the depth of the particle shower penetration in both calorimeters.

Figure 3.8: Schematic diagram of CMS calorimetry system with HCAL enclosing ECAL in the Barrel and Endcap regions.

Electromagnetic Calorimeter

The main particles to detect using ECAL detectors are photons and electrons. High energy photons and electrons are detected through their interaction with the material of the ECAL detector. During this interaction which can be either through electromagnetic showering also known as *bremsstrahlung* or electron-positron pair production, the incoming photons or electrons deposit practically almost all of their energy. The material for the CMS ECAL detector are lead-tungstate ($PbWO_4$) crystals. There are 75848 lead-tungstate ($PbWO_4$) crystals mounted in a barrel (EB) and endcap (EE) structure. $PbWO_4$ crystal is the appropriate choice for calorimetry by CMS for operation in the LHC environment because of its a high density (8.28 g/cm^3), short radiation length (X_0=0.89 cm) and a small Molière radius (22 cm). This dense nature allows for the electromagnetic shower to develop early and therefore very likely to be fully contained within a compact device. In a high radiation dose and fast timing (25 ns bunch spacing) environment like the LHC, the choice of $PbWO_4$ crystals is justified because of their high radiation resistance and short scintillation decay time of the same order of magnitude as the LHC bunch crossing time:about 80% of the light is emitted in 25 ns. Since the 'amplitude" or "probability" of a high energy photon or electron interacting with an ECAL material through (*Bremsstrahlung*) and pair production is proportional to the nuclear charge or number of electrons, Z of the material, $PbWO_4$ which is a high Z material is once again CMS preferred choice for calorimetry. The small Molière radius of $PbWO_4$ crystals ensures that on average about 95 % of the electromagnetic shower

energy is contained within the crystal volume therefore reducing the transverse spread of the electromagnetic cascade arising from multiple scattering of electrons. This improves on the estimation of the transverse position of impact of the incident particle and the fine granularity provides good precision for measuring the energy of an incoming electromagnetic particle and thus better energy resolution.

The barrel section of the ECAL covers a pseudo-rapidity of $|\eta| < 1.479$. The EB has 61,200 crystals providing a granularity of 360-fold in ϕ and (2×85)-fold in η. The crystals are mounted in a quasi-projective geometry to avoid cracks aligned with a particle trajectories, so that their axes make an angle of 3% with respect to a line vector from the nominal interaction vertex in η and *phi* directions. These EB crystals have approximately 0.0174×0.0174 in $\eta - \phi$ or 22×22 mm^2 at the front face and 26×26 mm^2 on the rear face. each crystal is 230 mm long corresponding to about 25.8 X_0 radiation length. The crystals are contained in a thin-walled aveolar structure made with aluminium called submodule with their radial distance from the center of the face of the crystals to the beam line is 1.29 m. Each submodule are arranged into 4 modules of different types according to their η position with each module having about 400 to 500 crystals. The four modules make one supermodule containing 1700 crystals. The aluminium surface is coated to avid oxidation hence coloration which causes decrease in transparency. On the rear end of each EB crystals, is glued two Avalanche Photodiodes (APD) whose purpose is to collect the scintillating light from the crystals converting light into current which is further collected by the read-out electronics.

The endcap sector occupy a pseudo-rapidity region of $1.479 < |\eta| < 3.0$ with Preshower (ES) detector made of silicon strip sensors interleaved by lead placed immediately in front of it. The purpose of the preshower detactor is to help separate converted from unvonverted photons. There are two endcaps located in the $+z$ side of the nominal interaction and denoted EE+ and on the $-z$ side denoted as EE−. The longitudinal distance between the nominal interaction point and the center of the surface of the crystals in EE is 3.154 cm. Crystals in the EE are of identical shape group in units of 5×5 crystals called *supercrystals or SC*. Each endcap is divided into two halves called *Dees* with each Dee holding 3662 crystals. The crystals are arranged in $x - y$ grid with their front face and rear cross section of 28.62×28.62 mm^2 and 30×30 mm^2 respectively. Ecah crystal is 220 mm (24.7 X_o) in length. Vacuum Phototriodes (VPT) is glued on the

rear face of each crystal for scintillating light collecting and conversion into electrical signals. These photodiodes and triodes are used because of their high gain and the fact that they are not affected by the high magnetic field. Although the light-yield for $PbWO_4$ is rather low (≈ 70photons/MeV), the photodiodes have internal gain (50 for APDs and 10 for VPTs) and good quantum efficiency of 75% for APDs and 20% for VPTs of the emission wavelength. This makes it possible that signals from incident particles with energies from a few to high GeV can be recorded. APDs and VPTs are the standard choice of photo-detectors by CMS because of their high resistance to radiation and smooth operation in a strong magnetic field environment. Photodiodes like APDs and VPTs are similar to silicon photodiodes, with the exception that they have a buried p-n junction reversed-biased at a very high electric field. The photo electrons arriving at the junction undergo avalanche multiplication giving the device a gain. The signals from the APDs and VPTs are digitized by voltage-sensitive analogue-to-digital converters are later converted to light signals which are then transported using long optical fibres to the counting room located adjacent to the experimental cavern.

The energy resolution and geometric structure of the ECAL ensures that the photon or electron's arrival position at ECAL,energy and time and even the direction and shape of its electromagnetic shower in the crystals can be measured and identified respectively with good precision.
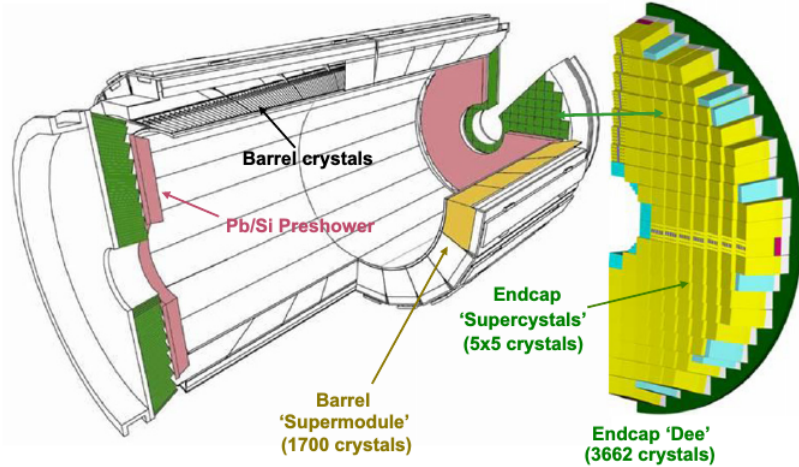
Figure 3.9: Layout of the CMS electromagnetic calorimeter showing the arrangement of crystal modules, supermodules in the barrel with the preshower infront of endcap with supercrystals.

Hadronic Calorimeter

Hadrons like protons, neutrons kaons and pions are unlike electromagnetic particle strongly interacting (strong force is the force that binds nuclei together). A hadronic shower is formed when an incident hadron undergoes an inelastic collision with the nucleus of the absorber material producing secondary hadrons which as they go through successive layers of absorber material interact inelastically with other nuclei to produce further hadrons etc. The hadronic cascade loses about 30 % of incident hadron energy through nuclear excitation of the nuclei of atoms of the absorber material. Hadronic showers start to develop later with more lateral spread and and larger in the longitudinal dimensions than electromagnetic showers. This is why the hadronic calorimeter (HCAL) is made of alternating plates of brass and plastic scintillator encompassing the ECAL. The scintiallating light is readout using wavelength shifting optical fibres by photosensors in the barrel and endcap. The photosensors are hybrid photodiodes (HPD). The are ongoing upgrades to replacing the HPDs with silicon photon multipliers (SiPM). The hadronic barrel(HB) and hadronic endcap(HE) of the HCAL cover a region in pseudo-rapidity of $|\eta| < 3$. While the Hadronic Forward (HF) occupies a pseudo-rapidity region of $3 < |\eta| < 5$. The HB calorimeter is an assembly of two half barrels each composed of 18 identical 20° wedges in ϕ. Each wedge is made of flat brass alloy absorber plate parallel to beam axis with the innermost and outermost layers made up of stainless steal interleaved by plastic scintillating tiles. The first active layer is situated directly behind the ECAL in order to actively sample low energy showering particles from the support material between the ECAL and HCAL. Each scintillating tile has a size of $\Delta\eta \times \Delta\phi = 0.087 \times 0.087$ and is instrumented with a single wave length shifting fiber(WLS) for better collection of light. The summed optical signals or light are converted into fast electronic signals by photo-sensors called hybrid photo-diode(HPD). This inhomogeneous design gives the HCAL, an energy resolution of $\Delta E/E \approx 0.5/\sqrt{E(GeV)}$ for particles with energy above 250 GeV, much lower compared to that of homogeneous ECAL detector.

The forward hadronic (HF) calorimeters placed upstream have scintillating tiles called Beam Scintillation Counters (BSC) which in coincidence with the beam pick-up monitors (BPTX) detector helps to eliminate beam background contamination at the trigger level and is also useful for detection of hadrons in the forward region. HF

made up of steel absorbers embedded in radiation hard quartz fibers running parallel to the beam axis and providing a fast collection of Cherenkov light. The signal results from Cherenkov light emitted in the quartz fibres embedded in the steel matrix in response to charged particles. The Cherenkov calorimeter have long and short fibers which are positioned alternatively separated by 5 mm with readouts for better sampling of the different shower components. The goal of this hardware design is to give better compensation for different shower components in the hadronic shower. The HF section enables the HCAL to pick up myriad of particles coming out of the collision point. Quartz fibre has high resistance to the high radiation does in the forward detectors and light production is through Chererenkov method than scintillation in HB and HE calorimeters.

The purpose of the HF detector is to provide a full hermetic 4π phase space coverage required for missing transverse energy calculation or MET. MET is the established as signal for very weakly interacting particles like neutrino and supersymetric particles like gravitino which travel through the detector undetected. For $|\eta| < 1.74$ region, the HCAL cells are $0.087 0.087$ rad in pseudo-rapidity(η) and in azimuth (ϕ). In the (η, ϕ) plane, and for $|\eta| < 1.48$, the HCAL cells map on to 5×5 ECAL crystals arrays to form calorimeter towers projecting radially outwards from close to the nominal interaction point. At larger values of $|\eta|$, the size of the towers increases and the matching ECAL arrays contain fewer crystals. Within each tower, the energy deposits in ECAL and HCAL cells are summed to define the calorimeter tower energies subsequently used to provide the energy and direction. The ratio of the energy deposit if a particle in the ECAL crystals to that in the HCAL towers is used to distinguished between true photons from neutral hadronic showers.

3.2.4   Muon Chambers

Muons are long-lived particles capable of travelling across the entire lateral section of the CMS detector into the muon chambers producing tracks in the tracker and depositing very little fraction of their energy in the calorimeters. The muon chambers uses ionization and the magnetic field from the return iron yokes to curve the tracks of charged long-live particles like muons, measuring their momentum and finally detecting them. There are three different types of muon chambers: the drift tubes (DT) chambers in the

barrel, cathode strip chambers (CSC) n the endcaps and resistive plate chambers (RPC) glued to the DT and CSC chambers. Four layers or stations of DT/RPC and CSC/RPC are embedded in an interleaved style with the iron yoke for track reconstruction and triggering. Figure (**??**) provides a longitudinal view of the CMS detector showing the position of the stations. The DT and CSC record track segments characterised by the position of the track and the bending angle which is used to determine the precise transverse momentum and charge of a given particle during off-line reconstruction. The RPCs are dedicated trigger chambers used to determine the candidate muon's approximate transverse momentum ad bunch crossing number where the particle originates. The RPC has a timing resolution of about 3 ns.
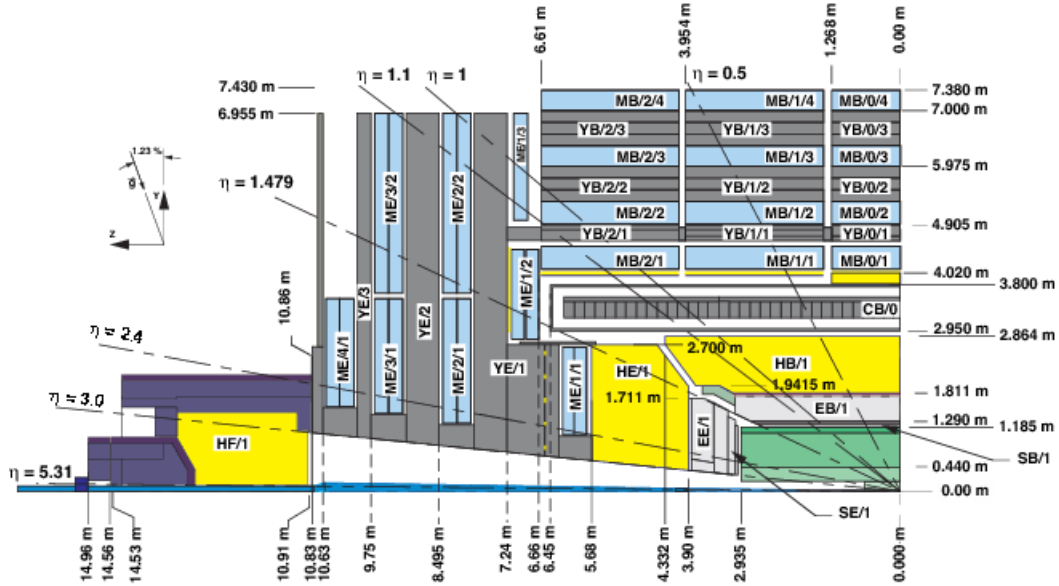
Figure 3.10: Longitudinal view of CMS showing the coverage range of its sub-detectors.

3.2.5   Particle Detection

Particle types that are identified using the CMS detector include electrons, photons, hadrons, muons, neutrinos and other weakly interacting particles. These particles depending on their charge, nature of interaction and lifetime can be identified either using some or all the sub-detectors of the CMS detector. The figure (**??**) show a transverse slice of the CMS detectors with tracks in the tracker and muon sub-detectors and calorimeter energy deposit showing how different particles interact with the material in

different sub-detectors thus ensuring their unique identification and reconstruction in the detector.
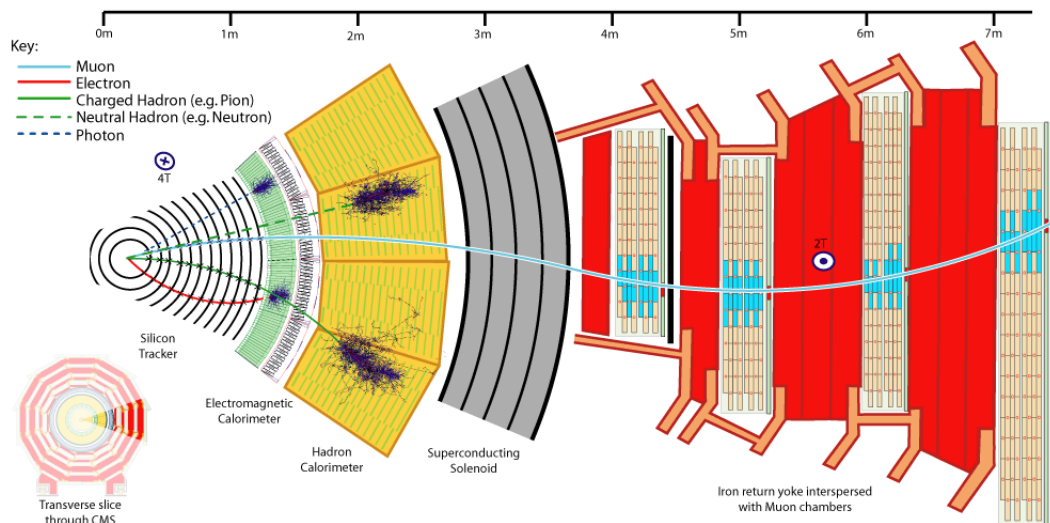
Figure 3.11: Transverse slice of the CMS detector showing how different types of particles interact and hence identified using this detector.

3.2.6 Triggering

In CMS, there are a billion interactions happening every second which means data from protons colliding 40 million times every second equivalent to the 25 ns LHC bunch crossing time interval has to be process and analyse before the next collision happens. Obviously this is impossible and infact, not every proton-proton collision will lead to the production of an interesting physics event. Thus one has to find a way of selecting only events produced from head-on proton collision with sufficient amount of energy. Even with this selection, it is not possible to process a single event in a 25 ns time frame. Thus, the CMS uses a two level triggering system for selecting interesting events and a pipeline system to temporarily store and process information from many interactions at the same time. Thus so as not to confuse particles from two different events, the CMS triggering system has a very good timing resolution and synchronization so that signals from millions of electronic channels and synchronised and identified to be produced by the same event. The CMS triggering system consist of two layers: The Level-1 (L1) and High Level Triggers (HLT) triggers. L1 triggers are hardware designed electronic

system while HLT is a farm of more than 1000 standard computers running the HLT event selection algorithm. Thus event selection begins at the L1 and HLT triggers. The L1 trigger electronics is implemented in FPGA and ASIC technology and consists of a calorimeter, muon trigger and a global trigger boards. The global trigger board makes the final decision based on the calorimeter and muon triggers to reject or keep and event for further processing at the HLT trigger. The L1 trigger is responsible for selecting the best 100,000 events each second from the initial 1 billions events from interactions happening every second. The pipeline system is used during the L1 trigger latency time of about 3.2 μs. The HLT trigger using assimilated and synchronised information from different parts of the detectors recreates the entire event. the HLT runs complex algorithm relating to physics objects like matching tracks to hits from the muon chambers or energy deposits above a certain threshold in the calorimeters without tracks for electromagnetic objects. By the time this selection process in complete, there are now only 100 events per second with the remaining 99,900 thrown away. With the average event size of about 1 Megabyte, in a stable and effective LHC proton collision year or 10^7 seconds, the CMS produces about a Petabyte of data which is stored in tapes for later offline analysis. Due to the large amount of data, such analysis are performed using clusters of computers geographically connected to each other in a virtual computing environment called the LHC Computing Grid (LCG) to which the CMS is a member. This data is made available to 7 primary and later to secondary tier centres consisting of national research laboratories and universities around the world using a data transport system term Physics Experiment Data Export (PhEDEx).

Chapter 4

Timing Reconstruction and Calibration

The time of an electromagnetic object such as a photon is extracted at the level of individual crystals called reconstructed hits (rechits). The recorded time of the photon is the crystal calibrated time where the Time-Of-Flight (TOF) as well as the time to transmit the recorded signal from the front-end detectors to the back-end readout electronics is removed such that on average the time is zero for a photon produced at the nominal proton-proton collision point and travelling at speed of light and then impinges at the surface of the crystal. There are separate algorithms for extracting and calibrating the crystals using the rechit time. This calibrated time is considered the reconstructed time (T_{RECO}). Measuring the difference in timing between any two reconstructed objects (individual crystals or electromagnetic objects) originating from the same nominal point and thus assumed in principle to have the same time give the timing resolution of the detector as well as the crystal-to-crystal synchronization factor. T_{RECO} of a photon can be defined in either of the following ways:

1. Seed Time: The time of the highest energy crystal or rechit in the highest energy basic cluster of the photon supercluster denoted as T_{SEED}

2. The Mean Time: This is the error weighted mean time of all the crystals in the

photon supercluster denoted as $T_{CLUSTER}$ or T_{MEAN} and is defined as follows:

$$T_{CLUSTER} = T_{MEAN} = \frac{\sum_{i=1}^{N} \frac{T_i}{\sigma_i^2}}{\sum_{i=1}^{N} \frac{1}{\sigma_i^2}} \tag{4.1}$$

where N is the number of crystals in seed basic cluster of photon supercluster.

4.0.7   Electromagnetic Calorimeter Readout Chain

The ECAL electronics readout system described in detailed in [35] is a light-to-light system. Energy from incoming electromagnetic objects is absorbed and converted into scintillating light by $PbWO_4$ crystals. This is received and converted into electrical signals by the avalanche photo-diodes. These electrical signals are digitized and finally converted back into light signals which is transported using optical fibres into the off detector electronics in the counting room at point 5. Thus one can easily classify the full readout chain of the ECAL electronics readout system as divided into an on-detector electronics and an off-detector electronics. Both electronics system are connected by a 100 m optical fibre links. A simple picture of the readout chain is shown in figFIXME:Fig readout Chain.

The on-detector electronics reads a trigger tower consisting of 5×5 crystals in $\eta \times \phi$ in barrel (EB) and *supercrystals* in endcap (EE). Five Very Front End (VFE) boards (reading out data from 5 crystals each), one Front End boad (FE) two (EB) and six (EE) Giga Optical Hybrids (GOH), one Low Voltage Regulator (LVR) board and a Mother Board (MB) make up the complete on-detector electronics. Electrical Signals from the APDs (EB) are accepted by the VFE which is equipped with a Multi Gain Pre-Amplifier (MGPA), a 12-bit Analogue to Digital Converter (ADC) and a buffer. The MGPA an Application Specific Intergrated Circuit (ASIC) developed in 0.25 μm technology, pre-amplifiers, shapes and then amplifies the signals through three amplifiers with gains of 1, 6 and 12. For VPT (EE), these signals first pass through a High Voltage (HV)filter card which acts as a moderator separating very high voltages caused by the increase radiation in the EE. The full scale of the APDs and VPTs are 60 pC and 12.8 pC corresponding to $\approx$ 1.5 TeV and 1.6-3.1 TeV respectively. The full shaping of the signal takes about 40 ns. The noise for gain 12 is about $8000e^-$

for APD configuration and about $4000e^-$ for VPT configuration. The 3 analog output signals of the MPGA are digitized in parallel by the multichannel 40 MHz, 12-bit ADC. This ADCs have an effective number of bits of 10.9. The highest non-saturated signal is selected as the output signal and reported as 12 bits of the corresponding ADC with 2 bits coding the ADC number. It is possible, that when the signal is saturated and wrong signal amplitude can be produced leading to am amplitude dependence of the readout time. This effect has been studied for Gain 1 and 6 transitions and the relevant corrections factors of timing produced and validated. A schematics picture of the showing the readout chain of the FE with its MPGA and ADCs showing the shaping and digitization process can be seen in figure (4.0.7).
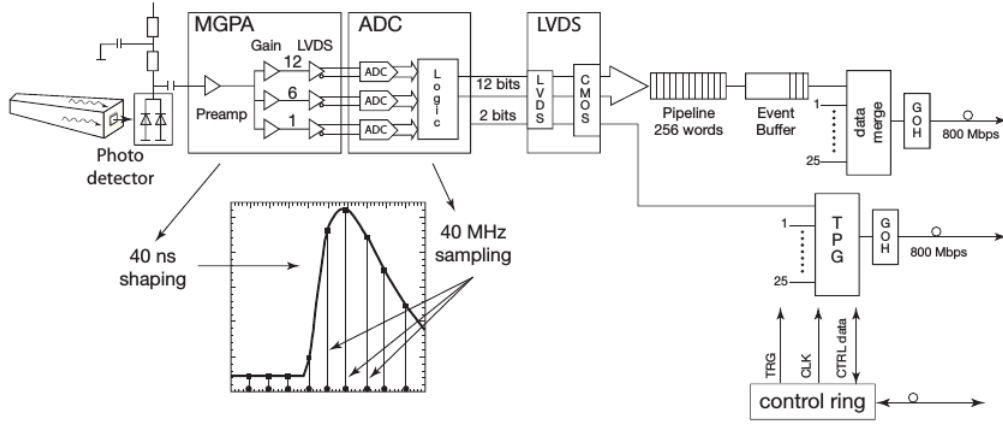
Figure 4.1: Schematic showing ReadOut Chain.

A radiation-hard buffer (LVDS) adapts a low voltage differential out put signal of the ADC to input into the FE. Signals from five identical channels are integrated and read into VFE card with a Detector Control Unit for measuring the APD leakage currents. The noise from each VFE is typically 1.1, 0.75, 0.6 ADC counts for gains 12, 6 and 1 respectively. This would be about 40 MeV for gain 12.

Digitized data from 5 VFE cards are fed into each FE through the LVDS and stored in 256-word-deep dual-ported memories called pipelines. Data pipelines can be stored for up to 128 bunch crossings. The FE is base on a ASIC called the FERNIX holding the logic to calculated the energy of 5 channels once every bunch crossing. This energy is summed in strips of 5 crystals along ϕ. Thus each VFE is serviced by a FERNIX

chip. In the case of the EE, the five strip energy sum are transported by GOH to the off-detector electronics Trigger Concentration Card (TCC) while for EB, there a sixth FERNIX which sums the five strips energy sums and calculates an electromagnetic bit which is used to identify electromagnetic shower candidates on the basis of their shower profile in a trigger tower. The trigger tower energy sums and the electromagnetic bit is transmitted to the TCC through the GOH. This process is referred to as Trigger Primitive Genration (TPG). Once a Level-1 trigger signal is received, the ten 40 MHz samples for each channel are transmitted to the off-detector electronics DCC using an identical GOH. This takes about 7.5 μs. The VFE and FE cards are controlled using a 40 MHz digital optical link system and controlled by the off-detector Clock and Control System (CCS). The Off-detector electronics consist of different types of electronic boards (the CCS, TCC and DCC modules) sitting in an 18 VME-9U crates and a 1 VME-6U crate holding the Selective Read-Out Processor (SRP). This system is serving both the trigger and the Data Acquisition Systems (DAQ) paths. In the DAQ path, the DCC performs data read-out and data reduction based on flags of the SRP. While in the trigger path, at each bunch crossing, the trigger primitive generation which began in the FE is finalised and synchronised or time alignments in the TCC before transmitted to the regional calorimeter triggers. The trigger primitives each refer to a single trigger tower (25 crystal data) and consists of the summed transverse energy deposits and the electromagnetic bit charactering the lateral shower profile of the electromagnetic shower. The accept signal for accepted events is return from the global trigger after about 3 μsand the selected events area read into the data acquisition system to the filter farm where the even rate is further reduced using data from the full detector. Thus is the regional calorimeter, the ECAL trigger primitives together with the HCAL trigger primitives are used to compute the electron/photon and jet candidates as well as their transverse energy. The resulting physics objects after passing through the HLT trigger are transferred to the various tier systems for offline full event reconstruction. The ECAL also has a laser calibration systems where laser light is delivered directly to the PbWO$_4$ crystals using optical fibres. The laser data is used for energy and time calibration of crystals and hardware system. The crystals are energy calibrated because of the decrease in optical transmission due to the formation of color centres in the crystal. The formation of color centres is caused by irradiation. Time calibration using

laser data is also required in case of hardware timing offset especially during long short down periods of the CMS detectors.

4.0.8   Timing Extraction

The MGPA of the VFE amplifies and shapes an analogue signal from the APD/VPT of a single crystal producing a typical signal pulse as seen in figure (4.0.8).
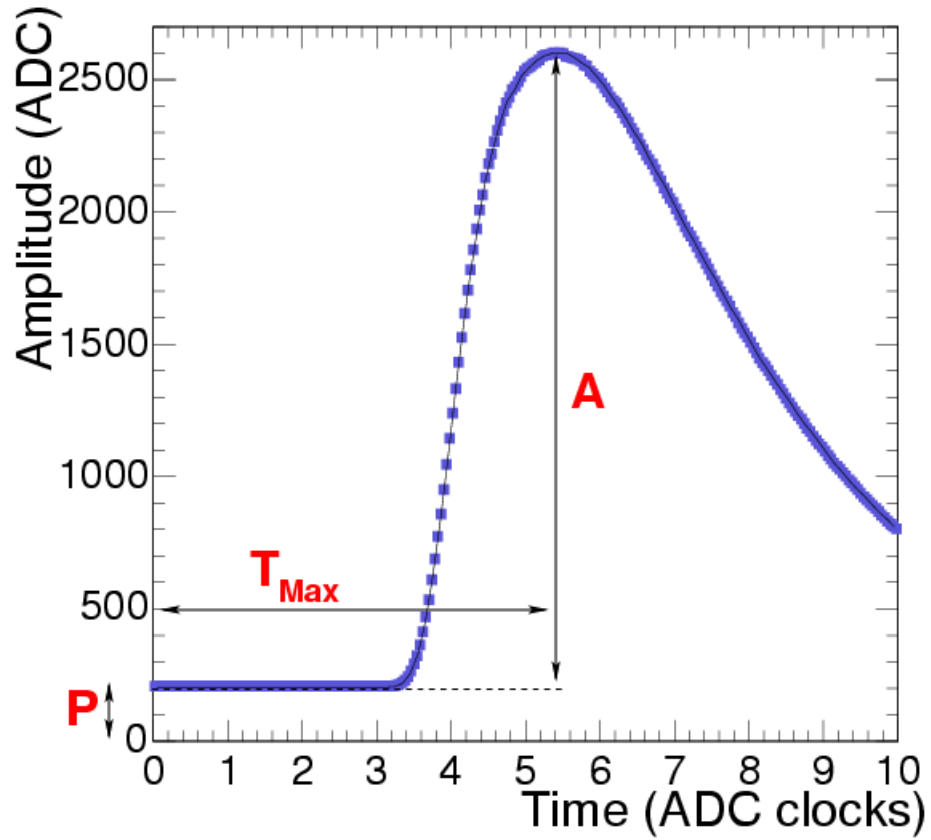
Figure 4.2: Typical pulse shape of a given signal showing signal amplitude and time.

This pulse is digitised into 10 samples by the ADC for data storage purposes. The pulse's amplitude is a measure of the energy deposited in the crystal while the time from the ADC clock with a sampling frequency of 40 MHz for 10 samples is used to extract the arrival time of the physics object depositing its energy unto the crystal. The value **P** is known as the pedestal or noise read as ADC values in the absence of

any signal. Using the 10 samples, a timing algorithm is employed to extract the time of arrival of particles to the ECAL. The goal of this algorithm is to use the maximum amplitude value of the pulse A_{MAX}, and extract its corresponding maximum value of the ADC time A_{MAX} as the time of arrival of the physics object to the crystal. Thus, ECAL timing reconstruction is defined as: Using the 10 samples of the pulse amplitude to measure T_{MAX}. Obtaining the true A_{MAX} is performed through an energy reconstruction algorithm. Extracting the arrival time is thus a matter of comparing the pulse shape obtained using the 10 samples of a scintillating channel's pulse to that of a reference shape. This reference shape is obtained from experimental measurements using Testbeam or synchronous LHC events. Figure (a) shows a distribution of the amplitude A as a function of time rather plotted for convenience as A/A_{MAX} on the vertical or y-axis and $T - T_{MAX}$ on the horizontal or x-axis. T is the time and T_{MAX} is defined as the time when the pulse reaches its maximum value, A_{MAX}
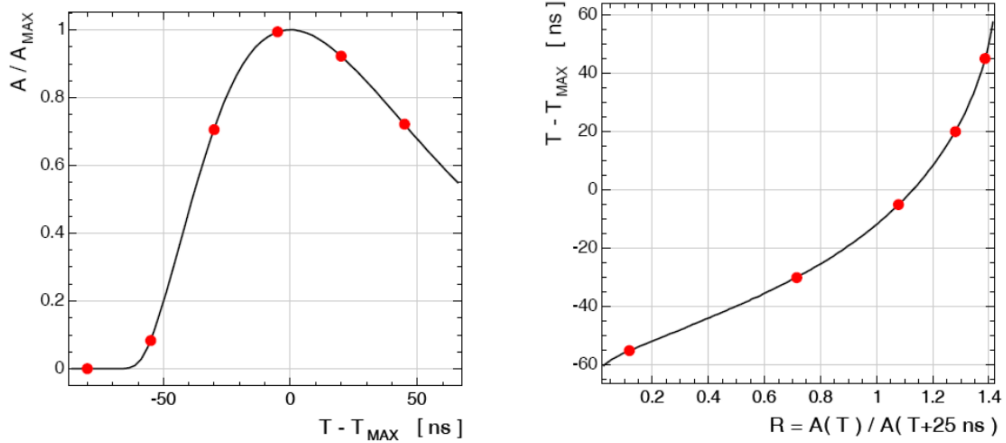
Figure 4.3: left: A measured ECAL pulse shape for each channel. Right: $T - T_{MAX}$ Vs $R(T)$ showing the distribution of $T(R)$. Solid line is reference shape or shape from testbeam while dots correspond to a 10 discrete samples corresponding to signal from a single event in a single channel or crystal.

Performing an analytical fit to compare the reference pulse shape to that from the 10 samples on the $A(T)$ distribution to obtain A_{MAX} and T_{MAX} is rather cumbersome and technically in efficient, as the amplitude of each sample depends on the pulse shape, the A_{MAX} value and also the relative position of T_{MAX} between time samples. This phase is referred to as "T_{MAX} phase". Thus, using a new variable defined as $R(T) = A(T)/A(T+$

25 ns) and instead perform an analytical fit on the distribution of $T - T_{MAX}$ Vs $R(T)$. This $T(R)$ distribution is independent on A_{MAX} and can be very well described by a polynomial of order 7. A distribution of $T(R)$ is shown in figure (4.0.8)(b) with both the four to five samples(dots) obtained from the ratio $R_i = A_i/A_{i+1}$ from each consecutive pair of samples and the reference pulse shape(continuous line). Thus each point R_i gives a quick accurate measurement of $T_{MAX,i} = T_i - T(R_i)$. The uncertainty, $\sigma_{T,i}$, on each measurement is a production of the derivative of the function $T(R)$ and the uncertainty on the value of R_i. The uncertainty on the value of R_i depends on three separate uncertainties: the noise fluctuation, σ_n of each sample, the uncertainty in the estimation of the pedestal value which is always subtracted from the measured value and the truncation during 12-bit digitization. These uncertainties are uncorrelated and can thus be added in quadrature. The reconstructed time and its error of a hit(fraction of energy deposited on a single crystal) is determine using the following equations:

$$T_{MAX} = \frac{\sum \frac{T_{MAX,i}}{\sigma_i^2}}{\sum \frac{1}{\sigma_i^2}} \quad ; \qquad \frac{1}{\sigma_T^2} = \sum \frac{1}{\sigma_i^2} \tag{4.2}$$

where the sum is over all the 4 or 5 R_i ratios and the assumption is that the weights are uncorrelated.

4.0.9 Timing Resolution

Using the reconstructed timing for each channel, We can measure the timing resolution for ECAL. First, the timing resolution for ECAL can be parametrised and expressed as a sum in quadrature (uncorrelated) of three major terms accounting for the uncertainties in the timing measurement. These three contributions are: First, the noise (N) resulting from contributions from electronic noise, coherent movement of the baseline and effects due to the fact that in addition to the main or hard proton-proton collision, other soft or less energetic collisions or events are produced known as *pile up* (PU) effect. Second, the stochastic term (S) resulting from fluctuations in the photon collection time because of finite time for $PbWO_4$ scintillation. Finally the constant term (C) whose contribution is independent on the energy deposited but rather from effects correlated with the point of shower initiation within the crystal and systematics in the extraction of the time due to different is pulse shape for each channel. The equation for the timing resolution can

thus be expressed as shown in equation (4.3)

$$\sigma^2(t) = \left(\frac{N\sigma_n}{A}\right)^2 + \left(\frac{S}{\sqrt{A}}\right)^2 + C^2 \tag{4.3}$$

A is the measured amplitude corresponding to the energy deposited and σ_n is the intrinsic noise for individual sample with a value of $\approx$ 42 MeV and 140 MeV in the barrel and endcap respectively and $N = 33$ ns measured from Monte carlo simulation studies. Contribution from the stochastic term, (S) is considered small, with value of $S < 7.9$ ns·$MeV^{1/2}$.

To measure the timing resolution, a simple experiment was performed in which electron beams with energies between 15 GeV(GeV = Giga electron volts = 10^6 eV, 1 eV= 1.602×10^{-19} joules (J) in energy units) and 250 GeV was directed unto each crystal in a supermodule. The timing resolution measurement is obtained by extracting from the measured distribution of the difference in timing between two crystals sharing energy from the same electromagnetic shower. The advantage of this approach is that, the contribution from poor synchronisation is less as this synchronisation effects do not affect the spread but rather the average time. However, it is not blind to crystal-to-crystal synchronisation effects. Other methods used to study timing resolution is considering the timing difference between two a few group of crystals usually 5×5 crystals called basic clusters, between a complete electromagnetic shower or electron or photon.

Using equation (4.3) and neglecting the stochastic term because its contributions are negligible, the timing resolution can be expressed as:

$$\sigma^2(t_1 - t_2) = \left(\frac{N\sigma_n}{A_{eff}}\right)^2 + 2\bar{C}^2 \tag{4.4}$$

where $A_{eff} = A_1 A_2 / \sqrt{A_1^2 + A_2^2}$, $t_{1,2}$ and $A_{1,2}$ correspond to the times and amplitude measured in the two crystals and $\bar{C}$ is their residual contribution. Measuring the timing resolution is performed by using the standard deviation of the Gaussian fit of the distribution from each slice in A_{eff}/σ_n distribution. The $\sigma(t_1 - t_2)$ against A_{eff}/σ_n of the extracted standard deviation of each slice is plotted the resulting distribution fitted to extract the noise and constant term. The results are shown in figure (??) with the noise factor $N = (35.1 \pm 0.2)$ ns and $\bar{C} = (20 \pm 4)$ ns.
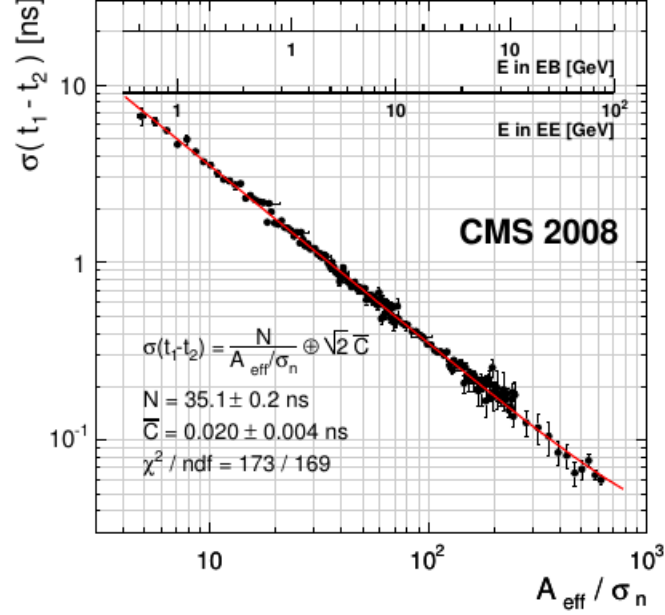
Figure 4.4: Deviation of the timing difference as a function of A_{eff}/σ_n between two crystals sharing an energy in the same electromagnetic shower obtained during electron testbeam measurements. The single crystal energy scales for barrel (EB) and endcap (EE) is overlaid. The fitted results give $N = (35.1 \pm 0.2)$ ns and $\bar{C} = (20 \pm 4)$ ns.

A timing resolution better than 100 ps for energy values A_{eff}/σ_n greater than 400 ADC counts is obtained. This demonstrates that for a perfectly calibrated ECAL crystals and energy deposits of $E > 20$ GeV in the barrel, we can obtain a resolution better than 100 ps.

4.0.10 Timing Calibration Procedure

The timing calibration is performed such that particles travelling along a straight path with speed close to the speed of light or $\beta \approx 1$ produced from proton-proton collisions happening at the CMS luminous region or IP will arrive at the surface of an ECAL crystal with an average time of 0 ns. This means that if a particle arrives at a crystal with its arrival time significantly and positively large, then it is either because this particle is travelling with a very small velocity (slowly moving particles or $\beta << 1$) or it was produced with a decay path that significantly deviates from the obvious

straight path connecting the arrived at crystal to the IP or it is a particle from the decay of a temporarily stopped particle in the detector. The presence of the "T_{MAX} Phase", the difference in pulse shape between each crystal, variation in time of flight by a few nanosecond (ns) and the different intrinsic delays among channels allow for timing calibration at two separate levels. At the level of the front end electronics (FE) consisting of 5×5 crystals, one is capable of performing an initial internal timing synchronization by adjusting in steps of 1.04 ns among these crystals. Determining these values of adjustments to be made is referred to as *Hardware Synchronization.*

Offline Timing Calibration

The purpose of the offline calibration is to provide additive timing adjustments values for each channel measured from reconstructed data to account for global phase shift in timing caused by shifts in CMS clock relative to the LHC bunch crossings and de-synchronizations induced by hardware interventions occurring usually during detector repairs. The global shifts due to drifting in CMS clock relative to LHC bunch crossings can be about 1 ns while that caused by hardware intervention can be about 3 ns. The calibration constants obtained for each crystal or channel are the negative values of the average time measured from the reconstructed hits of each crystals. These crystals are kept in XML files which are then loaded into the online configuration database holding the hardware settings. The calibration procedure is as follows:first identify the existence of a timing shift occurrence using either the CMS or ECAL detector running electronic (e-Log) book or the CMS or ECAL data acquisition monitoring (DQM) results. Second, if there is a timing shift, use reconstructed crystals hits or rechits from very recently produced data to measure the calibration constants for each channel. Finally deploy the validated calibration constants in an XML format file into the online configuration database for reprocessing of CMS full datasets to be used for physics analysis. This process is repeated over and over until the entire LHC proton-proton collision period each year. At the end of each calibration process, the set of calibration constants developed for the hardware settings within a period of time is referred to as having an *interval of validity or IOVs.* The amount of data used in measuring the timing constants is defined by the amount of event statistics available and covers a particular CMS events run range. During the entire LHC run period of 2011, a total of 17 IOVs

were developed while during 2012 LHC run, a total of 44 IOVs were produced. The raw dataset used in producing the calibration constants are mostly ECAL crystals hits from Level-1 triggered events with loosely triggered electromagnetic objects including a photons, electrons and hadrons with larger electromagnetic proportions called *ElectronHad* or *PhotonHad*. These event rechits must pass the following selection criteria: The event time (an average over its rechits) must be smaller than 5 ns. Event rechits must belong to a basic cluster (cluster of about 5×5 crystals) with transverse energy of atleast 2 GeV. The signal amplitude must not be lower than 26(47) or 100 (in year 2012) ADC counts for rechits in EB(EE) corresponding to an energy of about 1(3) GeV respectively. The reconstructed rechit time must be within 5(7) ns window in EB(EE) respectively and to reduce the presence of anomalous crystal hits, the ratio of the sum of energies of the north, south, east and west neighbouring crystals excluding a crystal with the highest energy to that of the energy of the highest energy crystal must be greater than 5% or equivalently $1 - E_4/E_1 < 0.95$. This variable is known as the *swiss-cross* variable and it is very useful for rejecting events with anomalous crystal energy deposits. The selected rechits are used to make a timing distribution for each channel and if each channel has at least 10 rechits, the average time measured represents the timing calibration constants or inter-calibration coefficient to be applied for correction while the spread or variance represents the spread in this measurement. For channels with less than 10 valid rechits, the average time of all the other channels is assigned to them as their inter-calibration coefficient. validation of these constants is obtained by applying the negative value of these constants to the same or a different set of events and varying that the measured average over rechits per channel is 0 ns to within the accuracy of the calibration method and event migration in the event sample. The event migration effects are of the order of 10 ps. The figures in figure 4.5 shows a two dimensional distribution of the channel mean time for each crystal for all the 61,200 crystals in the EB and 1468 crystals in EE. Its shows the mean timing distribution prior to calibration and after the measured calibration constants have been applied. The full IOVs produced for the entire LHC runs 2011 and 2012 can be found here [?].

Mean Time EB [ns]

Entries 61560

Mean Time EEM [ns]

Entries 10000

Mean Time EEP [ns]

Entries 10000

Mean Time EB [ns]

Entries 61577
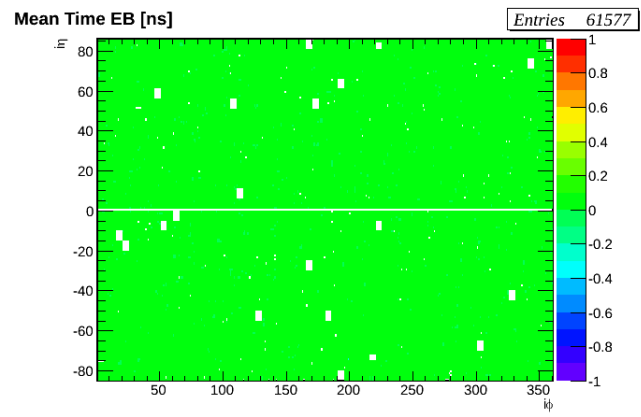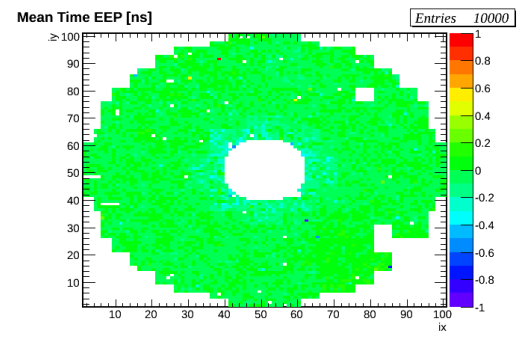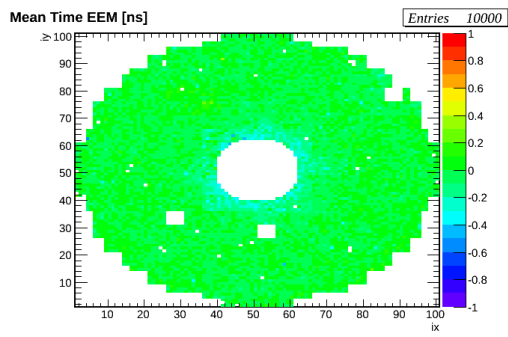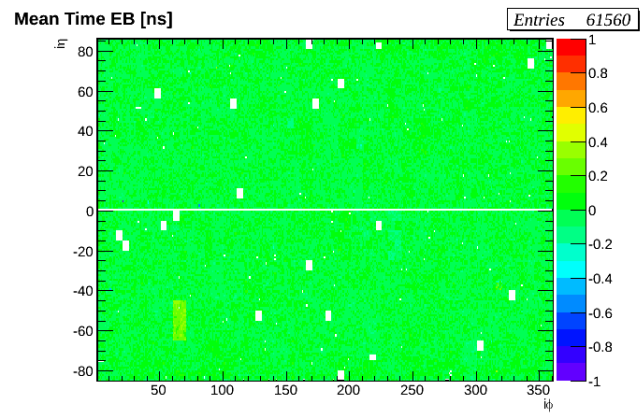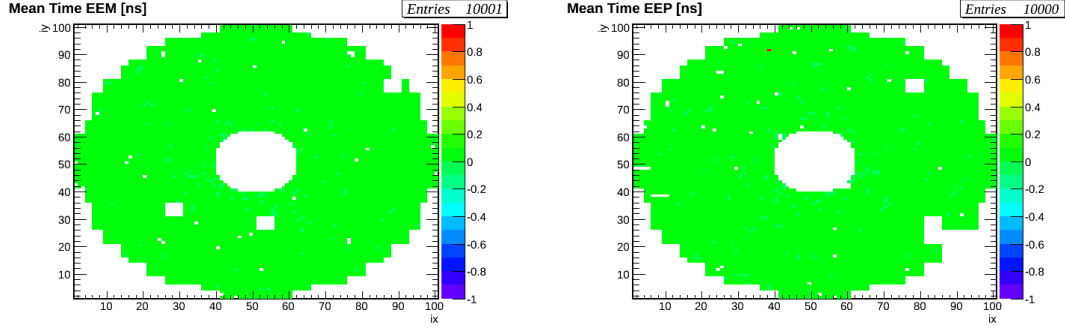
Figure 4.5: Top: Timing calibration maps showing the distribution of average time for each channel/PbWO$_4$ crystal in EB (top) and EE (below: EE−(left), EE+(right)) before calibration.
Bottom: Timing calibration maps showing the distribution of average time for each channel/PbWO$_4$ crystal in EB (top) and EE (below: EE−(left), EE+(right)) after calibration. After calibration most crystals have an average time of zero.

Hardware Timing Calibration

Often, it happens that during a regular technical stop or machine development period, the hardware experts maintaining the ECAL front end electronics introduce a timing offset due to hardware intervention. These timing offsets are not easily adjusted at the event reconstruction level, offline, using software from proton-proton collisions data. These hardware settings for readout electronics with timing offsets if not properly aligned can contribute to the worsening of the timing resolution. The traditional method of correcting for this hardware timing latency during CMS data taking when the LHC is colliding protons at stable beams has been to collect enough data with the unadjusted hardware settings with timing offset during stable proton beams, stop the entire CMS data taking process while LHC proton collisions are ongoing and use the collected data to extract the hardware timing offset and finally use these extracted timing offsets to adjust the hardware settings for future collisions when CMS detector data taking has resumed. These offsets are extracted from Data Quality Monitoring (DQM) and data certification hardware readout electronics performance histograms. However, although these procedure is quite effective, it is not very efficient as stopping the ECAL section of the CMS detector in order to adjust the settings of the hardware readout electronics requires a huge loss in data taking by the entire CMS detector. Since the

goal of the CMS data taking department is to minimised the lost of data as much as possible thus reducing the difference between LHC delivered luminosity and CMS recorded luminosity, an efficient approach is needed. We have developed such an approach to investigate and adjust the hardware settings in case of a timing offset at the readout electronics after each period of technical stop or machine development. Rather than using collision data, we use the laser data whose initial primary objective is to adjust for crystal energy resolution due to loss of crystals transparency through radiation. We use laser data to measure hardware timing offset and use these timing offsets provide new hardware settings prior to proton-proton collision. These adjustment is performed at the level of ECAL online readout electronics condition data base. The full procedure for this process can be found at [?]. The ECAL laser system comprise of two lasers, a 440 nm wavelength (close to peak emission for $PbWO_4$ crystals) laser for monitoring crystal transparency lose and a 796 nm wavelength laser for monitoring readout electronics chain from APDs to ADCs. Both lasers have jitter of less than 4 ns for every 24 hours run. To account for this jittering effect, the timing from the laser is averaged over 600 event pulses. The time for each crystal from laser is expected to be the same as the time from data and is represented as T_{MAX}^{APD}. The ECAL laser system is also equipped with a fast acquisition card called MATACQ. The time for each channel recorded using the Matacq is also averaged over 600 event pulse denoted as T_{Matacq}. The difference in $T_{MAX}^{APD} - T_{Matacq}$ between these two times averaged over a clock and control unit (CCU) comprising of 25 crystals gives the time for each CCU denoted as $t_{CCU} = \langle T_{MAX}^{APD} - T_{Matacq} \rangle$ average over 25 crystals. Thus to calculate the timing shift of 25 crystals belonging to the same front end electronics (FE), we monitor for any changes to the this average before (t_{CCU}^B) and after (t_{CCU}^A) hardware intervention. This difference $\Delta t_{CCU} = t_{CCU}^A - t_{CCU}^B$ after corrections due to global shift in the average timing $(\langle t_{CCU}^A - t_{CCU}^B \rangle)$ for all the CCUs in an entire supermodule (SM) or front end detector (FED) or single readout unit from the data acquisition point of view. These global timing shift of all the crystals in a given FED is due to the laser light distribution inhomogeneity or evolution of the laser pulse due to different optical fibre supply of laser light to each CCU. Each FED or SM is made of 1,700 $PbWO_4$ crystals. The plots in figure 4.6 show our current observation of monitoring for any shift in timing within each CCU using laser. It shows the distribution of the CCU timing difference Δt_{CCU} with its

root mean squared (RMS) value for each CCU before and after machine intervention. Considering the subtraction of the global shift per FED also reduces the possibility of false timing shift showing up by a given CCU.
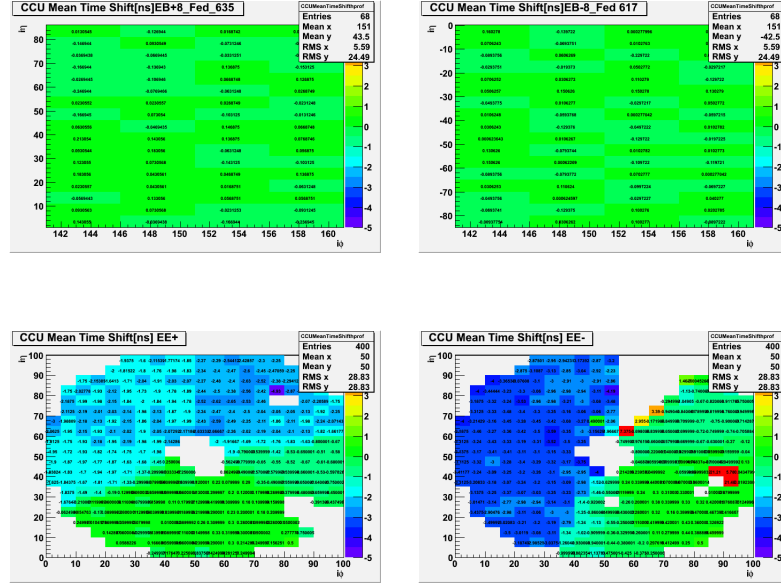
Figure 4.6: Top: Crystal mean time distribution for crystals in readout electronics EB±8. Crystal time is obtained from Laser data. Bottom: Distribution of CCU timing shift in readout electronics due to hardware intervention for EB (top) and EE (bottom). The adjustment for global timing shift per FED due to difference in light source for each CCU can be seen to reduce the possibility of CCU showing false timing shift. The figures show the distributions of the Δt_{CCU} with corresponding RMS values before (left) and after (right) the global shift has been subtracted.

Using the average subtraction method with the laser data, we can measure each CCU timing shift to within 0.2 (0.5) ns in EB (EE) precision. This tool and procedure allow for adjusting the hardware timing settings at CMS data taking site in Point5 at Cessy, France. However some validation studies for the reliance and efficiency of this tool is yet to be performed.

Timing Bias

The Ratio algorithm described in previous sections for extracting the amplitude and time of an event from the ten digitized samples for a given crystal or channel is assumed

to performed smoothly for all energies of a given initial particle impinging on the crystal. However, during collision, this is not the case, especially during gain transition points of the MGPA. An inherent bias in the timing measurement is introduced for incoming electromagnetic particles with energy above the gain transition point. The energy in GeV units deposited by an incoming particle on each crystal, i is given by the signal amplitude A_i, in ADC counts and other correction and conversion factors using the equation:

$$E_i = G \cdot S_i(t) \cdot C_i \cdot A_i \tag{4.5}$$

where G is an ADC-to-GeV factor with value equal to 0.039 (0.063) in EB (EE). C_i is the inter-calibration coefficients accounting for different channel response and $S_i(t)$ is correction term (usually from laser data) accounting for radiation-induced channel response and changes as a function of time. The Gain 1 transition point occurs at 4096 ADC counts corresponding to 159.744 GeV in EB and 258.048 GeV in EE. The subsequent Gain 6 and 12 transitions are at energy values of TeV range. The bias in timing introduced as a result of these gain transitions cannot be corrected at hardware or calibrated away rather we developed a method of applying these timing bias corrections at the standard CMS Software (CMSSW) reconstruction package. Using reconstructed hits with same selection as offline timing calibration, selected hits are also required to be path of a basic cluster (usually 9×9 or 25×25 matrix of crystals) to ensure that they are electromagnetic objects produced from proton-proton collisions. These hits must have amplitude with channel noise consideration above 10 ADC counts, in order to reject hits with very large timing biased and must be overcome the swiss-cross variable selection threshold. A distribution of the hit time against its amplitude is plotted and then sliced in bins of amplitude. Each bin with having at least 7 hits is fitted using a Gaussian function constrained within ± 7 ns. The average or mean and standard deviation or RMS of this distribution is extracted and plotted again its corresponding amplitude or energy bin content to give a distribution of mean against amplitude and standard deviation or resolution against amplitude. This procedure is performed for different Modules or pseudo-rapidity (η) ranges starting from $\eta = 0$ which is Module1 in barrel to $\eta = 3$ for high-eta in endcap. Figure 4.7 shows these distribution for different CMSSW release (CMSSW44X) where the these bias corrections have not been

applied to the software release (CMSSW5XY) in reconstruction where they have been applied. The dataset used for this reconstruction is the *DoubleElectron* and *Photon* dataset processed using CMSSW44X release during LHC RUN 1 and later reprocessed using CMSSW53X with the bias corrections we developed applied. All CMSSW releases beyond CMSSW5XY now have these bias corrections applied.
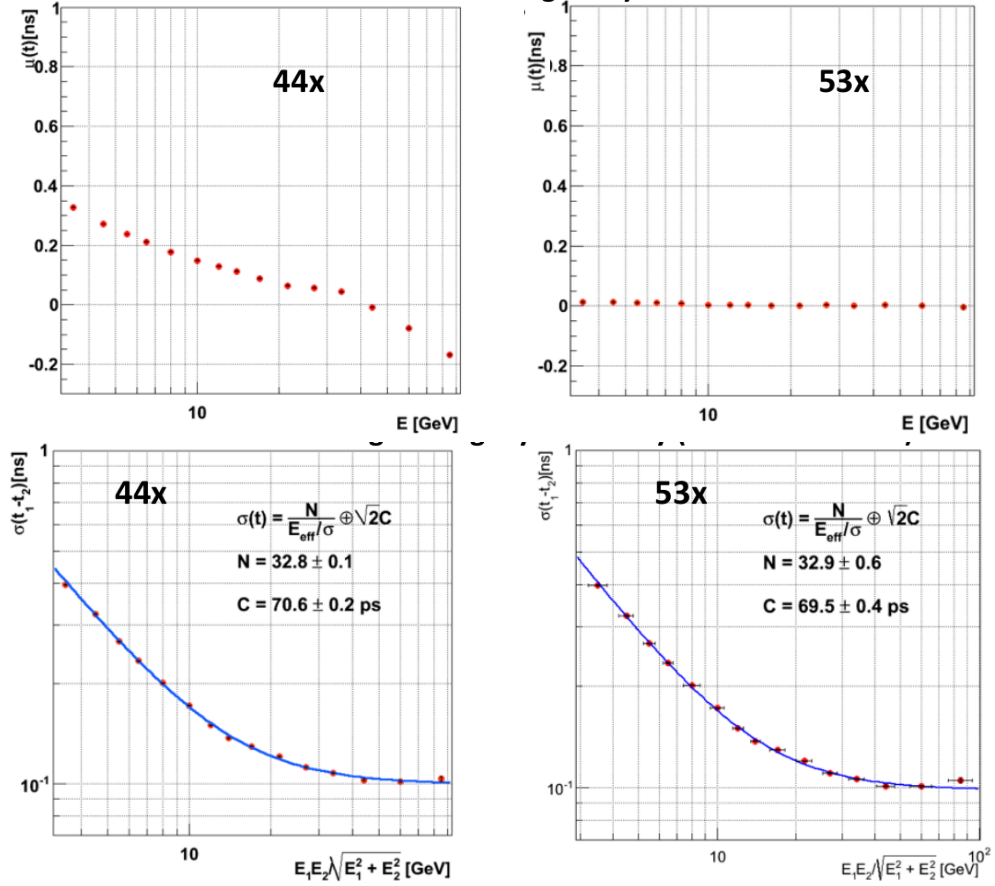
Figure 4.7: Top: Distribution of mean time as a function of crystal energy for EB prior (left) and after (right) timing bias corrections depending on amplitude developed have been applied.
Bottom: Distribution of timing resolution as a function of crystal energy for EB prior (left) and after (right) timing bias corrections depending on amplitude developed have been applied.

Figure 4.8 show the distribution of the mean and standard deviation for different modules in barrel and sections in endcap. The timing resolution do not show any dependence on pseudo-rapidity (η), however minor dependence on event run number and different electronics or trigger towers have been observed. These small effects are yet to be understood and provides a challenge in realising using proton-proton collision data, ECAL timing resolution as initially observed during tests using electron beams.
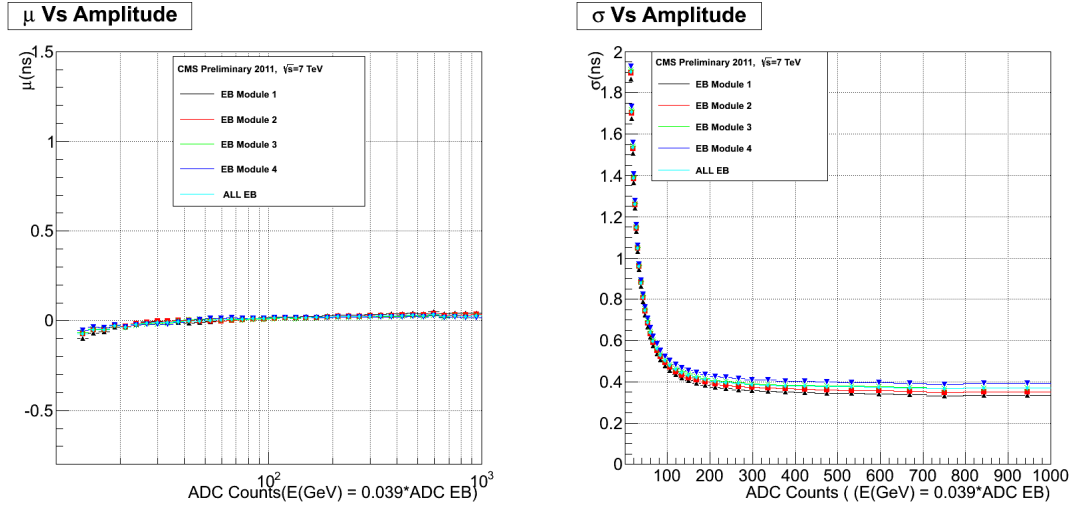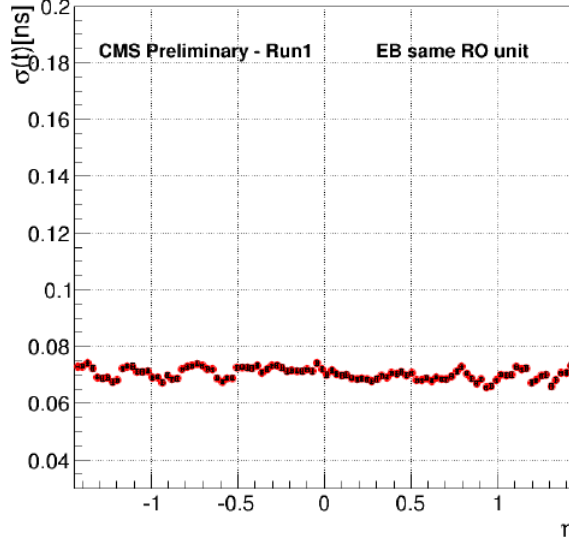
Figure 4.8: Top: Distribution of mean time as a function of amplitude (left) and Resolution as a function of amplitude (right) for different pseudo-rapidity regions in the barrel.
Bottom: All modules in EB combined timing resolution as a function against η crystals in the same readout electronics in barrel (EB).

4.0.11 Electromagnetic Calorimeter Timing Performance

Timing calibration has been performed to properly align the timing of an incoming event which might be effected due to variations of event time in different runs, poor inter-calibrations especially between different front end electronics, biased on timing due to timing dependence on energy, reduction in $PbWO_4$ crystal transparency due to radiation, hardware intervention during machine repairs and other yet understood causes. To ensure that the calibration procedure has improved on the timing alignment, we study the timing performance of the ECAL crystals and validate this studies using events electrons produced from the decay of a Z boson i.e $Z \rightarrow e^- e^+$. The decay of a Z boson is a very well understood signal and with effects due to poor event reconstruction or detector effects very well understood and measured.

The main idea is to use these two electrons or any two reconstructed candidate "objects" which in principle should have the same ECAL crystal arrival time and then use their

measured time difference as a measure of timing resolution of the PbWO$_4$ crystals in ECAL. These two reconstructed candidate objects can be:

1. Two crystals within the same electron super cluster.

2. Neighbouring crystals with a particular supercluster and sharing the same supercluster energy. This has the advantage of minimizing shower propagation effects.

3. Two crystals each from the different electron superclusters.

4. Or the two well reconstructed and energy corrected superclusters from the Z decay.

In using reconstructed electron, we considered following additional contributions to the electron time:

1. The bending of the electron path due to the presence of the 3.8 T magnetic field of the CMS detector.

2. Displaced collisions because "partons" (subparticles) in the protons of the proton-proton (p-p) bunches did not collide at exactly the collision point or nominal interaction point (IP).

3. The collision developed over the full duration of the overlap of the proton bunches. This is known as the spread in collision timing and account for about 183 ps in worsening of timing resolution.

The Time-Of-Flight (TOF) of the electron from the I produced in a nominal collision is assumed to be zero on average in the time calibration algorithm since the electrons or photons travel with speed very close to on even the speed of light. However, there are slight variations due to the difference in originated point or vertex position of these electrons or photons. In the case of electrons, the true vertex position of the electron can be reconstructed and the small TOF variations corrected for, but in the case of photons, since photons do not leave in track signals in the tracker detector, it is a bit challenging to account for these variations in TOF due to no knowing the true primary vertex where the photon originated from. There are active studies ongoing to be able to use ECAL timing to reconstruct the true primary vertex of a photon using the information of its arrival time in the ECAL, cluster position and energy. This kind

of studies is motivated by the Higgs decay into two photon process i.e $H \to \gamma\gamma$, as we continue towards understanding the properties of the recently observed scalar boson particle decay into to photon process.

Thus photons are used for timing calibration of the $PbWO_4$ crystals while electrons or electron candidates in general are used for studying the timing performance. Figure 4.10, shows the timing resolution obtained by extracting the timing of the seed crystal (crystal with highest energy) within the electron suspercluster (a) and the time difference of both electrons with the corrections due to time of flight applied (b). Without contribution from the fact that proton collisions develops across the entire beam luminous region of nearly 5.5 cm referred to as proton collision time (corresponding to about $\sigma(t_{colision}) = \sigma(t_Z) = 183 \ ps$) removed in quadrature gives 232 ps in EB and 384 ps in EE timing measurements from Z events. This is pretty good resolution for detecting late electromagnetic particles if produced during a new kind of particle interaction non in the SM. The electrons used are required to isolated to differentiate them from hadrons by using simple cluster shape selection requirements. Each electron candidate making the Z must have a transverse energy bigger than 10 GeV. Both electrons must also have their invariant mass bounded from below (above) by a 60(150) GeV cut i.e 60 $GeV < m_{inv}(e_1, e_2) < 150 \ GeV$ to make a good Z boson candidate.
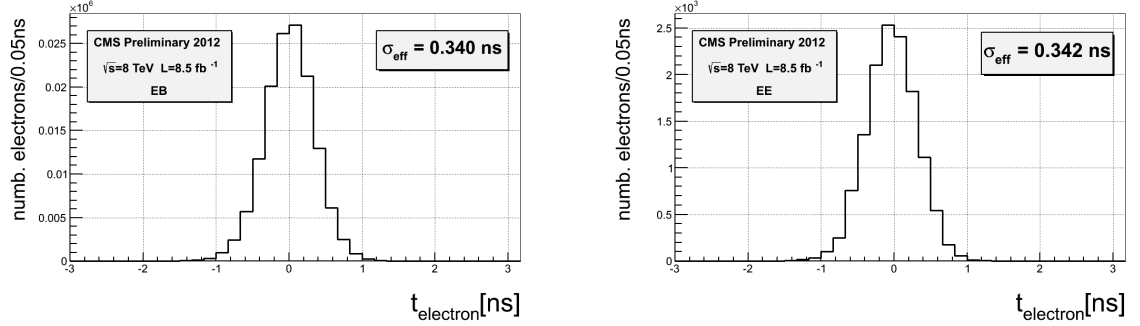
Figure 4.9: Ecal absolute time of a single reconstructed electron in Z $\to$ e$^-$e$^+$ decay. The electron time is the seed (crystal with highest energy deposit)time of the electron.(a) in in EB and (b) in EE
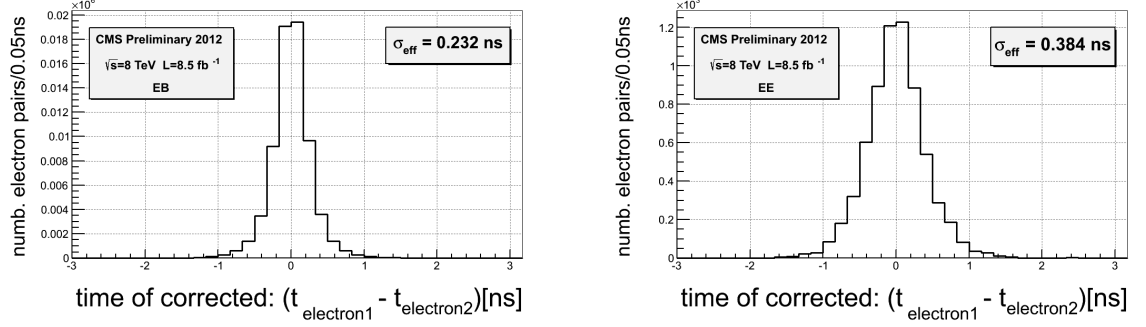
Figure 4.10: Ecal time difference between the two reconstructed electrons in Z → e⁻e⁺ decay. The electron time is the seed (crystal with highest energy deposit) time with additional correction due to the time of flight of the electron.(a) in in EB and (b) in EE

To compare the timing resolution obtain during test beam studies to that obtained recently at the end of LHC Run 1, a similar figure is made as shown in figure 4.11 produced from the Z → e⁻e⁺ decay events with the timing difference between the two electrons plotted as a function of the effective amplitude normalised to the noise in the ECAL Barrel for 2011 and 2012 data. The noise term in consistent with results obtained during test beam while the constant term is bout 150 ps much larger than that obtained from test beam studies. Its has been shown that effects such as poor inter-calibration between two different front end electrons, run dependence and radiation might be the reason for the large constant term. There is active research ongoing towards archiving the test beam results, however the current value is good enough to use the ECAL timing as a variable to search for long-lived particles.
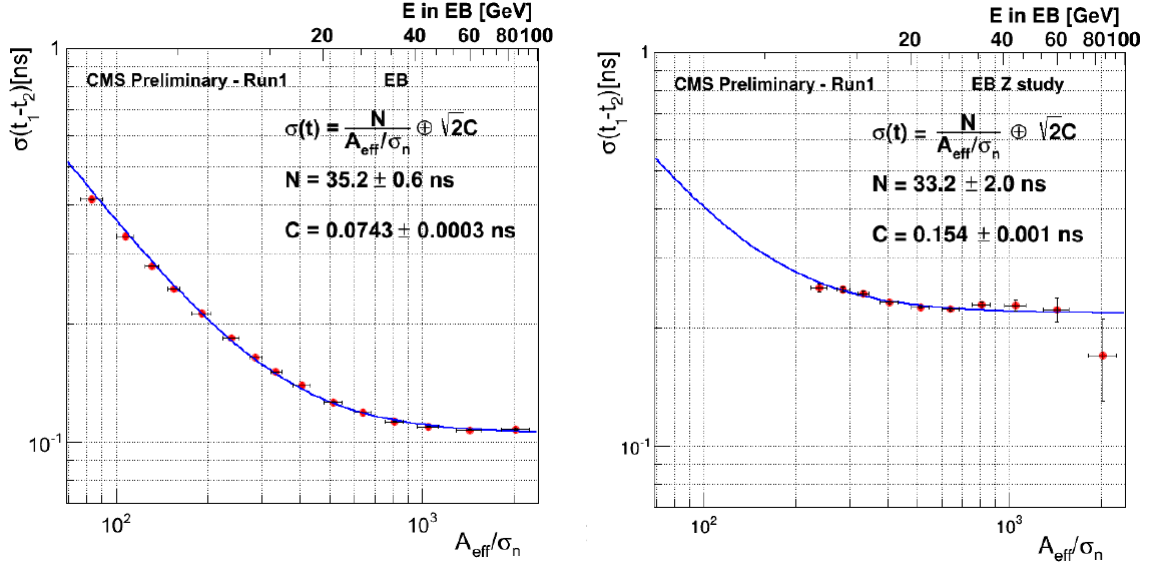
Figure 4.11: Resolution of time difference between two most energetic crystals in the same readout unit of an ECAL cluster as a function of effective amplitude- The Neighbouring crystal method(left), Resolution of time difference between the two reconstructed electrons in Z $\rightarrow$ e$^-$e$^+$ decay as a function of effective amplitude($A_{eff} = A_1 A_2/\sqrt{A_1^2 + A_2^2}$), for both electrons in EB; The Z method (right). The noise term N is the same as test beam for bother methods while the constant term $\bar{C}$ is better for the Neighbouring crystal method (70 ps) than for the Z method (150 ps) indicating the effect due to different intercalibrations between two different readout of front end electronics.

Table 4.1 shows Ecal timing resolution for 2011 and 2012 dataset.

	ECAL Timing Resolution	
	2011	
	$\sigma_{eff}(t_{seed})$[ps] Absolute time	$\sigma_{eff}(t_{e1} - t_{e2})/\sqrt{2}$[ps] Single Precision
EB	376	190
EE	356	282
	2012	
	$\sigma_{eff}(t_{seed})$[ps] Absolute time	$\sigma_{eff}(t_{e1} - t_{e2})/\sqrt{2}$[ps] Single Precision
EB	340	164
EE	342	272

Table 4.1: Table Comparing Timing Resolution performance of 2011 with 2012

Chapter 5

Physics Objects Reconstruction and Identification in CMS

5.1 Physics Objects Reconstruction

Reconstruction is the operation of constructing physics quantities from raw data collected in the experiment. It is a software process whose objective is data reduction to higher-level objects use for data analysis. An event observed by the CMS detector is reconstructed using information from the different sub-detectors. This information represents the raw data from the DAQ which is in a format called digitised hits or *digis*. A local reconstruction is performed with the output from these reconstruction units called *RecHits*. The local reconstruction algorithm search for pixel or strips with a signal exceeding a threshold and use these as seeds for clusters. RecHits are typically position measurements (from times or clusters of strips or pixels) in tracking type detectors (Muon and Tracker systems) and energy deposits or hits from Calorimetry systems. For example in the Muon Cathode Strip Chambers (CSCs),local reconstruction provides position and time of arrival of muon hit from the distribution of charge induced on the cathode strips. For the case of the Electromagnetic Calorimeter (ECAL) and Hadronic Calorimeter (HCAL), local reconstruction identifies, the position, time of arrival and energy of localised electromagnetic and hadronic energy depositions respectively. The typical software package for local reconstruction is label as RecoLocalTracker as in the case of tracks indicating only local modules of the sub-detector have been used. Global

reconstruction takes these rechits as input to produced higher-level objects like charge particle tracks. This is where information from different modules in the same sub-detectors are combined. Clustering, tracking and fitting algorithms are used at this stage. For example, in ECAL and HCAL, global reconstruction provides a Calorimetric Tower (CaloTower) links matching clusters in ECAL and HCAL to produced a projective tower in the calorimetric system. These towers have a definite position in (η, ϕ) plane and are used as basis for Jet reconstruction as described later in the sub-sections. In the Tracker, global reconstruction uses tracker hits and track segments and use the seeds for Kalman fitter which builds trajectories with a χ^2 cut applied to reject hits unlikely to be associated with tracks. The typical software packaged is label RecoTracker again as in the case of full charge particle tracks. The final reconstruction combined reconstructed objects from individual sub-detectors to produced higher-level reconstructed objects suitable for high-level triggering or physics analysis. Further selection requirements may be further applied until the final physics objects such as electron, photon or jet belonging to the event is fully reconstructed.

5.1.1 Supercluster Reconstruction

The basis of all object reconstruction is the supercluster or basic cluster. Electromagnetic showers of photons and electrons are deposited in several crystals. Usually about 94% (97%) of the incident energy is deposited in a 3×3 (5×5) matrix crystals in the (η, ϕ) plane. The presence of 3.8 T magnetic field, material in front of the calorimeter causes bremssrahlung electrons and converted photons to deposit their energy in calorimeter in the form of small clusters spread in ϕ. This energy is recovered using clustering algorithms where by starting with a seed crystal containing the maximum of energy, superclusters (clusters of cluster) are build within a narrow window in η by is summing the crystal energy along the ϕ which is the direction of energy spread due to the magnetic field. Figure 5.1 shows a simple picture how these super clusters are build.
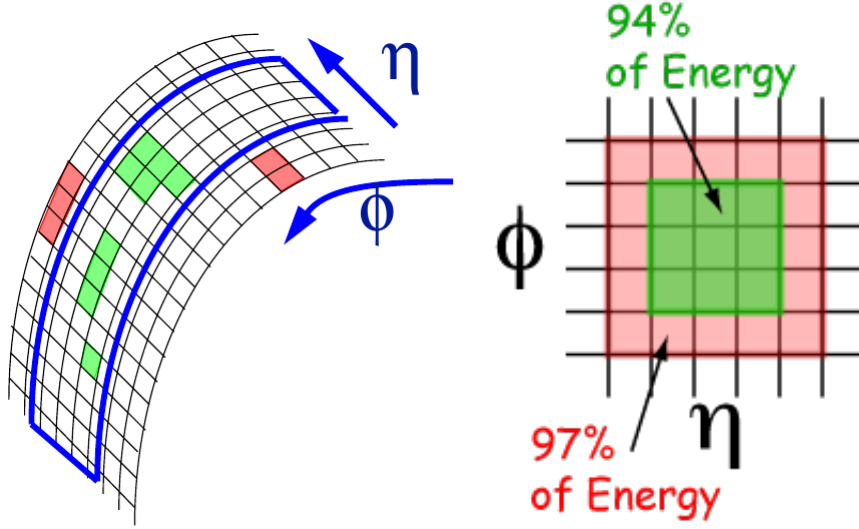
Figure 5.1: Superclustering algorithm in ECAL for both hybrid (EB) and island (EE) clustering algorithms.

There are two major clustering algorithms used:

- **Hybrid Superclusters:** This algorithm is used to make super-clusters in the barrel (EB). It takes advantage of the $\eta - \phi$ geometry of barrel crystals by taking a fixed 3 or 5 crystals in η and dynamically search and sum separate crystals energy along ϕ. The Hybrid algorithm takes advantage of our knowledge of the lateral shower shape along the η direction. The supercluster is made of basic clusters. The figure 5.2 shows an example of how the hybrid clustering algorithm performs clustering.
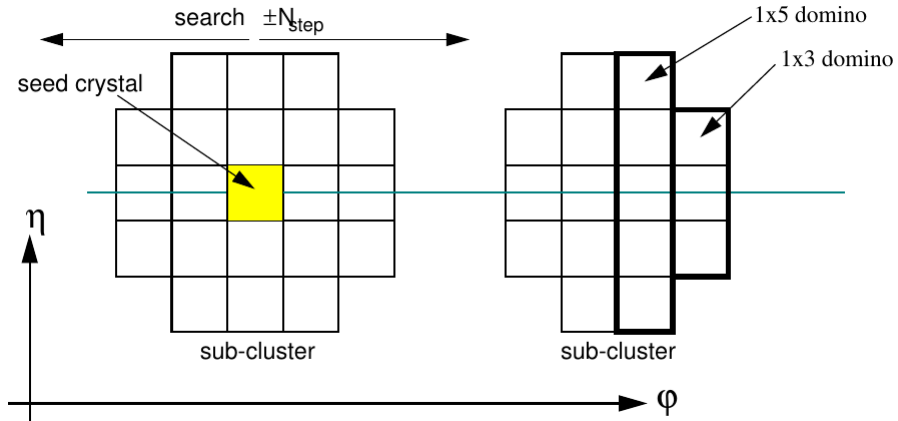
Figure 5.2: Superclustering in ECAL for hybrid clustering algorithm in barrel.

- **Island Basic cluster or Superclusters:** After Local reconstruction leading to the production of *EcalRecHits*, the island algorithm is applied in both barrel and endcap (EE)to produce superclusters. This algorithm begins by finding the seed crystal with a local energy maximum above a certain threshold. from the seed position, adjacent crystals are examined starting fist along ϕ and then in η adding crystal energy to cluster until a crystal belonging to another cluster or crystal that has no readout is reached. For each crystal to be added to the cluster, the crystal must contain a rechit with positive energy, the crystal has not been assigned to another cluster and the previous crystal added in the same direction has higher energy. These non-overlapping clusters are then made into superclusters. A search is performed for the most energetic cluster and then collect all the other narrow window clusters in η and wide window in ϕ. The figure in 5.3 provides a pictorial view of how the island algorithm works.
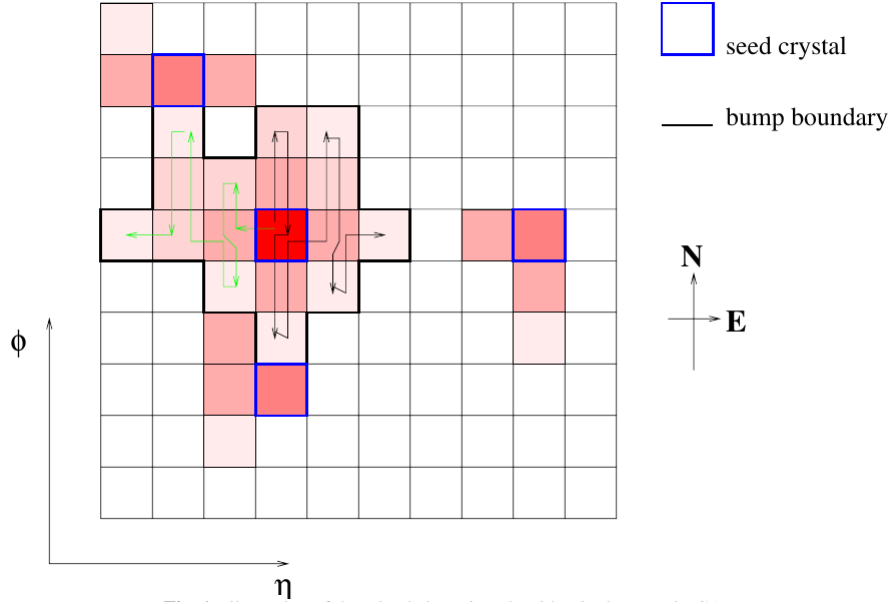
Figure 5.3: Superclustering in ECAL for Island clustering algorithm in barrel.

5.1.2 Vertex and Track Reconstruction

The reconstruction of track candidates of a charge objects such as an electron begins by selecting an initial parameter which a pair or triplet of hits constraint by the interaction region or a given beam spot in the pixel detector. This if followed by the search of other pairs of hits in pairs of tracker layers as well as hit pairs in the strips or strips an pixels to allow for reconstruction of vertices beyond the pixel volume. To prevent the combination factor and reduce fake rates when using the Combinatorial Track Finder (CTF), hits are selected in a small restricted region in ϕ compatible with a super-cluster in the ECAL. This seeding strategy is known is *tracker-driven*. Another powerful approach is to start with the ECAL super-cluster and match the seed super-cluster hits back towards hit in the tracker particular the pixel. It is term *ECAL-driven* seeding and this super-cluster-driven pixel seed finding presents advantage for comparable reconstruction efficiency and increasing the purity by reducing the presence of fake tracks in the sample of candidate tracks. This is particularly useful for electron reconstruction and is used by the Higher Level Trigger (HLT) for tagging primary electron-like objects.

In selecting the seed cluster, the cluster which initiates the bremsstrahlung recovery procedure, this seed is required to have a minimum Transverse Energy (E_T) of 1 GeV is $E_T > 1$ GeV. This requirement allows the reconstruction of electron super-cluster for with low Transverse Momentum (p_T). In a study using back-to-back e^+e^- events, a supercluster reconstruction efficiency of of about 93% is achieved for electron $p_T^e = 10$ GeV/c when $E_T^{seed} > 1$ GeV. Using this seed cluster, the hits in the pixel layer are predicted by the propagation of an energy weighted mean position of the super-cluster backward through the magnetic field under the charge hypothesis(positive or negatively charged particle) towards the pixel detectors. A first compatible hit is looked for in the inner most (barrel) of the pixel detector within a loose $\Delta\phi$ window adapted to the uncertainty of ϕ measurement of the super-cluster (ϕ_{SC}) and loose Δz interval adapted to the spread of the interaction vertices. In case no hit is found in the innermost pixel layer, the first hit is looked for in the netx-to-innermost layer. Once a compatible hit is found, a new estimate of the z_0 on the z coordinate of the primary track vertex is calculated by combining the pixel hit found and the information from the calorimeters in the RZ plane. Using this predicted trajectory, we propagate once more to look for the second pixel hit in the next pixel layer(s).

Starting from this seed (pair hits), a trajectory is created. This trajectory creating begins be first searching for the next silicon layer hits, then extrapolation is performed using a model based on the non-gausssian nature of energy losses by Bethe and Heitler, then Gaussian Sum Filter (GSF) algorithm is used to perform a fit on the track. This procedure is repeated untill the last trackers layers unless no hit if found on the subsequent layers. If many hits a found on a compatible layer, many candidate tracks are build in parallel and using the χ^2 from the GSF fit, the best two GSF track candidates with the smallest χ^2 is selected and kept. A minimum of five hits is required to create a track. The difference between electrons and photons at this stage is that photons because they are neutral have no pixel hits and as a result have no reconstructed tracks. Thus, from the ECAL driven track reconstruction, super-clusters with no pixel matched seeds fall into the photon candidate sample collection. However, 50% of the time photons due to the tracker material will convert into e^+e^- conversion pairs. These are known as *converted photons*. These converted photons are usually low p_T photons and don't always travel to the ECAL but those that do and if happen to arrive late can be candidates for clear signal of physics beyond the SM. Because electrons have a GSF tracks , they are normally referred to as GSF electrons. Using the selected GSF tracks, important particle kinematic information such as the vertex pseudo-rapidity (η), the track p_T and the vertex ϕ coordinate are well measured with good resolution.

The primary interaction vertex in an event is reconstructed from a collection of tracks. A group of tracks in clusters based on the z coordinate position of their track with respect to the point of closest approach to the beamline. The track clusters, as previously mentioned are fitted with and adaptive vertex fitter and the tracks are assigned weights between 0 and 1 based on their closeness in proximity to the common vertex. This ensures a dependence on the primary vertex resolution to the number of tracks used in the fitting and p_T. This primary vertex resolution dependence on the number of tracks is studied using tracks in an event with just one vertex while for p_T, the resolution is studied for a number of tracks with different average p_T of tracks in the vertex. It is important to recall that tracks can only be reconstructed up to $|\eta| < 2.5$ which defines the tracker volume, beyond which these objects are assumed to have no tracks.

5.1.3 Photon or Electron Identification

Electron and photon identification depends of the ability to reject minimum biased events, underlying events or Pile Up (PU) produced from multiple proton-proton interactions, electrons embedded in hadronic showers or Jets and anomalous events. Pre-selections are applied at the level of track seeding and clusters so as to reject tracks from underlying or low energy proton-proton collision events called Pile Up (PU). Based on kinematic and nature of electromagnetic showers in the ECAL, some variables have been developed and their performance studied for optimal identification and isolation of electrons and photons. This is in compatibility with the fact that the two electron reconstruction algorithms compliment each other in specific p_T range. The tracker seed driven algorithm is more suitable for low p_T electrons as well as better performance for electrons inside jets while ECAL seed driven algorithm which selects seeding clusters with transverse energy $E_T > 1$ GeV is optimised for isolated electrons $p_T > 10$ GeV/c up to p_T relevant for the mass of Z or W bosons.

The goal of the ECAL is to obtain the best estimate of energy deposited by an electron or photon in the ECAL, $E_{e/\gamma}$. This from the detector point of view, the energy deposit is given as:

$$E_{e/\gamma} = F_{e/\gamma} \cdot [G \cdot \sum_i S_i(t) \cdot C_i \cdot A_i] \tag{5.1}$$

where A_i is the signal amplitude in ADC counts, C_i is the inter-calibration coefficient, $S_i(t)$ is the time-dependent corrections for response variable usually obtain from laser, G is the global scale calibration allowing one to move form energy in ADC counts to GeV and $F_{e/\gamma}$ is the particle energy corrections for geometric, clustering and other effects. The sum is over all the crystals belonging to the photon or electron super-cluster. In order to measure and reconstruct the true energy of the detected particle, energy corrections depending on η such as $F_{e/\gamma}$ are applied at the level of super-cluster reconstruction to account for detector effects hence better identification of particles, in this case electrons and photons. Figure 5.4 shows energy scale and resolution obtained when these energy corrections are applied compared with when no corrections are applied. Figure 5.5, shows the scenario for applying these corrections at the level of super-cluster reconstruction which at this stage are only electromagnetic objects.
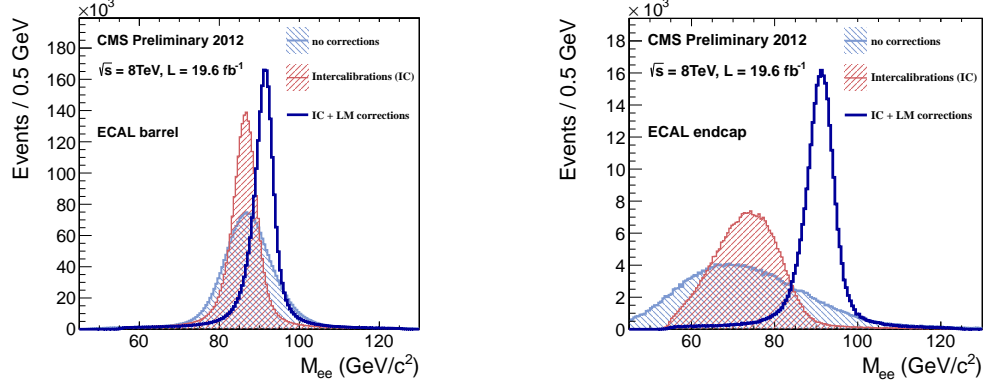
Figure 5.4: $Z \to e^+ e^-$ mass plot showing resolution and energy scale that is obtained from applying energy scale corrections to account for intrinsic spread in crystal and photo-detector response and time-dependent corrections to compensate for channel response loss for EB (right) and EE (left)
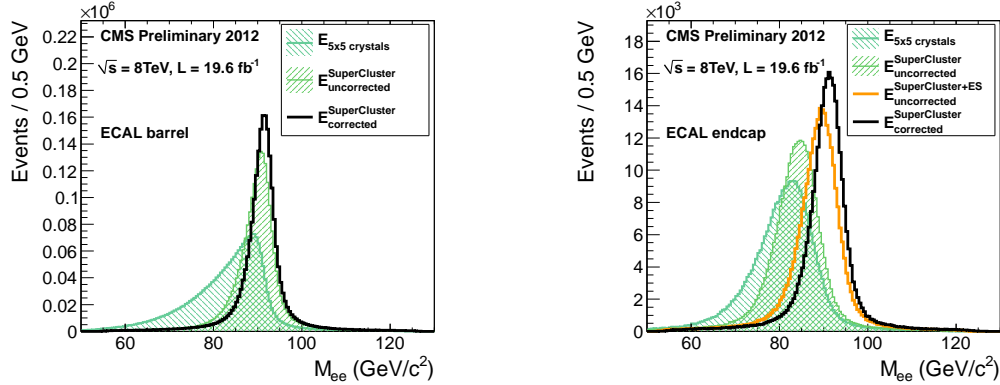
Figure 5.5: Super-clusters showing resolution and energy scale that is obtained from applying energy scale corrections for EB (right) and EE (left)

With these electron or photon candidates, further selections using variables constructed from information on the spread of the electromagnetic shower in η and ϕ, the ratio of the energy deposited in ECAL and HCAL, the track p_T and ECAL E_T to further identify photons and electrons. Pre-electron candidates based on cut elections such as minimum transverse energy, $E_T > 4$ GeV, η and ϕ geometrical matching; $\Delta Eta < 0.02$, $\Delta\phi < 0.1$ and a cut on Ratio of hadronic to electromagnetic energy cluster: $H/E < 0.2$ is enough to suit physics analysis, however, additional elections and identification criteria are added depending on the purpose of the particular analysis to fully defined an electron or photon. These identifications and isolation criteria can also be categorised

in terms of flavours as being very loose (VL), loose (L), medium (M) and tight (T). The typical variables used for electron and photon identification are defined as follows:

- Ratio of energy of HCAL behind super cluster to super cluster energy: H/E

- Energy momentum matching variables between energy of the super cluster or of the super cluster seed and electron track measured momentum at the vertex or at the calorimeter: E/p_{in}, E_{seed}/p_{in}, E_{seed}/p_{out}

- Geometrical matching between the electron track parameters at the vertex extrapolated to the super cluster and the measured super cluster position: $\Delta\eta_{in}$, $\Delta\phi_{in}$.

- Calorimeter shower shape variables: the width of the ECAL cluster along the η direction computed for all the crystals in the 5×5 block of crystals centered on the highest energy crystal of the seed cluster ,$\sigma_{i\eta,i\eta}$ and the ratios of the energy sums over 3×3 and 5×5 matrices centered on the highest energy crystal of the seed cluster: $R_9 = E_{3\times3}/E_{5\times5}$ or $R_9 = \sum E_9 / \sum E_{Supercluster}$. This R_9 variable makes a good separation between unconverted photons (energy not spread in tracker) and converted photons (energy spread by B-field before reaching ECAL).

- Bremsstrahlung fraction: (track momentum at vertex - track momentum at ECAL)/ track momentum at vertex.

- 1/E(Super cluster) - 1/p(track at vertex)

Due to the very high photon conversion rate s as a result of the tracker material in front of the ECAL cuts like:

- Calorimeter shower shape:R_9

- Impact parameter: $d0$, minimum separation of the electron track computed with respect to the reconstruction vertex.

- Missing Hits: Number of cross layers without a compatible hits in the back-propagation of the track to the beam-line.

Isolation variables in addition to the identification variables are used to improve on the performance of identification. Below are the following isolation variables as defined and used by the CMS:

Electron Photon Isolation

- Tracker Isolation: sum of p_T of tracks with $p_T > 0.7\ GeV/c$ and maximum distance to the vertex of 0.2 cm in a cone of 0.3 with an inner veto cone of 0.04.

- ECAL Isolation: sum of energy of ECAL RecHits with a Jurassic footprint removal (Jurassic width of about 1.5 crystals) in a cone of 0.4 with veto cone of 3 crystals. A RecHit noise cut of 0.08 GeV in energy (E) in barrel and 0.1 GeV in transverse energy (E_T) in the endcap is applied.

- HCAL Isolation: sum of HCAL Calorimeter Towers in a 0.4 cone with a 0.15 veto cone.

In general the major difference between an electron and a photon as identified by the CMS detector is that electrons which have no pixel strip hits are automatically classified as photon candidates and further isolation and shower shape variables are used to arrive at the ultimate photon as required by a given analysis. Table **??** shows the Simple Cut-based selection criteria variables and cut thresholds used to identify electrons and photons in the CMS detector.

Particle Flow Algorithm

An alternative criteria for reconstructing and identifying physics objects in the CMS detector which is now widely acceptable is the *particle flow* (PF) algorithm.

The particle flow algorithm takes into consideration information from every sub-detectors like the tracker, ECAL, HCAL and muon section before identifying a particular physics objects. The goal of this algorithm is to reconstruct higher level physics objects like Jets, missing transverse energy (MET), and the identification of tau (τ) and b-jets by making use of the content of these objects in terms of more fundamental objects like electrons and photons or super clusters and tracks. The algorithm constitutes of steps like calorimeter clustering, tracking and extrapolation to calorimeters, muon identification, electron pre-identification, linking of topological elements and finally particle

identification and reconstruction. The result is a list of reconstructed particles consisting of photon, charge hadron, neutral hadron, muon and electron. From this list high level objects such as jets, MET and taus can be reconstructed. In the case of electrons reconstructed using the PF algorithm, tracks, electron energy seeds, 4-momentum, super cluster energy calibration, Bremsstrahlung tracks are used as base objects to reconstruct the entire electron. The PF is very useful in MET reconstruction where information about all the particles making up a single event is necessary to calculate MET.

Simple Cut Based Electron Photon Identification		
ID Variable	**Electron**	**Photon**
H/E	0.05(EB), 0.10(EE)	0.05
$|\Delta\eta_{in}|$	0.005(EB), 0.007(EE)	0.015(EB)
$|\Delta\phi_{in}|$	0.09(EB), 0.09(EE)	N/A
$\sigma_{i\eta i\eta}$	0.01(EB), 0.03(EE)	0.011(EB), 0.03(EE)
Pixel Veto	No	Yes
$|d0|(vertex)$	0.02(EB), 0.02(EE)	Veto
$|dZ|(vertex)$	0.1(EB), 0.1(EE)	0.02 (cm)(Veto)
$|1/E - 1/p|$	0.05(EB), 0.05(EE)	N/A
PF isolation / p_T (cone dR=0.3)	0.15(EB),0.10(EE)	N/A
ECAL Isolation	same	$4.2 + 0.006 * E_T^\gamma + 0.183 * \rho$(EB)
HCAL Isolation	same	$2.2 + 0.0025 * E_T^\gamma + 0.062 * \rho$
TRACK Isolation	same	$2.0 + 0.001 * E_T^\gamma + 0.0167 * \rho$
Rho corrected PF photon isolation	N/A	$1.3 + 0.005 * p_T^\gamma$(EB)

Table 5.1: Simple Cut-Based criteria for High energy electron and photon identification in CMS

5.1.4 Muon Reconstruction

The are three different types of muons reconstructed using the muon system detection all making up one huge collection of muons. They are Stand-alone, Global and Tracker Muons. Reconstructed hit positions within each DT and CSC are matched to form "segments" which are then collected and matched to generate seeds used as starting point for actual track fit of DT, CSC, and RPC hits. The resulting product of the fit in the muon spectrometer is a "stand-alone muon". "Global muons are formed when these stand-alone muon tracks and matched to tracker tracks in the tracker while "tracker muons" are muon objects reconstructed starting form silicon tracker tracks compatible with segments in the muon chambers. Using muon isolation variables defined using the calorimeter and tracker tracks, a collection of muon objects is identified in CMS. Thus is summary, stand-alone muons contain only hit position information from the muon chambers, global muons contain this information in addition to tracker information while Tracker muons are muons reconstructed starting with information from the inner tracker which is matched with calorimeter and muon chamber information. Using the beam spot as a constraint ensures that muons produced from proton-proton collision are distinguished from those produce from cosmic rays known as *cosmic muons* or from beam splash/gas 150 m upstream proton beam dump known as *beam Halos*. The 2 T **B**-field with a multi-stage flux-return yoke shields the muon detectors from hadrons ensuring that the measured particles can be identified as minimum ionizing muons. The barrel muon detector consists of 4 stations forming concentric cylinders $|\eta| < 1.2$ around the beam line while the endcaps system consists of 468 cathode strip chambers (CSC) arranged in groups as 72 ME1/1, 72 ME1/2, 72 ME1/3, 36 ME2/1, 72 ME2/2, 36 ME3/1, 72 ME3/2and 36 ME4/1 and the 72 ME4/2. A muon in pseudo-rapidity range of $1.2 < |\eta| < 2.4$ crosses a total of 4 CSCs. Muons in the encaps-barrel overlap region; $0.9 < |\eta| < 1.2$ are detected by both the barrel drift tubes (DT) and endcaps CSCs while in bother barrel and endcaps RPSc are used for triggering. RPCs are capable of tagging the time of an ionizing event in a much shorter time than the 25 ns between 2 consecutive LHC Bunch Crossings as a result triggering based on RPC can be used to unambiguously identify the relevant Bunch Crossing to which a muon track is associated even in the presence of high rate and background expected in the LHC.

Cosmic and Halo Muons

Muons produced centrally or from proton-proton collision are reconstructed a bit different from other muons. Halo muons originating from machine-induced particles travelling along the beam line and cosmic muons originating from cosmic rays require global information in order to distinguish them from centrally produced muons. Both cosmic and halo muons are considered to be background muons in most physics analysis. The stand-alone muon reconstruction software suited from reconstructed muons from proton-proton collision assumes these muons to be moving radially outward in seen in figure 3.11 while cosmic muons originate from the outside of the CMS detector and can traverse only a small part of a detector depending on its energy and direction. Figure 5.6 show an illustration of different trajectories for the different types of muons.
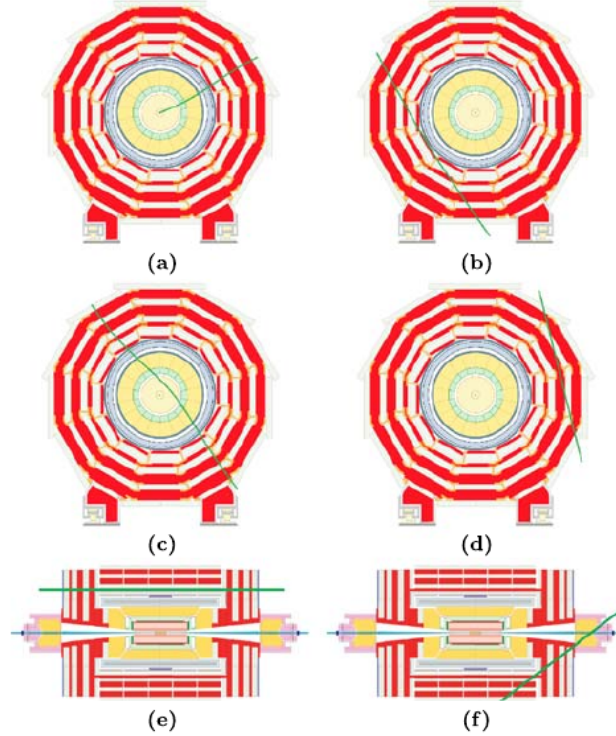
Figure 5.6: Illustration of the differences between proton-proton collision muons, cosmic and halo muons. (a) Muons from collision propagating from the center and moving outwards in a well defined pattern, (b) Cosmic muons penetrating the detector and leaving signals in opposite hemispheres of the muon system, (c) Cosmic muons leaving signals in the tracker and opposite hemispheres, (d) cosmic muons entering and leaving the detector without passing through the muon detector layers, (e) beam halo muons penetrating the detector and leaving signals in the endcaps and (f) Cosmic muons entering the detector through the endcap and leaving through the barrel and which can happen in a vice-versa manner.

A new stand-alone and global muon reconstruction software with the assumption that muons originate from outside the CMS detector and according to the properties of cosmic and halo muons has been optimised to reconstruct and identify both cosmic and halo muons which are used studies involving calibration and aligning the muon detectors.

5.1.5   Jet Reconstruction

Jets are experimental signatures of quarks and gluons produced in high energetic processes such as hard partons scattering in proton-proton collisions or gluon radiation processes. CMS reconstructs four types of jets which each combine individual contributions from sub-detectors to form inputs to a jet clustering algorithm. The four types of jets include Calorimeter jets, Jet-Plus-Track (JPT) jets, Particle-Flow (PF) jets and track jets. The clustering algorithm is the Anti-k_T clustering algorithm with a size parameter of $R = 0.5$. Calorimeter jets are reconstructed using energy deposits in the combine ECAL and HCAL calorimeter cells called calorimeter towers. A calorimeter tower is a single or group of HCAL cells with their geometrically corresponding ECAL crystals. In order to suppress both noise and and contributions from event pile-up (additional proton collisions within the same bunch crossing), thresholds are applied to both the individual cells when building the calorimeter towers as well as a transverse energy (E_T) cut on the calorimeter tower energy. Typical $E_T^{towers} > 0.3 - 0.7$ GeV is often used. Of particular importance to our analysis is the Particle Flow jets (PFJ). PFJ are reconstructed using the PF algorithm. The PF algorithm uses as input a list of reconstructed particles which include charge hadrons from tracks in central tracker, photons and neutral hadrons reconstructed from energy clusters in the HCAL and ECAL,

neutral particles as clusters separated from extrapolated position of tracks in calorimeters and electrons from tracks matched to clusters in the calorimeters. The PF algorithm exploits the high granularity in ECAL to precisely measure charge hadrons and photons inside jets, which makes up a larger portion of the jet energy. The quality of the jet is determined by variables making up the "Jet ID". For example, a high quality jet is required to have an electromagnetic energy fraction (EMF), $EMF > 0.01$, within the ECAL fiducial region $|\eta| < 2.6$; the number of calorimeter cells containing more than 90% of jet energy must be $n_{jet}^{90} > 1$; and the fraction of jet energy in the hottest Hybrid Photo Detector (HPD) unit of HCAL readout within a jet must be $f_{HPD} > 0.98$; the charge hadron fraction $CHF > 0.0$ if within $|\eta| < 2.4$, neutral hadron fraction $NHF < 1.0$, charge electromagnetic fraction $CEF < 1.0$, and neutral electromagnetic fraction $NEF < 1.0$. These requirements are used to remove fake jets arising from spurious energy deposition in a sub-detectors. Because the measured jet energy is usually different (usually unwanted energy) from the true corresponding particle jet energy due to miss-reconstruction, non-linear response of the calorimeters, electronic noise and additional energy contributions from PU, jet energy corrections during jet energy calibration (JEC) are applied to correct for this energy miss-match between the reconstructed measured jet energy and the true energy of the jet particle. This JEC to determine the jet absolute response is a source of systematic uncertainties in a given physics analysis.

5.1.6 Missing Transverse Energy Reconstruction

A typical collider detector can only be nearly hermetic despite its nearly 4π solid angle coverage as there is always room for passage of the colliding beams. As a result the use of the total energy balance constraint is not very useful since low p_T energetic interaction products moving in the forward direction can always escape detection. Thus, although these forward moving particles can carry significant longitudinal momentum (momentum along the direction of the beams), their transverse momentum (momentum transverse to the direction of the beam), p_T is always smaller than their total momentum. In the case of the CMS detector which has pseudo-rapidity $|\eta| < 5.0$, therefore only particles with $|\eta| > 5.0$ can escape detection, as we can easily find that the p_T of any given particle in CMS detector given as $p_\mathrm{T} = E/\cosh\eta < E/\cos(5) < 0.013 \times E$.

Thus even if the particle carried the whole 7 TeV energy of a single proton beam, its $p_T < 100$ GeV/c. Partons inside a protons which collide to produced moving particles typically have only a a fraction of the energy of the colliding proton. Each fraction is determine by parton distribution function (PDF). PDF are rapidly falling functions, thus a typical momentum for forward moving particles in hard collisions on interests for physics goals of an experiment is significantly less than the full beam energy. As a result, the transverse momentum carried away by particles beyond the acceptance of a calorimeter is very small, thus the detector allows for a precise test of 2-D momentum conservation of the plane perpendicular to the direction of the beams. In the case of the CMS detector, this plane in the $x - y$ plane. Thus the measurement in the calorimeter of a significant imbalance in the transverse momentum will indicate the production of a weakly interacting particle in the collision. Among SM particles, such an imbalance would indicate the presence of e neutrino or a muon which deposits a very small amount of energy in the calorimeters. However, the momentum of the muon can very precisely be measured using information from the tracker and muon chambers, and the calorimeter based missing transverse momentum can be measured and corrected for the muon's presence. Thus only the neutrino would truly escape detection, and its presence would be inferred from the remaining imbalance in the total transverse momentum as measured in the calorimeter and muon detectors. Other extensions of the SM, also predict the existence of other weakly interacting stable and quasi-stable particles, thus if an excess of events with s significant amount of transverse momentum imbalance is observed after accounting for all the SM processes, it would constitute a strong evidence for new physics beyond the SM. In the case of the minimal GMSB, the gravitino ($\tilde{G}$ would be the new physical particle. Thus the total transverse momentum imbalance or *missing transverse momentum* is an important variable to use in the search of new physics particles. On the other hand, poorly reconstructed objects, detector malfunctions, electronic noise and miss-measured transverse momentum can all lead to missing transverse energy thus mimicking the signal for new physics. Thus careful studies of the performance of the missing transverse energy variable in identifying neutrinos in the SM with high efficiency and accuracy is needed in order to depend on the use of it. The missing transverse momentum represented as the Missing transverse energy or MET (E_T^{miss}) which is itself a scalar quantity defining the magnitude of the missing

transverse momentum which has both direction ($\phi_{E_{\mathrm{T}}^{\mathrm{miss}}}$) and magnitude $E_{\mathrm{T}}^{\mathrm{miss}}$. The missing transverse energy is defined as the magnitude of the negative transverse vector sum over all energy deposits in uncorrected, projective Calorimeter Towers produced in a given event:

$$E_{\mathrm{T}}^{\mathrm{miss}} = |-\sum_n (E_n \sin\theta_n \cos\theta_n \hat{\mathbf{i}} + E_n \sin\theta_n \sin\theta_n \hat{\mathbf{j}})| = |\not{E}_{\mathrm{T}}^x \hat{\mathbf{i}} + \not{E}_{\mathrm{T}}^y \hat{\mathbf{j}}| \qquad (5.2)$$

Where n is the sum over all calorimeter input objects including energy deposits in towers, reconstructed hits or generator -level particle energies. The $E_{\mathrm{T}}^{\mathrm{miss}}$ values in physics processes of interest include processes with small $E_{\mathrm{T}}^{\mathrm{miss}}$ such as the decay of W bosons and top in the SM to large $E_{\mathrm{T}}^{\mathrm{miss}}$ as in the decay of SUSY particles. Thus in order to use small $E_{\mathrm{T}}^{\mathrm{miss}}$ for searches, SM processes like QCD, JEC and low energy resolution must be well understood while to use large $E_{\mathrm{T}}^{\mathrm{miss}}$ for searches, machine induced background processes and poor event reconstruction which processes with sources of large $E_{\mathrm{T}}^{\mathrm{miss}}$ must equally be well understood.

5.2 Anomalous Signals

Neutrons and charged hadrons such as protons may by pass the $PbWO_4$ without scintillating and striking and thus directly ionizing the silicon of the APDs to produce anomalous signals. These kind of events produced large isolated energy deposits thus are referred to as "punch through" events or "spikes". Because of the lack of scintillation, they appear much earlier (negative) in Ecal time and often populate the earlier time of the rechit time distribution. Their energy deposit ranges from a few GeV to ECAL saturation energy of ≈ 1.7 TeV. Since they do not electromagnetically shower in $PbWO_4$, their electromagnetic energy shower shape is very isolated, meaning only one or two crystals may make up their energy cluster. Spikes may also have positive time and thus appear late or delayed in their arrival at ECAL which is seen in the tails of the rechit time distribution. Their late arrival time is due to the slow propagation of neutrons through the CMS detector. A lot of test beam, collision data and simulation study has been performed to study and analyse the characteristics and rejection of spikes as seen in here [36]. As a result, most of the results presented in this thesis are

taken directly from [36] or redone for 2012 dataset which this analysis is based upon. It has been observed through studies using minimum bias data set(highly populated with neutrons and charged hadrons) at different center of mass energy, that the number of spikes increases with the proton collision rate as well as the charged tracks per event i.e there is a strong linear correlation between spike rate and the center of mass energy of pp collision. The reason for this is because more neutrons and charged hadrons with enough energy are produced which "punch through" the APD and produce hikes in the rechit energy profile as read from the APDs. It is understandable that spike production is most common in the barrel compared to the endcap. Thus with increases rate of proton collision and $\sqrt{S} = 8$ TeV, it is imperative to have robust variables which can identify and reject spikes in the barrel in this analysis. The above studies show that variables defined using timing and EM energy deposits are reliable. Other variables using the timing pulse shape and EM shower profile can be use in addition to identify and rejects spikes with efficiency of 90 to 95%.

Rejection of spikes is done at online(CMS Level-1 trigger level) as well as offline and analysis level.

At online, the strip Fine-Grained Veto Bit(sFGVB) is set to 0 or 1 use to flagging an object as either a spike or a good event respectively. A detail of this can be found in [37]. For example if the sFGVB is set to 0 and the trigger tower(5×5 crystals) transverse energy is below 12 GeV, the energy deposition is considered spike-liked and the corresponding tower will not contribute to CMS triggering of that event. The sFGVB was implemented in 2011 data taking process and was measured to reject over 95% of spikes with transverse energy greater than 8 GeV (12 GeV) in 2011(2012). The figure **Figure of sFGVB** shows the difference between an good EM-cluster and a spike-like cluster at sFGVB level.

At Offline, variables making using of the single(at times double) channel(crystal) energy deposit and early arrival time of spikes are defined. In figure **Figure of Swiss X and Rechit Time**, we show the difference between spikes and normal events energy clusters explaining the variables used to identify spikes in the offline. The topological variable constructed as $1 - \frac{E_4}{E_1}$ also known as "Swiss-cross" where E_1 is the energy deposit of the central(highest energy) crystals and E_4 is the sum of the energy of the neighbouring crystals in an $\eta - \phi$ plane is used for identifying isolated spikes. The figure**Figure of**

Spike energy topology and Distribution of SwissX shows the construction of the swiss-cross variable as well its distribution in data and simulation events. The peak at 1.0 in data of the distribution is due to the presence of spikes. A cut in Swiss-cross > 0.95 rejects more than 99% of isolated spikes with transverse energy greater than 10 GeV with very little impact on the efficiency of selecting electromagnetic EM showers. Other topological energy deposit variables such as $1 - \frac{E_2}{E_6}$ and $1 - \frac{E_2}{E_9}$ where E_2 is the sum of the energy of two crystals sharing the energy deposited and $E_6(E_9)$ is the sum of the neighbouring 6(pairs-of)(9) crystals in the $\eta - \phi$ plane. The $1 - \frac{E_2}{E_6}$ variable is used for the identification of isolated spikes whose energy deposit spread in two adjacent crystals while the $1 - \frac{E_2}{E_9}$ is used to identify non-isolated spikes or spikes which are found embedded in a normal Ecal supercluster.

The figure **Put figure of di-spike and non-Isolated spike construction and distribution** A cut on $1 - \frac{E_2}{E_6}$ ($1 - \frac{E_2}{E_9}$) greater than 0.95 (0.98 for tight) gives an efficiency close to 95% for events with transverse energy greater than 10 GeV for rejecting spikes with very little effect on normal EM shower reconstruction.

Another very important variable used for rejecting spikes with greater efficiency is rechit ECAL timing. Spikes and EM energy deposits show very distinct signal pulse shapes. Since spikes do not in the $PbWO_4$, when the pulse shape is fitted to extract the timing of a signal, the spikes appear "early" due to faster rise time of the spike pulse. The figure **Fig of spike pulse shape and rechit time distribution for data and simulation** shows the comparison between the pulse shape for a spike candidate pulse and and true $PbWO_4$ scintillated event. The adjacent plots shows the distribution of the rechit time for simulation(where there are no anomalous signals) and collision data where anomalous signals have a significant contribution to out-of-time signals.A cut on timing of ± 3 ns gives greater than 90% efficiency for rejecting spikes however, in this thesis, we do not employ this timing cut as we are actually searching for delayed objects whose timing can be beyond the ± 3 ns window.

However, it is worth nothing that, these anomalous signals if not rejected will lead to a biasing in the reconstruction of other physics variables such as missing transverse energy(E_T^{miss}) as well as being miss-identified as a possible signal for delayed photons. Infact the spike rate per bunch crossing as observed in [37] was approximately 1×10^{-3} in collisions bunch crossings while in non-collision bunch crossing is of the order of 2×10^{-6}

in non-collision bunch crossings. This spike rate from non-collision rate is obtained from cosmic muon data recorded during June-August 2009 while the spike rate for collision is obtained from Minimum biased(Soft proton-proton) collision events data. Thus, in this thesis, we have restricted ourselves to using only the energy topological variables discussed in previous paragraphs to identify and reject anomalous signals.

5.3   Using Timing for Event Cleaning

Energy RecHits and clusters used in the reconstruction of higher level objects are required in addition to cluster cleaning conditions, to pass certain selection criteria using transverse energy and ECAL timing. For the case of photon, electron, PF jets and $E_{\mathrm{T}}^{\mathrm{miss}}$ reconstruction, the basic and super-clusters are required to be seeded by seed crystals whose time is within approximately 3 ns in the barrel and 7 ns in the endcaps. These are called *in-time* RecHits. These RecHits are the standard RecHits used in the reconstruction for most physics objects used in physics where timing is not an important variable. The choice for using timing, is because, timing combined with other topological variables is an excellent variable to identifying and rejecting readout electronic crystals with large noise, poorly reconstructed RecHits, RecHits from anomalous signals, RecHits from machine induced events and cosmic muons as well as improved timing calibration. However, for physics analysis like our case of searching for long-lived particles, this cleaning procedure is not useful. As rejecting RecHits with time more than 3 ns also known as *Out-Of-Time* RecHits will remove super clusters from potentially delayed electrons and photons which defines the signal for new physics. Thus in this analysis, we combined all classes of RecHits, and do not reject RecHits with large reconstructed time except if the time is well beyond expected time for physics objects produced in proton-proton collisions within the required Bunch Crossing time spacing of 25 ns or 50 ns. The electromagnetic objects in this analysis are reconstructed from the combined sample of time cleaned and unclean RecHits. All other RecHit cleaning is applied except that which involves RecHit timing information.

Chapter 6

Search Analysis for Long-Lived Particles

6.1 Analysis Strategy

This analysis searches for delayed isolated photons produced with large transverse momentum. From a theoretical point of view, events containing such a photon will be a clear signal for new physics as such a photon is not expected to be produced from standard model interactions. However, from an experimental point of view, using timing measurements from ECAL sub-detector, there are many different sources of isolated, hight p_T photons. A few of these sources which have been identified are high p_T isolated and delayed photons due to timing miss reconstruction and miss-identification, photons produced from cosmic and other beam related effects like beam halo muons bremsstrahlung in the ECAL, and obviously, detector effects like high p_T neutrons by-passing the crystals and hitting directly the photo-detectors like APD and VPT, mimicking the behaviour of isolated, delayed and high p_T photons. The latter kind of photons are called spikes. They are normally isolated, high p_T and their ECAL time measurement show that they arrive early as well as late but with most of them arriving late compared to photons produced at the nominal proton-proton interaction region whose average arrival time at ECAL is 0 ns. These different sources of background makes it a bit challenging to distinguish a possible signal photon from true physics and background photons which are mainly instrumental. Thus, estimating the

background contributions to possible signal sample requires using true proton-proton collision events or data rather than simulated events as is normally done in most physics analysis. Nevertheless, as it is with most hadron collider physics analysis, exploring the use of the number of jets in the event selection can most often reduce dramatically the background contamination to possible signal sample. It is not different with this analysis, as we have employed jet multiplicity both as a physics related quantity for the production of high p_T isolated and delayed photons but also as a detector variable for reducing and at times discriminating background contribution to possible signal sample. Our motivation is related to the existence of physics models beyond the SM like the minimal GMSB (mGMSB) and GGM, where the production of a high p_T isolated, delayed photon in association with a number of jets constitutes a typical new physics event which could be produced at the LHC. Thus using simulated events from mGMSB or GGM model, serves both as a guiding model for the confirmation of a new physics signature at LHC but also as an alternate hypothesis for setting upper limits based on this model in the case that no significant excess over SM prediction is observed.

A typical signal event considered in this analysis for the existence of a neutral massive long-lived particle decaying into a photon is the detection of a late photon arriving at crystals in the ECAL sub-detector of CMS associated with jets with large E_T^{miss}. However, the production and decay of this long-lived neutral particle, in our case the neutralino ($\tilde{\chi}_1^0$), is associated with the production of at least two jets and a weakly interacting gravitino ($\tilde{G}$) as an additional decay product, with a late arrival photon since this is a cascade decay process from a possibly higher mass object into the neutralino and finally to the gravitino. The presence of the gravitino ($\tilde{G}$) is inferred using the transverse momentum imbalance whose magnitude is E_T^{miss}. In the SPS8 minimal GMSB or GGM model with R-parity conservation (RPC) assumed, SUSY particles are produced in pairs and so there would be an event having at least a single photon arriving late, associated with at least 2 jets and large E_T^{miss}. This signal configuration helps in defining and selecting our signal region (SR) and a control region (CR) for estimating the contribution to this signal from standard model processes and the detector effects considered as background processes.

6.1.1 Signal and Background Modelling

The SPS8 GMSB and GGM signal event generation begins with the production of Supersymmetry Les Houches Accord (SLHA) files using the SUSY ISASUSY package written by [?] containing the ISAJET software. The SUSY events are forced to decay according to the SPS8 GMSB and GGM model using the SDECAY decay package. These SLHA files containing information about the SUSY mass spectrum and decay rates is passed through a PYTHIA 6 [?] interface into the CMS software (CMSSW), in this case CMSSW532patch7, where proton-proton collision at $\sqrt{8}$ TeV events producing SUSY particles events are generated. Their interaction with the CMS detector is simulated using the GEANT4 package [?]. Standard Model processes like multi-jets and $\gamma+$ jets processes produced from strong interactions described by quantum chromodynamics (QCD) are generated and simulated at leading order cross-sections using PYTHIA 6 and GEANT4 packages respectively. Digitisation and event reconstruction in terms of its constituent objects like jets, photons, muons and electrons, after its passage and decay in the full CMS detector is later performed still using the CMSSW software.

Signal

The SPS8 mGMSB possible new physics parameter space used for the present physics analysis involves: $\tan\beta = 15$, $sign(\mu) = 1$, and $M_m = 2. \cdot \Lambda_m$. While $c\tau$ and Λ_m is used to scan the available parameter space which maximises the sensitivity of the CMS detector to long-lived particles, in this scenario mostly neutralinos ($\tilde{\chi}_1^0$). The cascade decay of higher mass SUSY particles in the SUSY spectrum to $\tilde{\chi}_1^0$ allows for signal events with the following constituents:

- at least one energetic photon,

- large missing transverse momentum,

- a number of high transverse momentum jets.

Background

QCD multi-jets and $\gamma+$ jet(s) events produced in leading order cross-sections with high p_T range of the photons, serves as background and also for time reconstruction and

calibration and for sanity check. Events with W and Z decay and $t\bar{t}$ with large missing transverse momentum are also generated for serving as sanity check for understanding momentum measurements.

6.1.2 Datasets

The proton-proton collision dataset used in this analysis was collected during 2012 runs at the center of mass energy of $\sqrt{S} = 8$ TeV and was collected using the CMS detector totalling and integrated luminosity of 19.1 fb^{-1}.

Data

The dataset consist is mostly containing events with at least a single photon triggered and only those selected using only luminosity-sections certified as GOOD in the CMS official run file; **JASON:Cert-8TeVPromptReco-Colllisions12-JASON.txt**. Table 6.1 shows the dataset used in this analysis.

Dataset Name	Recorded Luminosity [fb^{-1}]
/Run2012B/SinglePhoton/EXODisplacedPhoton-PromptSkim-v3	5.1
/Run2012C/SinglePhoton/EXODisplacedPhoton-PromptSkim-v3	6.9
/Run2012D/SinglePhoton/EXODisplacedPhoton-PromptSkim-v3	7.1
/SingleElectron/Run2012A-22Jan2013-v1/AOD	5.2
/DoubleElectron/Run2012C-22Jan2013-v1/AOD	4.8

Table 6.1: The dataset name and corresponding integrated luminosity of the data used in the analysis

Background and Signal Monte Carlo

The Monte carlo (MC) samples are produced taking into account the Summer 2012 prescriptions carrying information on the calibration and alignment status of the CMS detector with pile up (PU) conditions at 8 TeV taking into consideration. QCD events are generated with a cross -section (σ) at leading order (LO) and normalised to the 19.1 fb^{-1} integrated luminosity. 50112 events were requested for GMSB signal MC, however, due to an observes reduced lifetime ($c\tau$) observed for these official CMS samples, private

sample were generated and simulated covering the same line 8 of the SPS8 mGMSB proposal while the absence of any MC signal samples for GGM model, meant that we had to privately generate our own samples. The SPS8 mGMSB MC samples are generated to scan $\tilde{\chi}_1^0$ lifetime $c\tau$ from 250 mm to 12000 mm for each Λ_m point with Λ_m ranging from 100 TeV to 180 TeV and seen in table 6.2 while table 6.3 show the p_{T} range for the processed QCD samples.

$c\tau$ (mm)	σ_{LO} (pb)	number of events
250	0.0145	50112
500	0.0145	50112
1000	0.0145	50112
2000	0.0145	50112
3000	0.0145	50112
4000	0.0145	46944
6000	0.0145	50112
12000	0.0145	60000

Table 6.2: The signal GMSB MC samples used in this analysis

$\hat{p}_{\mathrm{T}}$	σ_{LO} (pb)	number of events
$50 \sim 80$	3322.3	1995062
$80 \sim 120$	558.3	1992627
$120 \sim 170$	108.0	2000043
$170 \sim 300$	30.1	2000069
$300 \sim 470$	2.1	2000130
$470 \sim 800$	0.212	1975231

Table 6.3: The $\gamma+$ jets samples used in this analysis

6.2   Event Selection

The major background events to this analysis are events which are not produced from the nominal proton-proton collisions. These events can be put into four major three major categories; Halo Muons, *Spikes* and *Cosmic muons*. In addition to these events,

there are also QCD events which mimic the $\tilde{\chi}_1^0 \rightarrow \gamma + \tilde{G}$ decay as a result of photon mis-reconstruction and measurement of fake E_T^{miss}. Along with QCD events, there are also $\gamma+$ jets events as background where there is the presence of a real isolated photon and a fake E_T^{miss} is expected due to mis-reconstruction of photons from jets. However, the event topology for $\gamma+$ jets is quite different from that of GMSB events.

Another interested possible background contribution, in addition to QCD multi-jets events can come from events with electroweak (EWK) decay. This include $W \rightarrow e + \nu$ decays, $t\bar{t}$ decays, where the top (t) decays to a b quark and a W 100% of the time. The electron is mis-reconstructed as a photon and real E_T^{miss} is measured due to the presence of the neutrinos (ν). However, most of these EWK and QCD background contributions have very low jet multiplicity in their events and as a result a selection of events with at least two jets helps to reduce their background contribution to a minimal level prior to additional photon quality selections based on the isolation and electromagnetic shower profile which eventually reduces its contribution to non-existent once photon time acceptance of $t_\gamma > 3$ ns is applied.

Cosmic muons, beam halo muons and ECAL spikes can all produced photons large reconstructed time and can contribute largely to E_T^{miss} measurements since they contribute to E_T^{miss} calculation which normally measures the p_T of all the detected particles in an event assuming all of these events arise from the nominal proton-proton collision although in practice cosmic muons, beam halo muons, spikes, ECAL and HCAL noise can all contribute to the total sum of the measurable event p_T imbalance but arising from non- nominal collision sources. A pre-event selection requiring at least a good vertex, 2 or more jets ECAL spike cleaning, DT time cosmic muon cleaning and CSC tight halo-muon cleaning is shown to be very useful in reducing and estimating the contribution of these important background sources.

6.2.1 Trigger

Event selection process begins online using a higher level trigger (HLT). The HLT trigger used for this analysis during the $\sqrt{S} = 8$ TeV proton-proton collision is the *HLT-DisplacedPhoton65-CaloIdVL-IsoL-PFMET25* seeded by *HLT-L1SingleEG12* level 1

trigger. This trigger was developed primarily for the study of displaced photons. To avoid bias in event selection towards any particular model, this trigger only requires that an accepted event must have an isolated photon with a p_T threshold of 65 GeV/c and a E_T^{miss} above 25 GeV. In order to study the trigger efficiency and turn-on curve (where the event selection efficiency becomes very close to 100%), we avoid any correlation between the photon and E_T^{miss} objects selection, by using a single muon dataset (HLT-IsoMu30) to study the efficiency measurements. The results of the trigger efficiency measurements are shown in figure 6.1 against photon p_T and E_T^{miss}. These efficiency studies are made using the *HLT-Photon50-CaloIdVL-IsoL* which has no E_T^{miss} and jet multiplicity requirement as the denominator and the *HLT-DisplacedPhoton65-CaloIdVL-IsoL-PFMET25* as the numerator. A single photon dataset is used to verify these efficiency while and GMSB and $\gamma+$ jets samples is used to derive any correction factors between data and MC events.
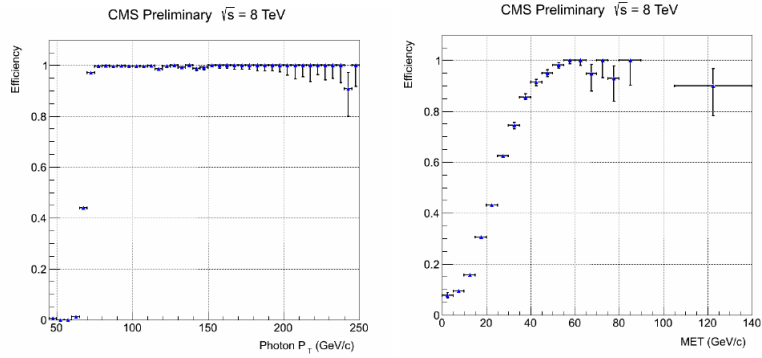
Figure 6.1: Trigger efficiency turn-on curves for photon p_T and $E_T^{miss} > 25$ GeV (left) and for E_T^{miss} with photon $pt > 80$ GeV/c (right).

6.2.2 Offline Selection

Offline event selection is directed towards selection of displaced photons with very minimal model dependency in terms of event jet multiplicity as possible. As a result, the event selection requires that the event contains at least one photon. The photon collection in contrast to other analysis, which do not employ the use of ECAL timing as a search variable, is extended to include events categorised as being "out-of-time" during the official super cluster reconstruction. These extension even though allows for the inclusion of possible background from spikes, noise, photons from beam hallo and cosmic

muons and detector malfunctions also brings with it photons which are potential signal candidates. The criteria for photon selections can be found in table 6.4.

Photon identification selection criteria	
Criteria	**Requirement**
Event leading photon must have $p_\text{T}(\gamma^1)$	> 80 GeV
Other photons in event must have $p_\text{T}(\gamma^{>1})$	> 45 GeV
$\|\eta_\gamma\|$,(Barrel Only),	< 3.0 (< 1.5)
S_{minor}	$0.12 \leq S_{Minor} \leq 0.38$
H/E	< 0.05
$\Delta R(\gamma, track)$	> 0.6
HCAL Iso	< 4.0
ECAL Iso	< 4.5
Track Iso	< 0.2
Photon Isolation cone size $\Delta R(\gamma, otherparticle)$	< 0.4
Topological Spike cuts	$1 - E_6/E_2 < 0.98$, $1 - E_4/E_1 < 0.98$

Table 6.4: The photon ID selection as used in this analysis

The presence of the gravitino ($\tilde{G}$) and jets due to the cascade decay (Feynman diagram in figure **??** of section **??**) of the $\tilde{\chi}_1^0 \rightarrow \gamma + \tilde{G}$ decay process as seen in figure 6.2 requires additional selection of jets and E_T^miss.

Figure 6.2: Schematic diagram showing $\tilde{\chi}_1^0 \rightarrow \gamma + \tilde{G}$ decay topology within the ECAL volume of the CMS detector.

The jets and E_T^miss selection criteria are based on the particle-flow algorithm. An additional $E_\text{T}^\text{miss} > 65$ GeV due to the flatness of the HLT trigger efficiency against
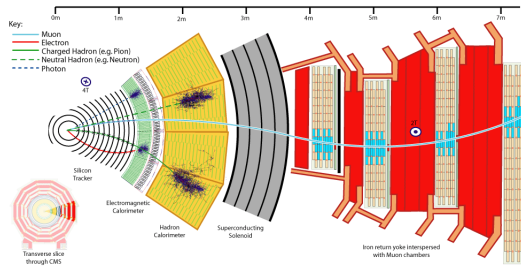
$E_{\mathrm{T}}^{\mathrm{miss}}$ (see figure 6.1) while table 6.5 summarise the jet identification criteria with threshold requirements used for jet selection in this analysis.

Jet PF identification selection criteria

Criteria	Requirement
Jet p_{T}	> 35 GeV
Number of Jet constituents	> 1
Charge EM energy fraction (CEF)	> 0.99
Neutral Hadron energy fraction (NHF)	< 0.99
Neutral EM energy fraction (NEF)	< 0.99
If $|\eta|$ of jet is > 2.4, Charge Hadron energy fraction (CHF)	> 0
If $|\eta|$ of jet is > 2.4, Charge multiplicity (NCH)	> 0
$\Delta R(\gamma, jet) = \sqrt{(\phi_\gamma - \phi_{jet})^2 + (\eta_\gamma - \eta_{jet})^2}$	> 0.3

Table 6.5: The Jet ID selection used in this analysis

6.2.3 ECAL Time

In the current analysis, ECAL time of the photon is the main observable and as a result of pile-up contamination with true photons from nominal proton-proton collisions, a reliable definition for the photon time which is robust to pile up. The two main definitions for ECAL time studied include:

- Seed Time: Time from the crystal with higher energy in object super cluster which is not a spike.

- Cluster Time: Error weighted average time of all the crystals in the seed basic cluster of the object super cluster.

The reconstruction of time as described in chapter 4 is extracted from the pulse shape through a fitting method. The χ^2 obtained from the fit determines how well the timing is reconstructed. Thus as a means of rejecting fake photons like jets faking photons as well as spikes, a $\chi^2 < 4$ cut is applied to improved on the timing resolution and hence improve on the rejection of anomalous photon. Figure 6.3 shows a comparison between the pulse shape profile of a spike and that of a normal event from data.
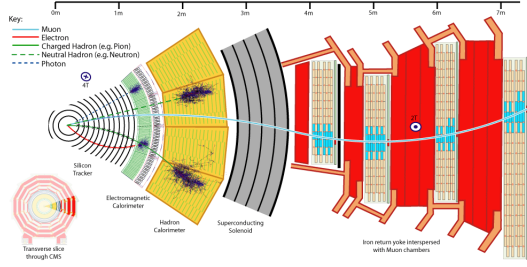
Figure 6.3: Pulse shape profile showing a spike and a real photon time from data.

.

In a study performed comparing the timing resolution obtained from cluster time to the seed time, it was observed that also the seed time method is very prone to isolated spikes, its resolution especially for large timing events is much better compared to the cluster time measurement method. Figure 6.5 shows the timing measurements of photons with $pt > 80$ GeV using either seed time or cluster time. The seed time show a timing resolution of 400 ps with a narrow time tails compared to 600 with a broad timing tail obtained from using cluster time.
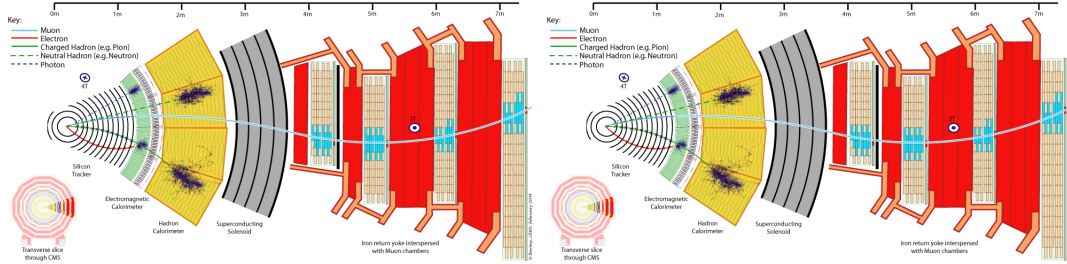
Figure 6.4: Timing distribution of photons with $p_{\mathrm{T}} > 80$ GeV showing timing measurements using seed (left) and that using cluster time (right). Resolution from seed time is much better compared to that for cluster time.

Monte Carlo simulation of ECAL timing is very challenging due to the presence of anomalous signals like spikes in data which are not available in MC samples. Thus in order to study the timing resolution between MC and data, we select events containing only one or two jets and compare this timing distribution to the difference between the Generated time (T_{GEN}) and the MC reconstructed time (T_{RECO}) within a timing window of [-2, 2] ns. The difference in peak or mean time between the data and MC $\gamma+$ jet sample is used to smear the reconstructed time of the MC samples to be as

comparable to true reconstructed time of data. A difference of about 125 ps is observed between the timing from data and that of MC, and a smearing of of the MC sample shows a close agreement between the smeared reconstructed time of the MC sample to that of data. Figure **??** shows the this comparison before and after the smearing is applied on the MC samples.
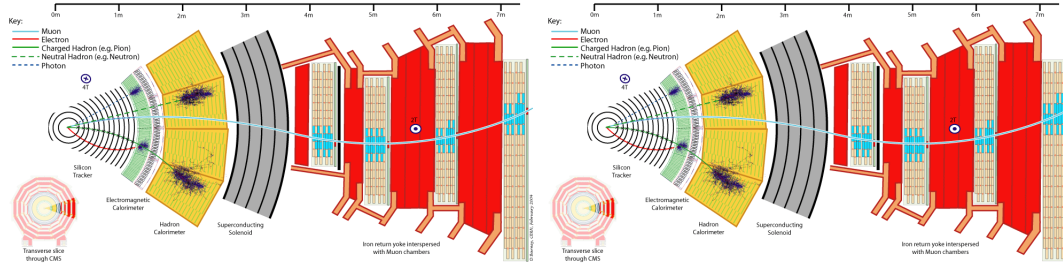
Figure 6.5: Timing distribution of photons with $p_\mathrm{T} > 80$ GeV showing timing of data and MC $\gamma+$ jets samples before (left) and after (right) smearing of MC is applied.

It is worth noting that the difference of 125 ps between T_{RECO}^{MC} and T_{RECO}^{DATA} compared to 500 ps ECAL timing resolution is not enough to influence event selection, however event distribution in the tails remains a major concern.

The ECAL timing distribution for photons with $pt > 80$ GeV in the ECAL (barrel and endcap inclusive i.e $|\eta_\gamma| < 3.0$) show timing distributions (see figure 6.6)
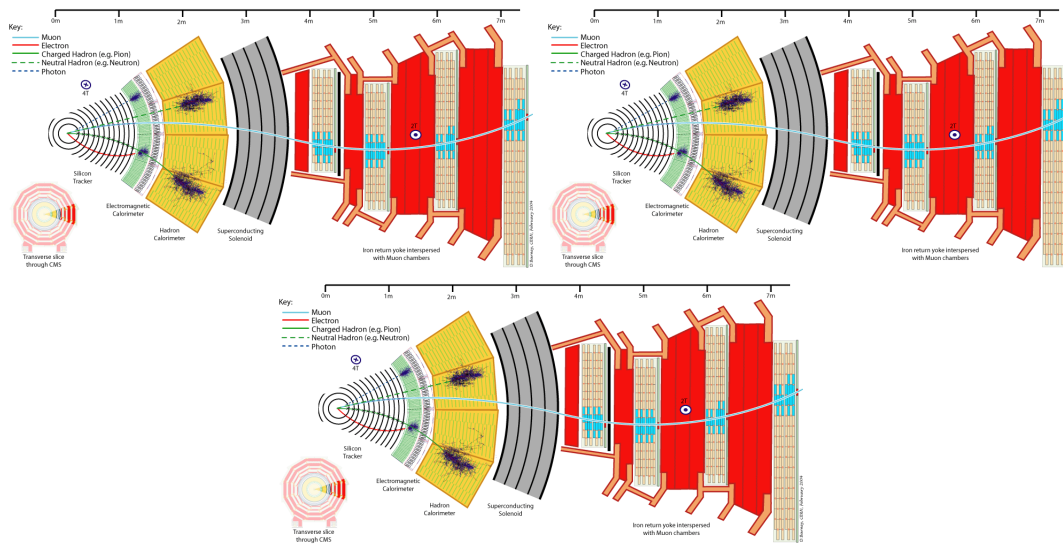
Figure 6.6: ECAL timing distribution of photons with $p_T > 80$ GeV from data showing contributions from main proton-proton collision in EB (left), EE (right) and all of ECAL combined (below). A 2.5 ns timing structure is clearly seen in EE compared to EB

with a clear 2.5 ns repeated discrete pattern with most of these photons arriving in the endcap, $1.47 < \eta < 3.0$ compared to the barrel, $|\eta| < 1.47$. These are photons originating from collisions of *Ghost* and *Satellite* bunches with either the main proton collision bunch or *Ghost/Satellite*. They contribute an irreducible amount to the photon time distribution which is very challenging to reject or estimate quantitatively. A rough estimate can be obtained by looking at ratio of the proton population in the filling profile of the LHC RF cavities as mentioned in section 3.1.5 of chapter 3 which gives a factor 10^{-5} compared to contributions from the main proton proton collision. It is observed that their main contribution is towards the endcap crystals as very few photons from these secondary collisions are produced with enough p_T compared to those from main proton bunch collisions. And even if they do, the ratio of photons from these secondary proton collision to that of the main proton-proton collision has an upper bound of 10^{-5}. Thus, the endcap is not used in this analysis for the reason that these contributions is more in the endcap and the timing resolution in the endcap is relatively poor compared to that of the barrel. The assumption of the upper bound of 10^{-5} is verified and validated using events with $Z \to e^+e^-$ as Z events must be produced from main proton-proton collisions rather than ghost/satellite collisions by studying electron candidates with time within [-2.0, 2.0] ns window. This will be explain in detail in the background estimation section which follows.

6.3 Background Estimation

A better understanding of the different background contributions to the photon ECAL time is shown using a two dimensional histogram of the photon η and ϕ against the photon seed time and the timing distribution for different jet multiplicity events. Thus the general event selection only requires that the event has at least a photon satisfying the photon selection of the previous section. The photon ECAL time inclusive distribution plots are shown in figure 6.7
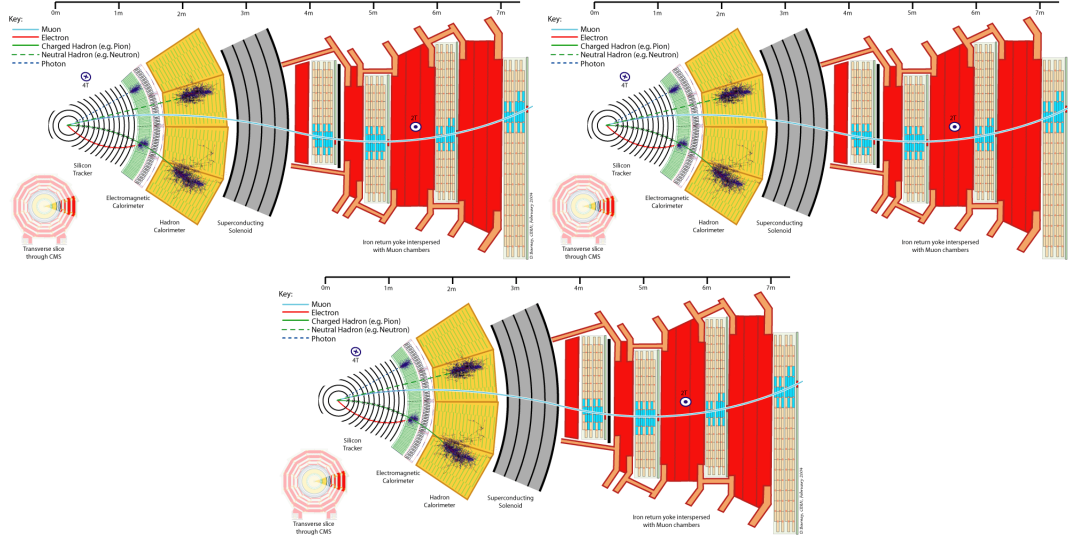
Figure 6.7: ECAL time Vs η (left) and ECAL time Vs ϕ (right) for photons with $p_{\mathrm{T}} > 80$ GeV from data. The lower plot show the photon timing distribution for events with different jet multiplicity.

From the above distributions, there seems to be contributions from quite a variety of sources. The possible sources considered in this analysis include: QCD processes which we consider to be a combination of γ+jets, multi-jets and other processes producing photons from nominal bunch collisions. Most QCD processes are expected to have minimal contribution to large timing photons and $E_{\mathrm{T}}^{\mathrm{miss}}$ with their only contributions arising from timing miss-reconstruction and $E_{\mathrm{T}}^{\mathrm{miss}}$ miss-measurements due to miss-identification of jets as photons. Events with possible or true large ECAL time with significant contributions arise from machine induce backgrounds (MIB)(arising from ghost/satellite bunch collisions), Halo muons, cosmic muons and anomalous events like spikes. These events bring significant contributions to both large photon times and large $E_{\mathrm{T}}^{\mathrm{miss}}$ where which is our possible signal sample. Thus, the data driven background estimation technique employed in this analysis is as follows:

- Divide the dataset into individual samples peculiar to the expected kinematics and observation of each individual background source,

- Identify observables based on its kinematics which can be used as variables to identify or tag and reject a particular background contribution with an acceptable

amount of efficiency,

- Used alternate samples particular to each background source to calculate and verify the event tagging and miss-tag rate or efficiency,

- Use the tagging and miss-tag rates to estimate the background contribution of each individual background source in a well defined control region (CR) or sample,

- Use another CR as a closure test sample to verify our background estimation method.

Due to a larger contribution of ghost/satellite bunch collisions observed in the endcap (EE)(see figure 6.6) and poor timing resolutions (≈ 3.0 ns), the endcap is not used in this analysis. Thus events are selected if the photon in the event is in the barrel i.e $|\eta_\gamma| < 1.47$.

In order to study the background in a data driven method, we divide the dataset into two major samples: Nominal or in-time photons whose photon ECAL time is within ± 1 ns and the event must have at least 2 jets, and Off-timing photons where the photon ECAL time is > 2 ns but < -3 ns with the event containing no jets. Our motivation is simply because the probability of a MIB or non-collision background producing an event with high jet multiplicity is small and even reduces with the p_T of of the resulting photon increases while nominal photons are mostly produced in association with jets due to the nature of QCD interactions and are mostly in-time.

By comparing these two samples, we can understand the difference and similarities between collision and non-collision backgrounds.

6.3.1 Non-Collision Backgrounds

Halo Photons

Energetic muons (energy up to 1 TeV) produced in Beam-induced backgrounds (BIB) as a result of proton losses $z = 150$ m from the interaction point of the CMS detector and inelastic proton interaction with residual gas inside the beam pipe bremsstrahlung in ECAL crystals producing photons with very high p_T and significantly large ECAL time. The rate of these BIB depends on the beam current and the operational conditions of

the LHC which include machine optics, collimator settings, residual gas densities and filling scheme. These muons which travel in a near parallel direction to normal protons in the beam pipe, referred to as halo muons are expected to leave a muons tracks in the Endcap muon systems with a corresponding associated ECAL electromagnetic cluster in the ECAL. They are also peculiar in that they travel from one side of the detector to the other along the z-direction, and their Time-Of-Flight (TOF) with respect to a potential hit position in the ECAL sub-detector can be estimated as well as measured. The expected time at ECAL of a halo muon travelling parallel along the beam line is given using a simple expression given as:

$$t_{\text{ECAL}}^{\text{expected}} = -1/c \left(\pm Z_{\text{cluster}} + \sqrt{Z_{\text{cluster}}^2 + R_{\text{cluster}}^2} \right) \tag{6.1}$$

and η dependence on this expression showing the different potential hit positions of the muons in ECAL can be seen by re-expressing this same expression in terms of η and ϕ as:

$$t_{\text{ECAL}}^{\text{expected}} = -\frac{R_{\text{cluster}}}{2c} \exp\left(-\eta\right) \tag{6.2}$$

where, Z is the cluster position or longitudinal distance along z-axis from nominal interaction point, R is the radial distance of the cluster from the beam line; $R_{\text{cluster}}^{EB} = 1.29$ m and C is the speed of light.

With this expression compared to the value from data,we select a sample (figure **??**) to study the halo properties in the negative timing distribution. Additional identification of halo muons can be performed using the the Cathode Strip Chambers (CSC) and the ECAL calorimeter information, Since halo muons are not bent in the azimuthal direction by the magnets and mainly located around the $y = 0$ plane, measuring the difference in ϕ between the CSC segment position and the ECAL photon cluster. A matching of these two referred to as $CSC(Seg, \gamma)\Delta\phi$ to within $3\,\text{deg}$ (figure 6.8) appears to provide a clear distinction between Halo photons and true photons from collision.

A distribution of the Halo photon time against the photon ϕ shows that most halo photon are distributed around $\phi = 0, \pm\pi$ as expected.
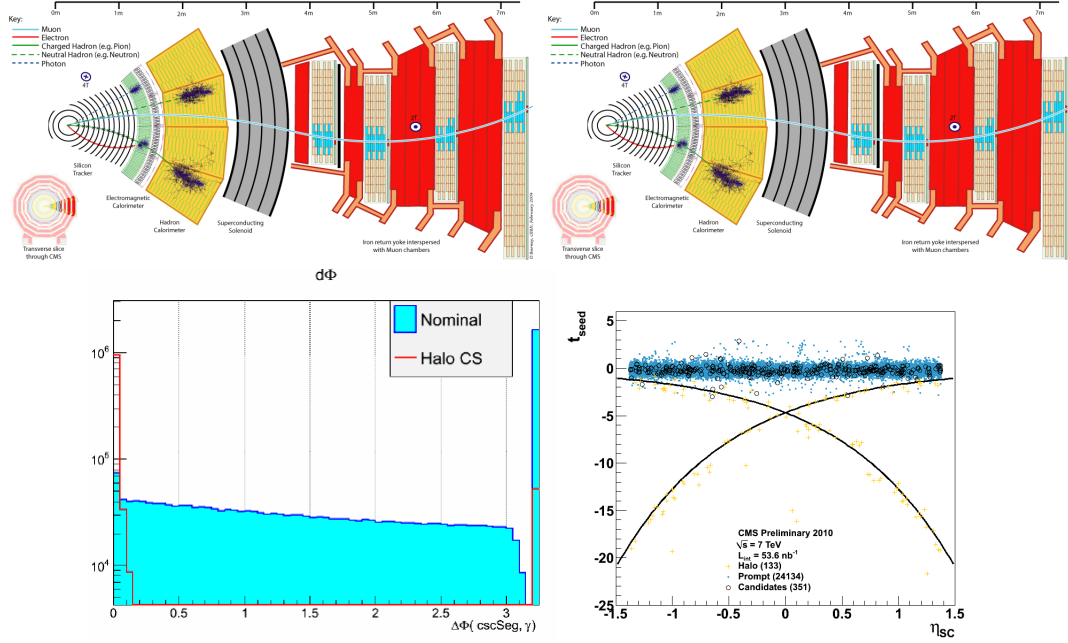
Figure 6.8: ECAL time Vs η (left) and ECAL time Vs ϕ (right) and $CSC(Seg, \gamma)\Delta\phi$ for photons with $p_{\mathrm{T}} > 80$ GeV from data. Halo photons show a clear matched between CSC segments and ECAL cluster in $\Delta\phi$ with their distribution peaking at $\phi = 0, \pm\pi$ and also the shape of their expected time.

Cosmic-Ray Photons

Cosmic muons like beam Halo muons produced with sufficient energy will bremsstrahlung in the ECAL producing photons referred here as *cosmic-ray photons*. Unlike halo muons, cosmic muons can arrive at ECAL from any direction. Nevertheless, they are expected to hits in the Drift Tubes (DT) segments. Thus, using the DT and corresponding muon photon clusters in ECAL we can match the hit position in DT segments to ECAL clusters within $\Delta\eta$ and $\Delta\phi$ between the DT segment hit and the ECAL cluster. The two dimensional distribution for $DT\Delta\eta(DT, \gamma)$ and $DT\Delta\phi(DT, \gamma)$ shown in figure 6.9 is shown for events with photon time above 2 ns and time below -3 ns. Events containing photons with small $\Delta\eta$ and $\Delta\phi$ are considered to be strong candidates for cosmic-ray photons. The same variables is used to identify cosmic-ray photons from a pure cosmic ray(data taken when there are no proton-proton collisions) sample and the distributions show very similar features as can be seen in figure 6.9.
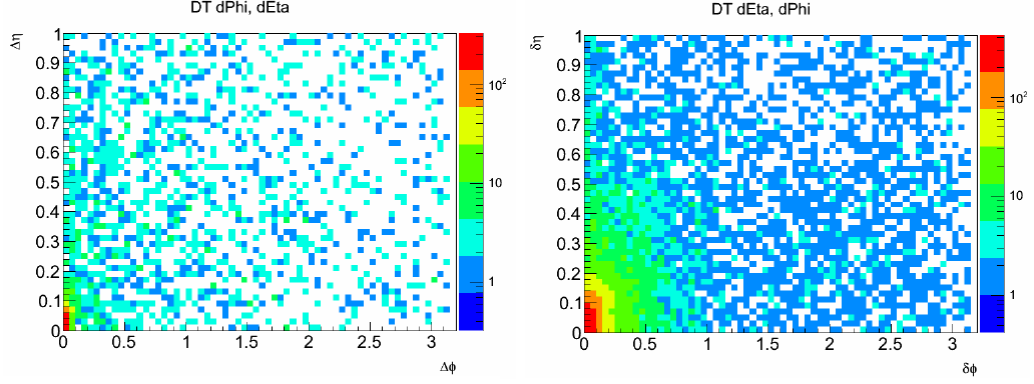
Figure 6.9: Two dimensional plot showing $DT\Delta\phi(Seg,\gamma)$ against $DT\Delta\eta(Seg,\gamma)$ for photons with $p_{\mathrm{T}} > 80$ GeV, ECAL Time > 2 ns and ECAL Time < -3 ns in proton-proton collision data (left) and non-proton-proton collision or cosmic data (right). Small $\Delta\eta$ and $\Delta\phi$ are cosmic-ray photon candidates.

Anomalous Photons: Spikes

Neutrons and some charge hadrons depositing their energy directly to the APDs instead of the crystal scintillation are referred to as *anomalous signal* or *spikes*. These spikes can mimic true photons from proton-proton collisions leading to mis-identification of spikes as photons. Spikes are easily miss-identified as energetic photons and isolated. However, most spikes show a different signal pulse shape to that of photons and also have large negative ECAL time. In addition to energy topological selection cuts and ECAL cleaning that is done during online and offline event selection, ECAL clusters belonging to spikes are usually made up of very few crystals compared to photons clusters with many crystals. Thus using the number of crystals making in a reconstructed super cluster, we can distinguish true isolated photons from events with spikes. It has been observed that spike contributions increases with increase in LHC luminosity. Thus, as a selection criteria, photons with Not identified as cosmic-ray photons or halo photons and with number of good crystals less than 7 are considered to be spike candidates. Figure 6.10 show the distribution of the number crystals in a photon super cluster comparing photons with ECAL time < -3 ns, in-time photons (ECAL $|time| < 1$ ns and a selected spike control sample. The spike control sample is selected using the "swiss-cross" variable which is used to identify and reject events with spikes during super cluster reconstruction.
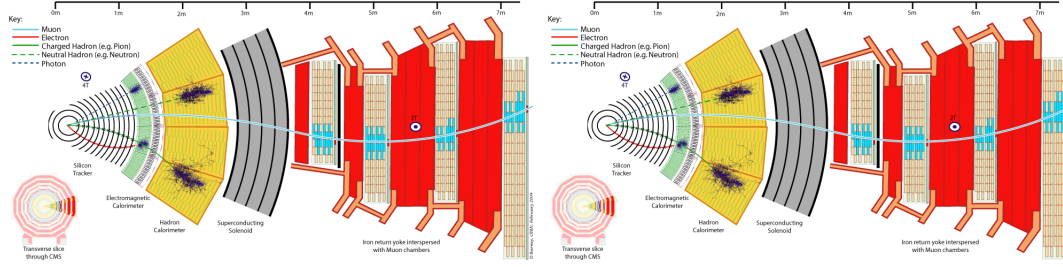
Figure 6.10: Plot showing Number of crystals in photon super cluster for photons with $p_\mathrm{T} > 80$ GeV, ECAL Time < -3 ns (blue), control region ($|t| < 1.0$ ns (black) and spike control sample (red).

6.3.2 Collision Backgrounds

QCD Photons and Pile Up

The LHC provides proton-proton collisions every 25 ns, however during the 2012 LHC run, these bunch spacing time increased to 50 ns. However, as discussed in section 3.1.5 on LHC Bunch structure, the presence of Satellite/ghost bunches spaced in 5.0 ns or 2.5 ns can also contribute to producing delayed photons either from collisions between these satellite/ghost bunches or with the main proton bunch collisions. As observed in figure 6.6, photons from these events are a serious background source to delayed photons and most of these photons will pass all the above event and photon criteria selections. Thus, a careful estimation of this contribution is the major task of the background estimation in this analysis. The kinematics of these events are very similar and as a result, we employ the standard ABCD method to for estimating these background contribution to the signal region.

First before proceeding, we should mention another possible concern which deals with the difference in the measurement of $E_\mathrm{T}^\mathrm{miss}$ in most analysis which mostly require events to be *in-time* to this analysis whose event selection has been extended to include *Out-of-time* events.

$E_\mathrm{T}^\mathrm{miss}$ Re-Calculation

The presence of timing cuts of $|t_{RECO}| > 3.0$ ns in EB in the official CMS electromagnetic super cluster reconstruction as an "out-of-time" event cleaning procedure, results

in a difference in the calculation of E_T^{miss} for "in-time" events ($|t_\gamma| < 3.0$ ns) and "out-of-time" events ($|t_\gamma| > 3.0$ ns). Out-of-time photons are not taking into consideration when calculating the total transverse momentum of an event to derived the total transverse momentum imbalance, thus, we have to recalculate the E_T^{miss} for events with out-of-time photons taking into consideration p_T contributions from these out-of-time photon. This results in us using two different sets of E_T^{miss} whose definition are given as follows:

1. $E_T^{\text{miss}}{}_1$: E_T^{miss} for events where photon p_T contributions is not included during E_T^{miss} measurements.

2. $E_T^{\text{miss}}{}_2$: E_T^{miss} of the event taking into account out-of-time photon p_T contributions in E_T^{miss} measurements.

The distributions for $E_T^{\text{miss}}{}_1$ and $E_T^{\text{miss}}{}_2$ against ECAL time can be seen in figure 6.11.
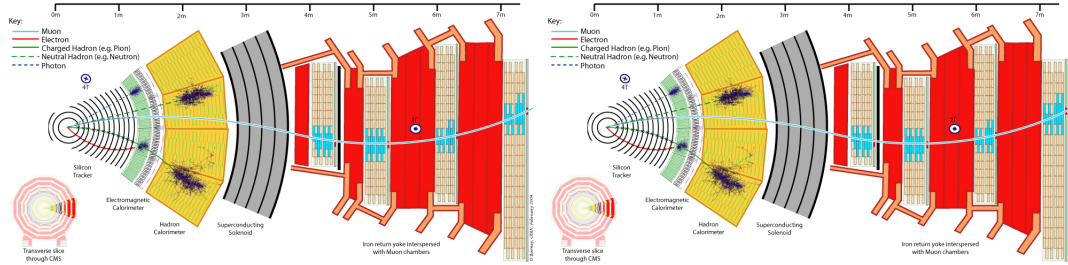
Figure 6.11: Figure showing E_T^{miss} distributions for events with out-of-time and in-time photons with $p_T > 80$ GeV. $E_T^{\text{miss}}{}_1$ and $E_T^{\text{miss}}{}_2$ definitions are given in context.

6.3.3 Event Cleaning

Using the above observables for studying halo, cosmic and spike photons we reduced the contribution of these events by applying in addition to our above selections the following selections:

- Veto 0-jet events as this sample is highly populated with beam halo events,

- Veto events with $CSC(Seg, \gamma)\Delta\phi < 0.05$,

- Only photons with $|\eta_\gamma| < 1.45$ are considered,

- Photons must have Number of Good crystals > 7,

- Photons tagged as halo and cosmic are removed,

- Event must have at least 1-jet.

Events which pass all these additional selection criteria make up the sample which is used to estimated the background to our signal.

In order to estimating the background contribution from collision and non-collision sources, we employ a 3-dimensional space involving $E_T^{miss}{}_1$, $E_T^{miss}{}_2$ and ECAL time. Our signal region is events with $t > 3.0$ ns and large E_T^{miss} where by large E_T^{miss} we mean events with large $E_T^{miss}{}_1$ and $E_T^{miss}{}_2$. Non-collision events have large time as they are mostly out-of-time and by E_T^{miss} calculation requirements should have large $E_T^{miss}{}_2$. While collision produced backgrounds events are mostly in-time and may often be measured with $t > 3.0$ ns due to either mis-reconstruction or from ghost/satellite contributions. However, these events cannot be produced with large correctly calculated E_T^{miss} because for example in $\gamma+$ jets events, very small E_T^{miss} due to energy miss-measurements is expected to be produced. But if the collision event is produced and arrives at ECAL with $t > 3$ ns, and the E_T^{miss} is not properly calculated (since events with photons ECAL time, $|t| > 3$ ns are rejected during standard super cluster reconstruction with their p_T contribution not taken into account in the E_T^{miss} calculation) which in this case is large $E_T^{miss}{}_1$, they will fluctuate or be easily considered as additional contribution to the non-collision background estimation in our signal region. Therefore, we select samples or control regions (CR) which enhances each interested background source and use that CR to estimate the enhanced background contribution taking into account the possible contamination of an alternate background source due to possible fluctuations in event rate. The overall estimation technique is verified through a closure test procedure and the collision background estimation verified and validated using an extra control sample of $Z \to \ell\ell$ events where the ℓ are electron candidates reconstructed using photon candidates extended to include out-of-time events.

Signal Region: Events with $E_T^{miss}{}_2 > 60$ GeV, $E_T^{miss}{}_1 > 60$ GeV and $t > 3.0$ ns.

$E_\text{T}^\textbf{miss}{}_2 > 60 \textbf{ GeV}$: CR in which collision (QCD) background is suppressed while that for halo, cosmic ray and spike photon are all enhanced. Within this space, we define four regions representing ABCD to estimate the the background contribution:

- A: Events with $E_\text{T}^\text{miss}{}_1 < 60$ GeV and $t < -3.0$ ns.

- C: Events with $E_\text{T}^\text{miss}{}_1 < 60$ GeV and $t > 3.0$ ns.

- B: events with $E_\text{T}^\text{miss}{}_1 > 60$ GeV and $t < -3.0$ ns.

- D: events with $E_\text{T}^\text{miss}{}_1 > 60$ GeV and $t > 3.0$ ns.

Thus, the number of events expected in CR D under the assumption that $\frac{N_D}{N_B} = \frac{N_C}{N_A}$ is given as:

$$N_D = \left(\frac{N_B}{N_A}\right) \cdot N_C \tag{6.3}$$

$E_\text{T}^\textbf{miss}{}_1 > 60 \textbf{ GeV}$: CR in which non-collision background (halo, cosmic and spike photons) contribution is suppressed wheras collision (QCD) background contribution is enhanced. Further dividing this CR into according to A',B',C',D' to estimate its contribution where:

- A': Events with $E_\text{T}^\text{miss}{}_2 < 60$ GeV and $t < -3.0$ ns.

- B': Events with $E_\text{T}^\text{miss}{}_2 > 60$ GeV and $t < -3.0$ ns.

- I': Events with $E_\text{T}^\text{miss}{}_2 < 60$ GeV and $|t| < 2.0$ ns.

- I: Events with $E_\text{T}^\text{miss}{}_2 > 60$ GeV and $|t| < 2.0$ ns.

we also define a in time CR as:

- C': Events with $E_\text{T}^\text{miss}{}_2 < 60$ GeV and $t > 3.0$ ns.

- D': Events with $E_\text{T}^\text{miss}{}_2 > 60$ GeV and $t > 3.0$ ns.

- I': Events with $E_\text{T}^\text{miss}{}_2 < 60$ GeV and $|t| < 2.0$ ns.

- I: Events with $E_\text{T}^\text{miss}{}_2 > 60$ GeV and $|t| < 2.0$ ns.

Now using using the above regions we can estimate the contributions of collision background in both CRs B and D as follows:

$$N_{col}^B = N_{B'} = \left(\frac{I}{I'}\right) \cdot N_{A'}, \qquad N_{col}^D = N_{D'} = \left(\frac{I}{I'}\right) \cdot N_{C'} \qquad (6.4)$$

where we have assumed that $\frac{N_{B'}}{N_{A'}} = \frac{N_I}{N_{I'}}$ and $\frac{N_{D'}}{N_{C'}} = \frac{N_I}{N_{I'}}$.

N_{col}^B and N_{col}^D are collision contributions to CRs B and A such that the final non-collision background estimation (since the dominant contribution to total background is the non-collision background source) is given as:

$$N_{\text{Total}}^D = \left(\frac{N_B - N_{col}^B}{N_A}\right) \cdot N_C + N_{col}^D \qquad (6.5)$$

where $N_{\text{Total}}^D = N_{\text{non-col}}^D + N_{col}^D$ is the total background estimation in our signal region. A diagram showing the above background estimation technique is shown in figure 6.12.
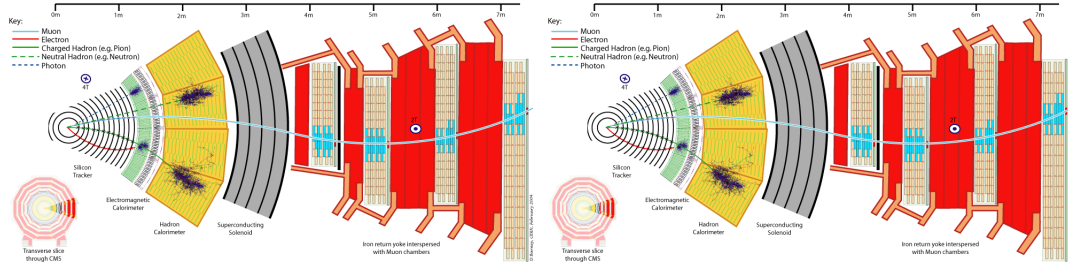
Figure 6.12: Diagrams showing background estimation technique.

A closure test using events with $0 - $ jets and $1 - jet$ is used to verify the above background estimation technique and the above assumptions are cross checked using $Z \to e^+e^-$ events. The underlying assumption here is that background contributions to large timing from collision source referred here as QCD is very small and must be of the order of 10^{-5} in comparison to in-time photons. i.e the ratio $N_{t>3\ ns}/N_{|t|<2.0\ ns} \approx 10^{-5}$ with N being the number of photons.

Closure Test

By selecting a sample of events containing only a single jet, we verify the validity of

our method of background estimation using a closure test. The closure test is simply comparing the number of events we observed in our signal region D with the number we expect from using our $ABDC$ background estimation method. Using a equation 6.3.3, we observed a total of 5-events when we expected $6.44^{+2.95}_{-3.45}$ which is quite close. This gives us confidence that our background estimation method is robust and reliable and we can now move on to do our final background estimation on dataset with events having at least 2-jets passing our final photon, jet and $E_{\mathrm{T}}^{\mathrm{miss}}$ selection after being cleaned.

6.3.4 Background Estimation Cross Check

The main assumption in our background estimation technique is that, the contribution from collision background events to our signal region ($|time| > 3$ ns) is negligible. In order to show this we select $Z \rightarrow e^+e^-$ events from `SingleElectron/` and `DoubleElectron/` data sets of 2012. The selection criteria of our extended to include out-of-time Z candidates events is as follows:

- The candidate two electrons for the Z bosons must have individual $p_{\mathrm{T}} > 20$ GeV,

- The di-mass of these two electrons, $|m_{\ell_1,\ell_2} - 91| > 61 \ GeV/c^2$,

- Each electron must be in the barrel, $|\eta_{\ell_1}| < 1.479$ and $|\eta_{\ell_2}| < 1.479$.

At the electron super cluster level, we used the seed crystal time adjusted accounting for the effects due to electron time of flight as the electron time, after the seed crystal has passed all the recommended crystals or rechit cleaning criteria recommended by the ECAP DPG such as *kWeird, kBad, kPoorCalib* used in rejecting crystals showing anomalous behaviours like spikes, noisy, bad crystals and poorly calibrated crystals. In this cross-check, we define our signal region as Z-candidate events with a well defined mass from both electrons i.e $71 < |m_{\ell_1,\ell_2} < 100 \ GeV/c^2$ while the Control sample consists of events which do not fall into the signal category. A quick look at the similar plots to figure 6.8 of the electron candidates from the Single/DoubleElectron data compared to the singlePhoton dataset as seen in figure 6.13 indicate that contribution from cosmic, halo and anomalous photon events is much reduced and thus makes the Z boson candidate events sample a reliable sample to disentangle non-collision contributions and only study collision background contributions as initial objective.
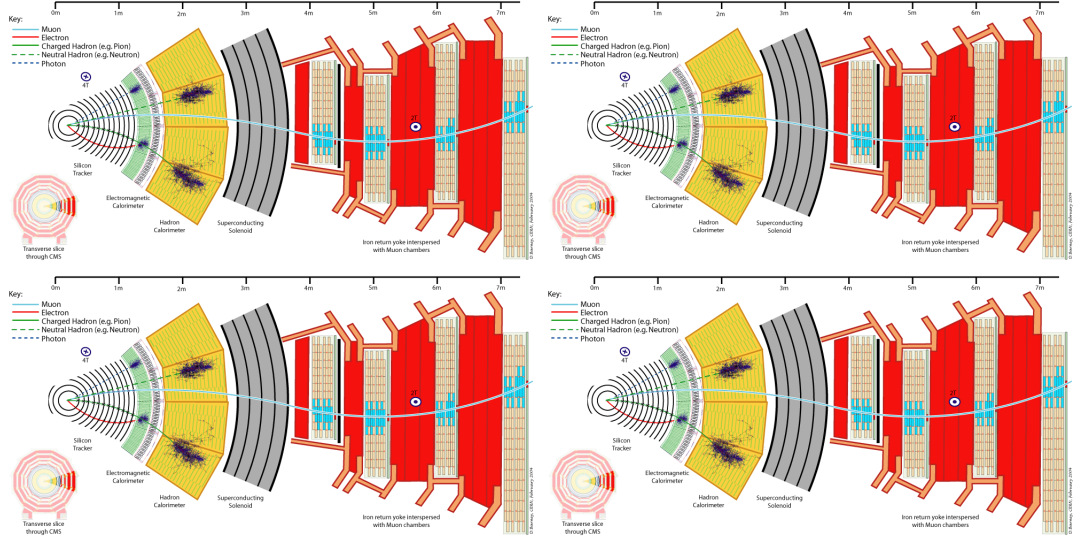
Figure 6.13: ECAL time Vs η and ECAL time Vs ϕ (left) for photons from SinglePhoton dataset (left) similar plots from the DoubleElectron dataset (right). Photons at $\phi = 0, \pm\pi$ which are mostly halo photons not observed in the Z boson candidate sample.

Figure 6.14 shows the Z boson mass reconstructed from the candidate electrons and timing of each electron for Signal (left and blue) and for our control sample (right and red).
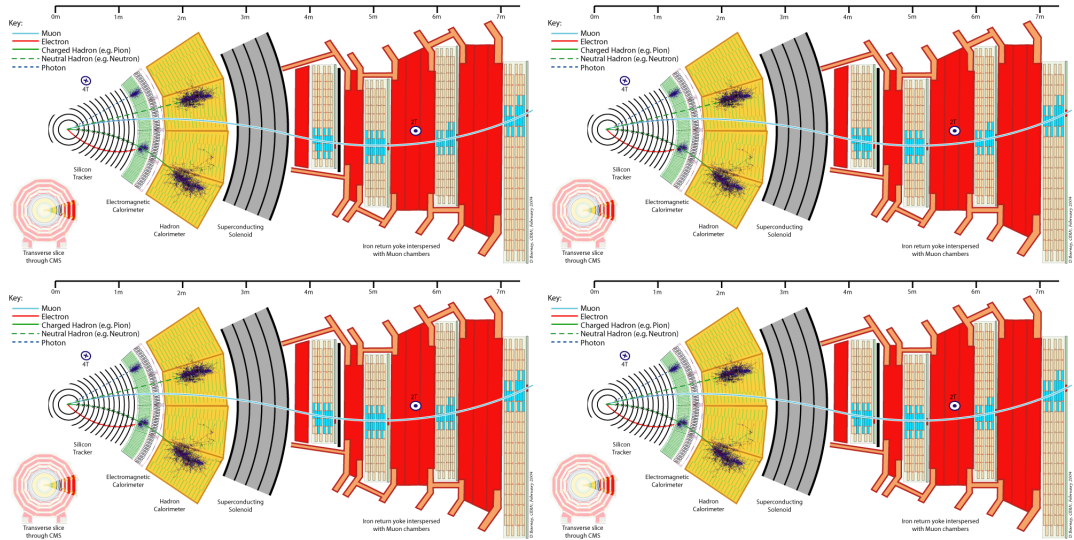
Figure 6.14: Di-electron candidate mass distribution and the time of both electrons for the signal $71 < |m_{\ell_1, \ell_2} < 100 \ GeV/c^2$ Z boson sample(left) and similar distributions from the Control (outside signal region) sample (right). Candidates events from the DoubleElectron dataset.

Using the control sample, we estimate its contribution using simple scaling which can be understood as an ABCD method into the signal sample as follows:

- Using a polynomial function, we fit the di-electron candidate mass distribution of the control sample to extract a set of fit parameters,

- Using the fit parameters, define our polynomial fit function to be used to extract our scaling factor and hence true contribution of the control region events in our signal region which in this case are Z bosons with possible large timing, $|t| > 3$ ns.

- Scale the control sample events (electrons time) by this extracted scale factor i.e

$$\text{Scale Factor} = \frac{N}{M_1 + M_2}$$

.

- By subtracting the scaled control sample event timing distribution from the signal sample electron time distribution, we are left with the true Z boson events whose electron time can extend to large time.

- Comparing the total number of observe electron candidates with $t > 3$ ns to those with time within the required in-time $|t| < 2$ ns using a ratio i.e $N_{t>3 \ ns}/N_{|t|<2.0 \ ns}$ gives us an estimate of the possible genuine collision electromagnetic objects with large timing.

A simple picture showing the above procedure with distributions is shown in figure 6.15.
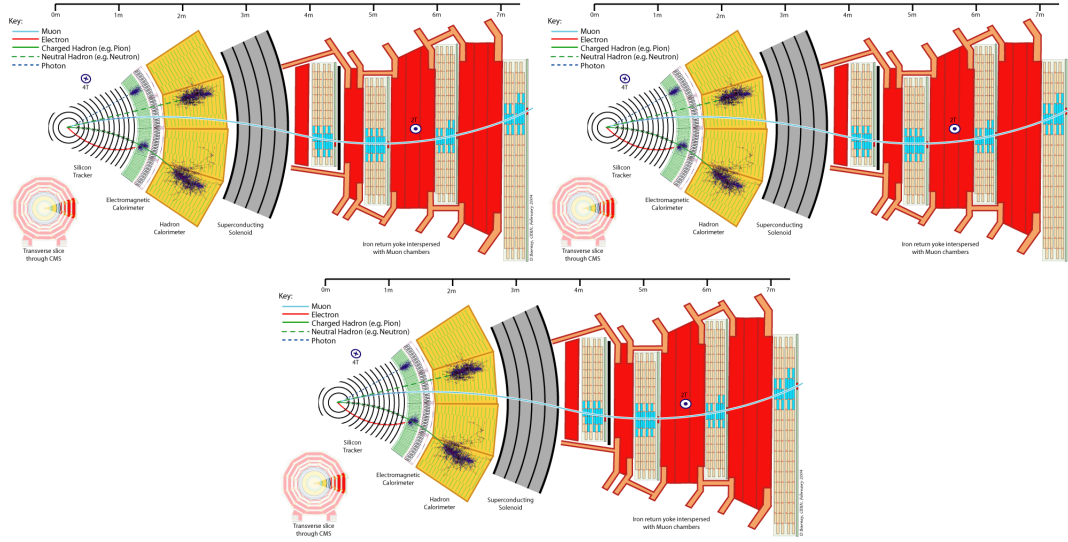
Figure 6.15: *Top*: Control sample (left) and signal sample (right) of di-electron candidate mass distribution. *Bottom:* Figure showing definition of scale factor use in estimating the contributions from control sample in signal sample.

The result of the final timing distribution of genuine Z boson events can be seen in figure 6.16. It is not difficult to see that the ratio $N_{t>3\ ns}/N_{|t|<2.0\ ns} < 10^{-5}$ confirming that indeed the contribution of electromagnetic objects with large timing $t > 3$ ns is negligible thus confirming that most collision events contain photons which are mostly in-time, $|t| \leq 2$ ns. A simple cut on the $E_{\mathrm{T}}^{\mathrm{miss}}$, $E_{\mathrm{T}}^{\mathrm{miss}} > 60$ GeV will further reduce this ratio to 0 as assumed in our above background estimation.

Figure 6.16: Timing distribution of genuine Z bosons after background contribution has been subtracted.

6.4 Results

We have used only the photon arrival time at ECAL to distinguish signal from SM background with our acceptance region being photons with ECAL time $|t| > 3.0$ ns. The final number of events estimated for each background component and observed from data after passing all our selection cuts is shown in table 6.6.

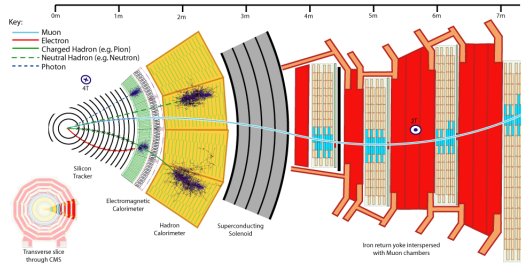| SM Background/SPS8 GMSB Signal	Number of Events
QCD (Collision)	000.00 ± 0.000
Halo Photons	000.00 ± 0.000
Cosmic Photons	000.00 ± 0.000
Anomalous photons/Spikes	000.00 ± 0.000
Total SM background	000.00 ± 0.000
Data	000.00 ± 0.000
GMSB(SPS8) ($\Lambda = 180$ TeV,$c\tau = 500$ mm)	000.00 ± 0.000
GMSB(SPS8) ($\Lambda = 180$ TeV,$c\tau = 1000$ mm)	000.00 ± 0.000
GMSB(SPS8) ($\Lambda = 180$ TeV,$c\tau = 2000$ mm)	000.00 ± 0.000
GMSB(SPS8) ($\Lambda = 180$ TeV,$c\tau = 3000$ mm)	000.00 ± 0.000
GMSB(SPS8) ($\Lambda = 180$ TeV,$c\tau = 6000$ mm)	000.00 ± 0.000
GMSB(SPS8) ($\Lambda = 180$ TeV,$c\tau = 12000$ mm)	000.00 ± 0.000

Table 6.6: Final number of events estimated for each background and the number of events passing out event selection and acceptance criteria.

6.4.1 Systematics Studies

The different sources of systematics which affect this analysis and the estimated contribution of each identified systematics is used in the calculation of the upper limit on observed signal cross-section is shown in table 6.7. The systematic uncertainty on luminosity measurement has the recommended value of 2.2%. The uncertainty for the jet energy scale correction has also been measured using the standard CMSSW tool by [46]. The uncertainty on the photon energy scale in barrel was estimated to be 1.0% and based on the final-state radiation (FSR) in $Z \rightarrow \mu\mu\gamma$ events [47]. The uncertainty from pardon density functions (PDF) evaluated using the re-weighting technique and

Master equation of CTEQ65 model set described in [48]. The uncertainty on the E_T^{miss} resolution uses a conservative estimate from [49]. The uncertainty on the ECAL timing obtained be comparing the peak in the timing distribution between $\gamma+$ jet sample and data events with time $|t| < 2$ ns to be of the order of 200 ps per event and from a study of high p_T photons beyond gain transitions and has been agreed by ECAL DPG to be a conservative estimate. Another important source of systematics is in the selection of the background control samples and estimation and individual systematics in the tagging and miss-tagging of non-collision background and also with the estimation of background contributions from collisions. All these separate systematics contributions have been combined into a single background estimation systematics referred to as background estimation systematics. The summary of every systematics in shown in table 6.7.

Source	Uncertainty on $\sigma_{UL}^{Exp}(\%)$
Photon energy scale (1.0%)	$< 3.0\%$
Jet energy scale	$< 0.05\%$
Jet energy resolution (10%)	$< 1.90\%$
PDF uncertainty (10%)	$< 1.70\%$
E_T^{miss} resolution (10%)	$< 2.8\%$
ECAL time uncertainty (0.5 ns)	$< 5.0\%$
Background estimation uncertainty (20.0)	$< 10.0\%$
Luminosity (4.5%)	$< 2.2\%$

Table 6.7: Summary of systematic uncertainties on the signal (top), background (middle) and machine (bottom) as used in the σ_{UL} calculation.

Chapter 7

Limit Calculation

7.1 Limit Calculation

The upper limit calculation procedure used in this analysis is the CLs technique. We fed carefully estimated amounts of background and signal with systematics to obtain the limit. The variable for which the 95% upper limit is set unlike previous experiments is based entirely on the neutralino proper decay length, $c\tau_{\tilde{\chi}_1^0}$.

The method we used in our upper limit calculation is by first performing a Hypothesis test and then use the result of this test to derived our confidence intervals. We do the following:

- We define a NULL hypothesis (H_0) and the Alternate hypothesis (H_1). If we had several other hypothesis, we will defined them also.

- Select a Test statistics ($t(x)$), where x is the data.

- Select a corresponding test statistics calculator.

- Use the result of the hypothesis test to compute the interval by inverting the result of the hypothesis test.

First, we describe the acceptable technique in experimental high energy physics for computing *p-values* used in any search and discovery experiment.

7.1.1 CLs Technique

The CL_s technique [50] is attributed as the standard technique or framework for computing the confidence or exclusion intervals in a search and discovery experiment. It has been shown to to work during the search for the Higgs boson at LEP and recently in the discovery of the scalar boson in 2012, by both CMS and ATLAS experiments with the mass of this boson being: $m_H = 125.36 \pm 0.37(stat.Unc) \pm 0.18(syst.Unc)$.

This method has been implemented in a unique statistical software package called *HiggsCombine* with the goal of providing direct access to a variety of robust statistical methods with optimised performance for computing limits or confidence intervals. HiggsCombine [52] is the official standard tool recommended by the CMS statistical committee and CMS Higgs group for calculating limits in any CMS search and discovery analysis. It takes as input estimates on the number or distribution of signal and background and the observed number or distribution from data and produces an upper limit in the production cross section of a given physics process for a given value of a parameter of interest (POI). Higgscombine tool has the advantage in that, it allows for the possibility to use several different statistical methods of calculating the upper limit. This way, one can make comparison and simple checks for any inconsistency. In this analysis, we used an Asymptotic [53] and HybridNew (a hybrid of Frequentist and Bayesian methods),[52], to calculate our observed upper limits. The purpose of the using the CL_s method is to compute reliable upper limits in a search scenario when the observed signal is very small compared to the background. In the CL_s technique, one uses not the p-value (CL_{s+b}) but rather divide this by CL_b (which is 1 minus the p-value for background only hypothesis). The reason for this is to define a conditional probability conditioned to the scenario of observing only background or background only hypothesis. The CL_s is formally defined as:

$$CL_s = \frac{CL_{s+b}}{CL_b} = \frac{p_{s+b}}{1 - p_b} \tag{7.1}$$

where $s + b$ means signal and background.

7.1.2 Statistical Test Formalism

The Neyman-Pearson Theorem states that the likelihood ratio gives the most powerful hypothesis test. Therefore, we construct our test statistics t_μ as a function of the observed data, as a likelihood ratio. In a search analysis, one defines the null hypothesis H_0 describing only known processes, or the background only which is to be tested against an alternate hypothesis H_1 defined as a background and signal. However in the computation of upper limits:

- H_0 being the NULL hypothesis includes the background and signal $(s + b)$ while

- H_1 being the ALTERNATE hypothesis includes only the background (b).

Using these, two hypothesis we quantify the level of agreement between our observed data with either of the hypothesis by computing a p-value (p-value if the probability under the assumption of a given hypothesis, of finding data of equal or greater incompatibility with the predictions of the given hypothesis). A given hypothesis is then regarded as being excluded if its p-value is observed below a given threshold. In particle physics, this threshold value for the p-value is 0.05 corresponding to 95% of confidence level (CL). The CMS accepted method of computing upper upper limit is based on mix of frequentist-hybrid significance test using the profilelikelihood ratio as a test statistics (HybridNew method). The parameter of interests in in our case the rate (cross section) of signal process as well as *nuissance parameters* as systematics for the background and signal models. This parametrized systematics effects results, as is always the case, to loss in sensitivity.

In this search experiment, for each event in the signal, we measured the timing of the photon as our observable. We use this value to construct a histogram $\mathbf{n} = (n_1, \cdots, n_N)$. The expectation value for each value of n_i can be written as:

$$E[n_i] = \mu s_i + b_i \qquad (7.2)$$

where μ is the parameter which determines the signal strength, when $\mu = 0$ means background-only and when $\mu = 1$ then we have the signal and background hypothesis.

The the mean number of entries in the ith bin from signal and background are given as:

$$s_i = s_{tot} \int_{bin,i} f_s\left(t; \theta_{\mathbf{s}}\right) \quad b_i = b_{tot} \int_{bin,i} f_b\left(t; \theta_{\mathbf{b}}\right) \tag{7.3}$$

with the functions $f_s\left(t; \theta_{\mathbf{s}}\right)$ and $f_b\left(t; \theta_{\mathbf{b}}\right)$ being the probability density functions (Pdfs) of the variable t for the signal and background events and $\theta_{\mathbf{s}}$ and $\theta_{\mathbf{b}}$ representing the parameters which characterise the shapes of the pdfs. s_{tot} and b_{tot} represents the total mean numbers of signals and backgrounds while the integrals represent the probabilities for an event to be found in bin i. $\theta = (\theta_{\mathbf{s}}, \theta_{\mathbf{b}}, b_{tot})$ denote all nuisance parameters (systematic uncertainties) while s_{tot} is the signal normalization is fixed to the value predicted by the nominal signal model.

The likelihood function is the product of the Poisson probabilities for all bins:

$$\mathcal{L}\left(\mu, \theta\right) = \prod_{r=1}^{N} \frac{\left(\mu s_r + b_r\right)^{n_r}}{n_r!} e^{-\left(\mu s_r + b_r\right)} \cdot \mathcal{G}(\theta) \tag{7.4}$$

where $\mathcal{G}(\theta)$ is a discrete (Poisson) distribution of the nuisance parameters. This distribution can be different for different nuisance parameter.

Using the likelihood function, the profilelikelihood ratio is then defined as:

$$\lambda(\mu) = \frac{\mathcal{L}(\mu, \hat{\hat{\theta}})}{\mathcal{L}(\hat{\mu}, \hat{\theta})} \tag{7.5}$$

Here $\hat{\hat{\theta}}$ is the the value of θ that maximizes $\mathcal{L}$ for a specified μ, thus, it is referred to as the *conditional maximum-likelihood estimator* (CMLE) of θ (given as a function of μ). While $\mathcal{L}(\hat{\mu}, \hat{\theta})$ is the maximized (unconditional) likelihood function with $\hat{\mu}$ and $\hat{\theta}$ being its *maximum likelihood* (ML) estimators. The nuisance parameters broadens the profilelikelihood as a function of μ relative to what is expected if their values where fixed and this reflects in the loss of sensitivity or information about μ due to the systematic uncertainties.

7.1.3 Test Statistics and p-values

The above expression for $\lambda(\mu)$ shows that $0 \leq \lambda \leq 1$, where λ close to 1 indicates a very good agreement between the data and hypothesis value of μ. The test statistics to be used for our statistical test is defined as:

$$t_\mu = -2 \ln \lambda(\mu) \tag{7.6}$$

It is important to note that the test statistics approach to any statistical test is favourable because just be looking at the values of the test statistics, higher values corresponds to increasing incompatibility between the data and the value of μ which is from the signal hypothesis. This incompatibility or disagreement between the data and a given hypothesis is quantified by calculating the probability or p-value as:

$$CL_{s+b} = p_u = \int_{t_{\mu,obs}}^{\infty} f(t_\mu|\mu)dt_\mu \tag{7.7}$$

where, $t_{\mu,obs}$ is the value of the test statistics t_μ obtained from the data and $f(t_\mu|\mu)$ is a pdf constructed from t_μ depending on the signal strength μ. The set of values for μ that a rejected because their p-value is below a specified threshold value α lying on either sides of those not rejected gives a two sided confidence interval of μ and if just on one side of the ones not rejected gives an upper limit on the rejected values of μ.

In the background only scenario i.e $\mu = 0$, the test statistics is defined as:

$$q_\mu = \begin{cases} -2 \ln \lambda(0), & \hat{\mu} \geq 0 \\ 0, & \hat{\mu} \leq 0 \end{cases}$$

where $\lambda(0)$ is the profilelikelihood ratio for $\mu = 0$ defined in 7.5. and again to quantify the disagreement between the background-only hypothesis ($\mu = 0$) and the data is given by the p-value as:

$$CL_b = p_0 = \int_{q_{0,obs}}^{\infty} f(q_0|0)dq_0 \tag{7.8}$$

where $f(q_0|0)$ denotes the pdf if the test statistics q_0 under the background-only ($\mu = 0$) hypothesis. Figure 7.1 shows a sampling distributions of the test statistics and how the

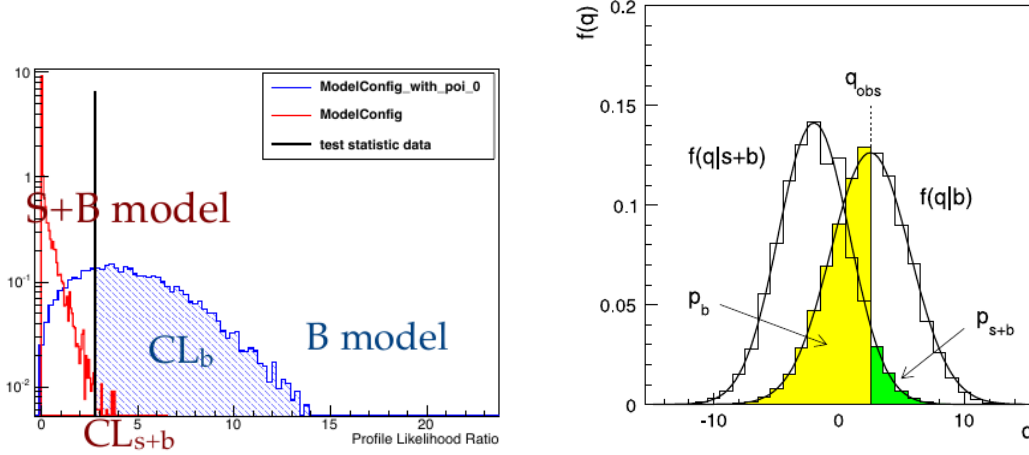p-values can be extracted from these distributions.

Figure 7.1: Sampling distributions for $f(t_\mu|\mu)$ showing how one extracts the p-vlaues. left: is the using a analytic of the Asymptotic method and right: is from the HybridNew method.

In addition to the p-value, for expressing the disagreement between the data and a given hypothesis, the Higgscombine tool also provides a quantity known as the *significance* ($\mathcal{Z}$). $\mathcal{Z}$ and the p-value have a very non-linear relation. Once can defined that relation using a two-sided fluctuation if a Gaussian variable σ, with 5σ significance corresponding to a p-value of $p = 5.7 \times 10^{-7}$ to denote a discovery. Since, we have not observed any significant excess of events over our standard model background, we will not mention a lot about significance in this thesis, but rather talk about p-values as they are indispensable in computing limits.

The important question is always, how does one obtain an expression or a distribution of the test statistics and $f(t_\mu|\mu)$ from the likelihood function? To answer this question, the HiggsCombine tool was developed which consist of various ways of both analytically (e.g the Asymptotic statistical method [53]) or through numerical integration or Monte Carlo computation (e.g the HybridNew statistical method) obtain the test statistics and $f(t_\mu|\mu)$. We have shown the limit computation results of both methods as used in this analysis. As an example, the pdf $f(q_\mu|\mu)$ of the test statistics (q_μ)

obtained though the Asymptotic statistical method as given in [53] is:

$$f(t_\mu|\mu') = \Phi\left(\frac{\mu - \mu'}{\sigma}\right)\delta(t_\mu) + \frac{1}{2}\frac{1}{\sqrt{2\pi}}\frac{1}{t_\mu}\exp\left[-\frac{1}{2}\left(\sqrt{t_\mu} - \frac{\mu - \mu'}{\sigma}\right)^2\right] \qquad (7.9)$$

where result to a half-chi-square distribution when $\mu = \mu'$.

In subtle point worth mentioning is that in the HybridNew approach, systematics uncertainties are taken into account through the Beyesian prior density $\pi(\theta)$, and the distribution of the test statistics is computed under the assumption if the Beyesian model of average given as:

$$f(q) = \int f(q|\theta)\pi(\theta)d\theta$$

and the prior pdf $\pi(\theta)$ is obtained from some measurements characterised by a given likelihood function $\mathcal{L}_\theta(\theta)$ which is then used to find the prior using Bayes' Theorem. Unlike other cases where systematic uncertainties are taking as being part of the data and incorporated directly through $\mathcal{G}(\theta)$ as shown in equation 7.4. Nevertheless, they arrive at the same result.

In summary, the hypothesis test is performed using a given statistical method on each value of a chosen parameter of interest (POI)(usually denoted μ). The p-value if obtained from the sampling distribution of the test statistics being used. Can either obtain this test statistics analytically or through Monte Carlo computation and numerical integration. By plotting the p-value as a function of the POI, we obtain the p-value curve (in this case the $CL_s = \frac{CL_{s+b}}{CL_b}$). The value of μ which has a p-value α (e.g 0.05) is the upper limit (for 1-dimensional limits,2-dimensional limits gives lower and upper limits) of $1 - \alpha$ confidence interval (e.g 95%).
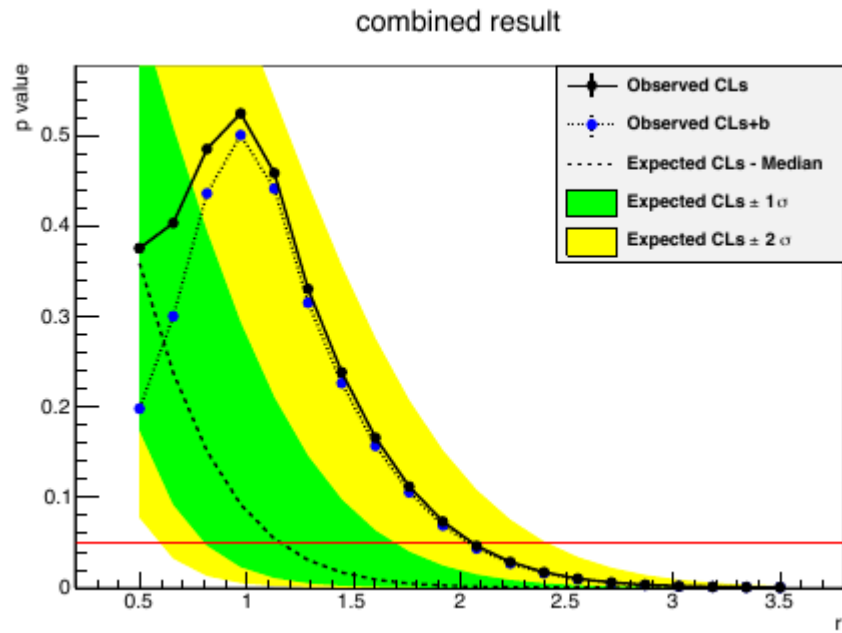
Figure 7.2: Distribution of p-vlaues showing how upper limit on μ is extracted for a given threshold probability.

Chapter 8

Limit Interpretation

Using the CL_s technique, the HiggsCombine tool produces an upper limit along with the expected limit at different quantiles as the signal strength computed which is a ratio of Number of Signal events over the Number of Expected signal events i.e

$$r = \frac{N^{Obs}}{N_{expect}} \tag{8.1}$$

and using the equation as given in chapter 3 on the cross-section $\sigma = \frac{N}{\varepsilon \cdot A \cdot \mathscr{L}}$ and hence the observed cross-section upper limit is given as:

$$\sigma_{UL}^{Obs} = \frac{r \cdot N^{expect}}{\varepsilon \cdot A \cdot \mathscr{L}} \tag{8.2}$$

where $\mathscr{L}$ is the integrated luminosity $(19\,\mathrm{fb}^{-1})$ and ε and A are the signal selection efficiency and Acceptance respectively. In addition to the observed limits (Solid black line), the uncertainties on the expected limits at $68\%/16\%$ $(\pm 1\sigma)$ and at $98\%/2.5\%$ $(\pm 2\sigma)$ provide the GREEN and YELLOW respectively, the error from the median (50%) expected limits (dashed red line) shown in figure 8.2.

8.1 Signal Efficiency and Acceptance

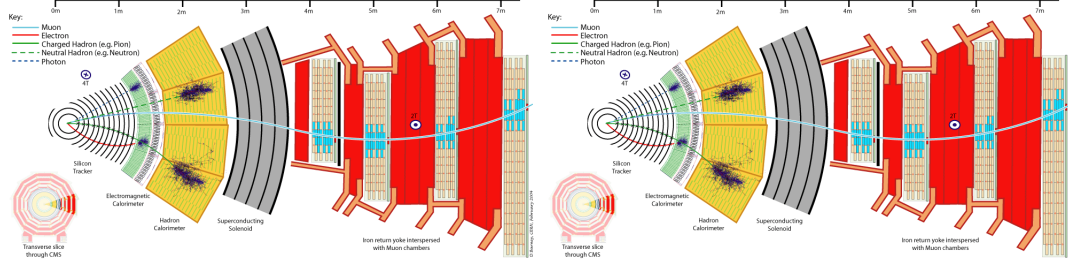The efficiency times acceptance $(\varepsilon \times A)$ combined as one is seen the figure 8.1.

Figure 8.1: Signal efficiency × Acceptance for signal events passing our events selection for the SPS8(left) and GGM(right) models. The acceptance are photons with $t > 3$ ns.

The $\frac{N^{expet}}{\mathscr{L}}$ defines the expected signal cross section which is obtained from a given signal model. In our scenario, our choice of signal model we want to produce exclusion limits on the possible production and decay of a long-lived particle described by this signal model is GMSB. Thus the interpretation of our search analysis is given within the context of any GMSB model with a long-live neutral particle decaying to a photon and gravitino. Such a model is the minimal GMSB or the SPS8 model and the general GMSB model. However, the results provided are based on interpretation within the context of the SPS8 model. In GMSB, the neutralino $\tilde{\chi}_1^0$ is the NLSP and decays to the gravitino $\tilde{G}$ the LSP (as a result of R-parity conservation) in association with a very energetic photon γ. Because of the smallness in mass difference between the $\tilde{\chi}_1^0$ and the $\tilde{G}$ as well as the coupling, the $\tilde{\chi}_1^0$ decay to $\tilde{G}$ is delayed and as a result, the photon emitted can arrive late in the calorimeter crystals. Measuring the arrival time of the photon on ECAL crystals, we can extract important parameters of theory of GMSB.
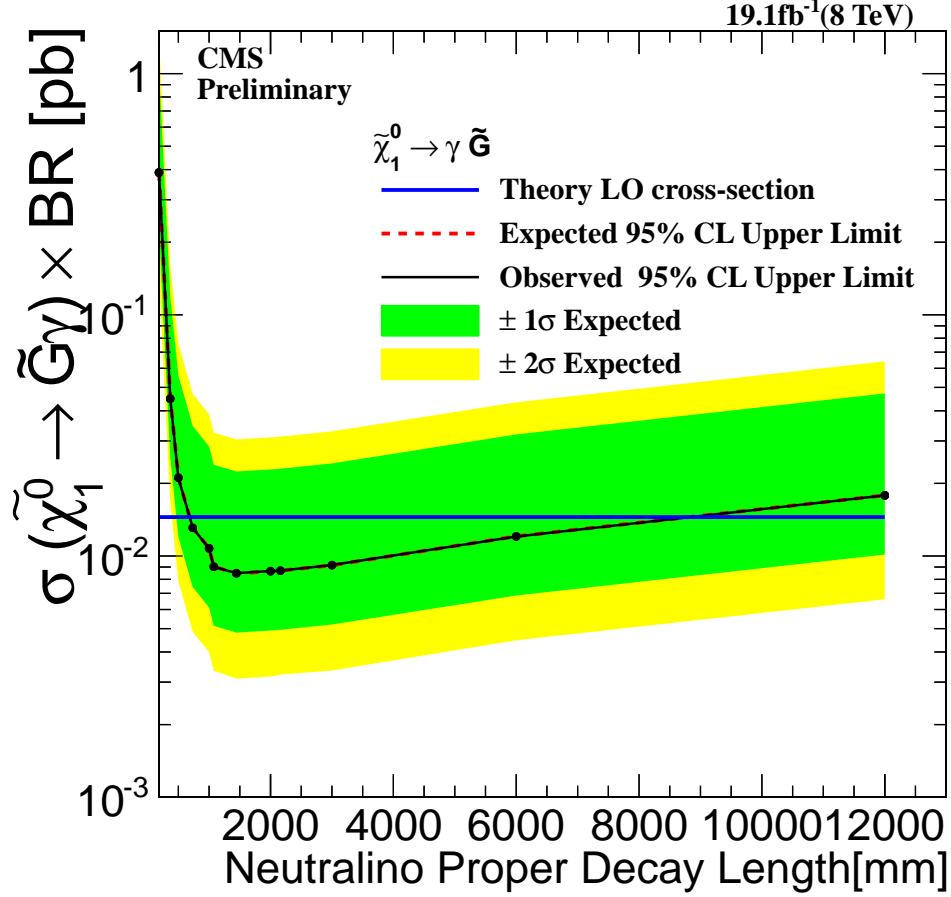
Figure 8.2: Neutralino production cross section against proper delay length upper limit interpretation in SPS8 model.

In the SPS8 model, the parameter space for long-live neutralinos is govern by $\Lambda_m - c\tau$ 2-dimensional parameter space. For each Λ_m point, we have a fixed neutralino mass with different proper lifetimes $c\tau$. We have obtained limits for Λ_m ranging from 100 TeV to 180 TeV corresponding to lightest neutralino mass $m_{\tilde{\chi}_1^0}$ between 90 to 255 GeV/c^2 and proper lifetime $c\tau$ ranging from 250 to 12000 mm corresponding to $\tau_{\tilde{\chi}_1^0}$ from 0.8 ns to 40 ns.

For a given value of $\Lambda_m = 180$ TeV, we have a lightest neutralino production cross section times branching ratio plot shown in figure 8.2, showing that the ECAL detector is sensitive to lightest neutralinos of mass $m_{\tilde{\chi}_1^0} = 255$ GeV/c^2 and life time upto 30 ns

and we are 95% confident that we have not missed any neutralino whose mass is $m_{\tilde{\chi}_1^0} = 255\ GeV/c^2$ and lifetime is $\tau \leq 30$ ns.

For a given lifetime of $\tau = 20$ ns, we can also obtain upper limits on the production cross section times branching ratio when compared against their theoretically expected values for a lightest neutralino with mass ranging from $m_{\tilde{\chi}_1^0} = 90\ GeV/c^2$ to $m_{\tilde{\chi}_1^0} = 255\ GeV/c^2$. The observed upper limit on this cross section is $\sigma_{\tilde{\chi}_1^0}^{UP} \geq XX$ pb with proper lifetime of $\tau = 30$ ns.

Using both the mass and proper lifetime of the lightest neutralino, we present possible 2-dimensional limits simulateneously on $m_{\tilde{\chi}_1^0}$ or Λ_m and $c\tau$ or τ in the SPS8 model, comparing this with the result of previous experiments. This is shown in figure 8.3.
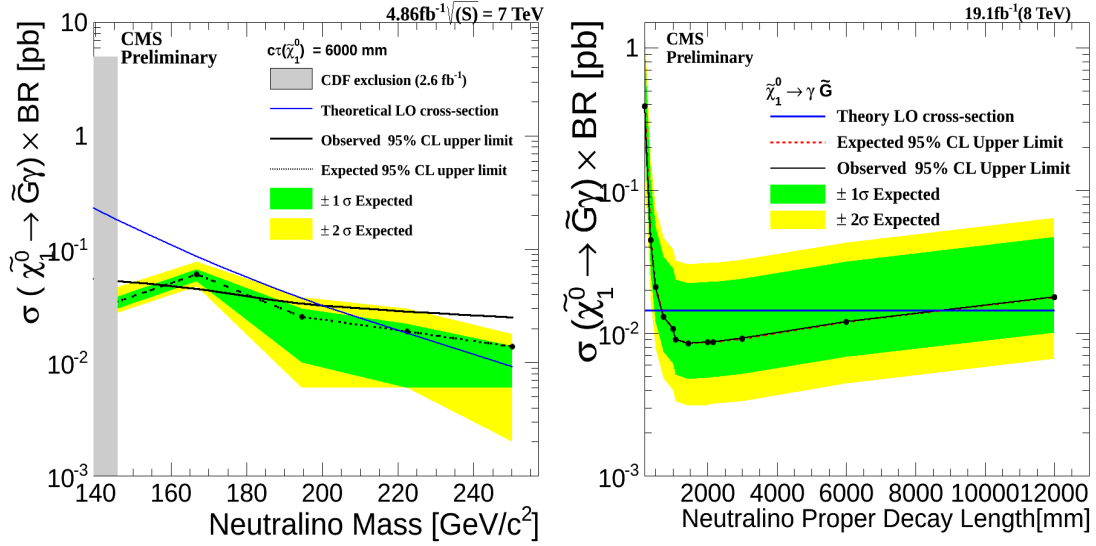
Figure 8.3: Neutralino production cross section against proper delay length upper limit at 95% confidence levels interpretation in SPS8 model.

Figure 8.4: Neutralino two dimensional exclusion limit of neutralino mass (Λ) against proper delay length upper limit interpretation in SPS8 model in the decay $\tilde{\chi}_1^0 \rightarrow \gamma + \tilde{G}$ with limits from previous experiments shown.

8.2   Future Improvements

8.2.1   Beam Halo Monitoring Detector

8.2.2   Back-end Electronics upgrade HCAL

Chapter 9

Conclusion

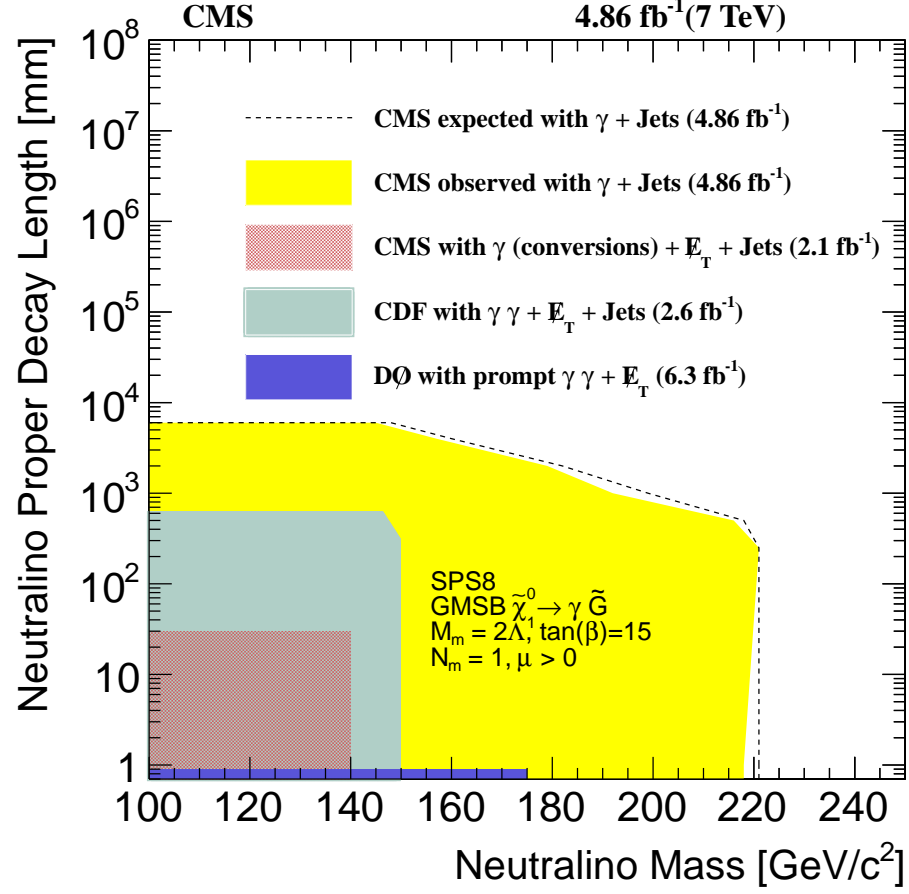We have performed a search analysis for NMLLP decaying to photons using the time of arrival of the photon as measured by the ECAL sub detector of the CMS detector. Haven fail to find any significant signal of delayed photons over the standard model background, we interpreted our results in SUSY models with NMLLP like SPS8 of minimal GBSM or general GMSB models. We showed that, neutralinos whose production and decay mechanism is described in the SPS8 mGMSB model, with $m_{\tilde{\chi}_1^0} \leq XX\ GeV/c^2$ and $\tau_{\tilde{\chi}_1^0} \leq XX$ ns are ruled out of existence at 95% confidence level using the 2012 8 TeV LHC dataset. This corresponds to an upper limit of $\sigma_{\tilde{\chi}_1^0}^{UP} \geq XX$ pb on the production cross section times branching ratio in a hadron collider. In addition, we mention some of the limitations in this particular analysis from a detector point of view and how in future studies can be improved. We hope that in the future, with increase in center of mass energy of the LHC collider as well as luminosity and an improve in timing resolution beyond what is already very reliable, we will surely find a new fundamental particle whose dynamics cannot be described by the already very successful standard model of particle physics.

References

[1] J.Ellis, J.Hagelin, D. Nanopoulos, K.A. Olive and M. Srednicki; *Nucl. Phys.* B238 (1984) 453; H. Goldberg, *Phys. Rev. Lett* 50 (1983) 1419; J. Ellis, T. Falk, G. Ganis, K.A. Olive and M. Srednicki, *Phys. Lett.* B 510 (2001) 236, arXiv: hep-ph/0102098.

[2] H. N. Brown et al., Muon $g_\mu - 2$ Collaboration, *Phys. Rev. Lett* 88 (2002) 2227, hep-ex/0102017; A. Czarnecki and W.J. Marciano, *Phys. Rev.* D 64 (2001) 013014, hep-ph/0102122.

[3] M. Knecht and A. Nyffeler, hep-ph/0111058; I. Blokland, A. Czarnecki and K. Melnikov *Phys.Rev. Lett* 88 (2002) 071803 hep-ph/0112117

[4] CLEO Collaboration, M. S Alan et al., *Phys. Rev. Lett.* 74 (1995) 2885 as updated in S. Amed et al., CLEO CONF 99-10;

[5] BELLE Collaboration hep-ex/0103042

[6] S.Mathin, arXiv:hep-ph/9709356

[7] B.Allanach et al,arXiv:hep-ph/0202233v1

[8] P. Meade, N. Seiberg, and D. Shih, Prog. Theor. Phys. Suppl. 177, 143 (2009), arXiv:0801.3278 [hep-ph]

[9] M. Buican, P. Meade, N. Seiberg, and D. Shih, J. High Energy Phys. 0903, 016 (2009), arXiv:0812.3668 [hep-ph]

[10] M. Dine and A. E. Nelson, Phys. Rev. D 48, 1277 (1993), arXiv:hep-ph/9303230

[11] M. Dine, A. E. Nelson, and Y. Shirman, Phys. Rev. D 51, 1362 (1995), arXiv:hep-ph/9408384

[12] M. Dine, A. E. Nelson, Y. Nir, and Y. Shirman, Phys. Rev. D 53, 2658 (1996), arXiv:hep-ph/9507378

[13] J. T. Ruderman and D. Shih, J. High Energy Phys. 1208, 159 (2012), arXiv:1103.6083 [hep-ph]

[14] G.F. Giudice and R. Rattazzi "Theories with Gauge-Mediated Supersymmetry Breaking" arXiv:hep-ph/9801271v2

[15] J.Dann et al.(LEPSUSY Working Group), Internal note LEPSUSYWG/97-04(1997), P. Janot, talk at the EPS Conference, Jerusalem, 1997.

[16] CDF Collaboration, "Search for Supersymmetry with Gauge-Mediated Breaking in Diphoton Events with Missing Transverse Energy at CDFII ",*Phys. Rev. Lett.*

[17] ATLAS Collaboration "Search for Diphoton Events with Large Missing Transverse Momentum in 1 fb^{-1} of 7TeV Proton-Proton Collision Data with the ATLAS Detector", arXiv:1111.4116v1,17th Nov 2011.

[18] CMS Draft Analysis,"Search for Long-Lived Particles using Displaced Photons in PP Collision at $\sqrt{S} = 7TeV$ ", CMS AN AN-11-081 104(2010)011801,

[19] ATLAS Collaboration, J. High Energy Phys. 1212, 124 (2012), arXiv:1210.4457 [hep-ex]

[20] The LHC Machine, Lyndon Evans and Philip Bryant *Jinst*,

[21] The CERN Brochure 2009-003-Eng

[22] CMS Collaboration, "The CMS experiment at the CERN LHC", JINST 0803:S08004, 2008.

[23] CMS uses a right-handed coordinate system, with the origin at the nominal interaction point, the x-axis pointing to the center of the LHC, the y-axis pointing up (perpendicular to the LHC plane), and the z-axis along the counterclockwise-beam

direction. The polar angle, θ, is measured from the positive z-axis and the azimuthal angle, ϕ, is measured in the x-y plane. $\boldsymbol{\eta = -\ln\tan(\theta/2)}$. The transverse energy and momentum are defined as $\boldsymbol{E_T = E\sin\theta}$ and $\boldsymbol{p_T = p\sin\theta}$ where E is the energy measured in the tracking system. $\boldsymbol{E_T^{\mathrm{miss}} = |-\sum_i E_T^i \vec{n_i}|}$ where $\boldsymbol{\vec{n_i}}$ is a unit vector that points from the interaction vertex to the transverse plane.

[24] "Timing Distribution at the LHC", B.G. Taylor Colmar, 9-13 September 2002

[25] "An FPGA based multiprocessing CPU for Beam Synchronous Timing in CERNs SPS and LHC".*Proceedings of ICALEPCS2003, Gyeongju, Korea ICALEPCS 2003*

[26] "Timing and Synchronization in the LHC Experiments", Varela, J. Krakv, 11-15 September 2000.

[27] http://ttc.web.cern.ch/TTC/intro.html

[28] CMS Collaboration,"CMS Physics: Technical design report, Volume 1" CERN-LHCC-2006-001

[29] "Study of the LHC ghost charge and satellite bunches for luminosity calibration.", CERN-ATS-Note-2012-029 PERF

[30] "LHC bunch current normalisation for the April-May 2010 luminosity calibration measurements.", CERN-ATS-Note-2011-004 PERF

[31] CMS Collaboration, "The CMS ECAL performance With examples", JINST 9 C02008, 2014.

[32] CMS Collaboration,"The electromagnetic calorimeter. Technical design report ",. CERN-LHCC-97-33

[33] CMS Electromagnetic Calorimeter Collaboration, "Energy resolution of the barrel of the CMS Electromagnetic Calorimeter",JINST 2(2007)P04004.

[34] CMS Collaboration, "Time Reconstruction and Performance of the CMS Crystal Electromagnetic Calorimeter",CFT-09-006, 2009.

[35] Bo Lofstedt, "The digital readout system for the CMS electromagnetic Calorimeter",*Nucl. Inst. Methods in Physics Research*,A 453 (2000) 433-439

[36] "Characterization and treatment of anomalous signals in the CMS Electromagnetic Calorimeter " CMS AN AN-10-357

[37] " Mitigation of Anomalous APD signals in the CMS ECAL",*2013, JINST 8 C03020*, W.Bialas and D.A. Petyt

[38] CMS Collaboration, "CMS trigger and data taking in 2010 ",*CMS CR-2011/051*.

[39] CMS Collaboration, "Reconstruction of the signal amplitude of the CMS electromagnetic Calorimeter", Eur.Phys.J. C46S1(2006)23-35.

[40] D.del Re et al "An algorithm for the determination of the flight path of long-lived particles decaying into photons" CMS AN -2010/212.

[41] CMS Collaboration,"Particle-Flow Event Reconstruction in CMS and Performance for Jets, taus and $\not{E}_T$", CMS Physics Analysis Summary CMS-PAS-PFT-09-001(2009).

[42] CMS Collaboration, Missing Transverse Energy Performance in Minimum-Bias and Jet Events from Proton-Proton Collisions at $\sqrt{s} = 7$ TeV , CMS Physics Analysis Summary CMS-PAS-JME-10-004 (2010).

[43] MET JINST (arXiv:1106.5048)

[44] CMS Collaboration, "Missing transverse energy performance of the CMS detector"; arXiv:1106.5048v1

[45] CMS Collaboration,"CMS Physics: Technical design report, Volume 2" CERN-LHCC-2006-001.

[46] CMS Collaboration,"Determination of Jet Energy Scale in CMS with pp collisions at $\sqrt{S} = 8$ TeV",*JME-10-010(2012)*

[47] "https://twiki.cern.ch/twiki/bin/viewauth/CMS/EGamma2012."

[48] "Parton distributions for the LHC" Eur.Phys.J C63(2009) 189-285 or arXiv:0901.0002

[49] CMS Collaboration, "Search for ADD Extra-dimensions with Photon + MET signature", *AN-11-319(2011)*

[50] "Presentation of search results: the CLs technique ",*A L Read 2002 J. Phys. G: Nucl. Part. Phys. 28 2693*

[51] "Computation of confidence levels for search experiments with fractional event counting and the treatment of systematic errors", *Peter Bock JHEP01(2007)080*

[52] https://twiki.cern.ch/twiki/bin/viewauth/CMS/

[53] "Asymptotic formulae for likelihood-based tests of new physics" *G. Cowan et al, arXiv:1007.1727v3*

Appendix A

Glossary and Acronyms

Care has been taken in this thesis to minimize the use of jargon and acronyms, but this cannot always be achieved. This appendix defines jargon terms in a glossary, and contains a table of acronyms and their meaning.

A.1 Glossary

- **Cosmic-Ray Muon (CR μ)** – A muon coming from the abundant energetic particles originating outside of the Earth's atmosphere.

- **SUSY** – A theoretical model based on a fundamental symmetry called supersymmetry in which the fermions and bosons can exchange their spin, extending the standard model to account for the stability in the observed Higgs boson mass and to also predicting the existence of many extra new particles which could be candidates of dark matter.

A.2 Acronyms

Table A.1: Acronyms

NMLLP	Neutral Massive Long-Lived Particles.
DM	Dark Matter.
DE	Dark Energy.
GMSB	Gauge Mediated Supersymmetry Breaking
LHC	Large Hadron Collider
CMS	Compact Muon Solenoid
CRμ	Cosmic-Ray Muon